INTERACTIVE ENVIRONMENT FOR THE CALIBRATION AND VISUALIZATION OF MULTI-SENSOR MOBILE MAPPING SYSTEMS

A Dissertation

Submitted to the Faculty

of

Purdue University

by

Radhika Ravi

In Partial Fulfillment of the

Requirements for the Degree

of

Master of Science in Civil Engineering

August 2019

Purdue University

West Lafayette, Indiana

THE PURDUE UNIVERSITY GRADUATE SCHOOL
STATEMENT OF DISSERTATION APPROVAL

Dr. Ayman Habib, Chair

Lyles School of Civil Engineering, Purdue University

Dr. Melba Crawford

Lyles School of Civil Engineering, Purdue University

Dr. Wolfgang Förstner

Institute of Geodesy and Geoinformation, University of Bonn

Approved by:

Dr. Dulcy Abraham

Head of the School Graduate Program

To my family, who always believed in me.

To the memory of my boyfriend, Vishesh.

ACKNOWLEDGMENTS

First and foremost, I would like to express my sincere gratitude towards my advisor, Dr. Ayman Habib, for his constant guidance and encouragement during my entire duration of graduation study and research. He has taught me the most vital qualities for being a successful researcher – curiosity and passion. With these learnings, I will strive to become a better independent researcher. Besides my advisor, I would like to thank my thesis committee members – Dr. Melba Crawford and Dr. Wolfgang Förstner – for taking their precious time to serve on my advisory committee and providing me their valuable advice.

A special thanks to my parents and my little brother for their love and for being a support system throughout my graduate study. Without their support and encouragement, it would not be possible to finish my research. Also, I would like to thank Vishesh Panjabi, who, although no longer with us, first introduced me to the world of research, provided me immense love and support, always believed in my abilities, and still continues to motivate me to keep moving forward.

I would also like to thank the wonderful members of Digital Photogrammetry Research Group, especially Yun-Jou Lin, Magdy Elbahnasawy, Tamer Shamseldin, Ronald Benziger, Fangning He, Tian Zhou, Seyyed Meghdad Hasheminasab, and Evan Flatt for their invaluable support and contribution towards my research. My special thanks to all my friends who made my stay here in the United States enjoyable.

I would like to acknowledge Joint Transportation Research Program (JTRP) and Advanced Research Projects Agency-Energy (ARPA-E). This work was supported in part by JTRP (administered by the Indiana Department of Transportation and Purdue University) and ARPA-E, U.S. Department of Energy. The views and opinions of authors expressed herein do not necessarily state or reflect those of the sponsoring organizations.

TABLE OF CONTENTS

Page

Page

LIST OF TABLES

LIST OF FIGURES

Figure Page

ABBREVIATIONS

2D	Two-dimensional
3D	Three-dimensional
GNSS	Global Navigation Satellite System
GPS	Global Positioning System
I-LIVE	Image-LiDAR Interactive Visualization Environment
IMU	Inertial Measurement Unit
INS	Inertial Navigation System
IOP	Interior Orientation Parameters
LiDAR	Light Detection And Ranging
LSA	Least Squares Adjustment
MMS	Mobile Mapping System
PPS	Pulse Per Second
RMSE	Root Mean Square Error
SPAN	Synchronized Position Attitude Navigation
UAV	Unmanned Aerial Vehicle

ABSTRACT

Ravi, Radhika M.S.C.E., Purdue University, August 2019. Interactive Environment For The Calibration And Visualization Of Multi-sensor Mobile Mapping Systems. Major Professor: Ayman Habib.

LiDAR units onboard airborne and terrestrial platforms have been established as a proven technology for the acquisition of dense point clouds for a wide range of applications, such as digital building model generation, transportation corridor monitoring, precision agriculture, and infrastructure monitoring. Furthermore, integrating such systems with one or more cameras would allow forward and backward projection between imagery and LiDAR data, thus facilitating several high-level data processing activities such as reliable feature extraction and colorization of point clouds. However, the attainment of the full 3D point positioning potential of such systems is contingent on an accurate calibration of the mobile mapping unit as a whole.

This research aims at proposing a calibration procedure for terrestrial multi-unit LiDAR systems to directly estimate the mounting parameters relating several spinning multi-beam laser scanners to the onboard GNSS/INS unit in order to derive point clouds with high positional accuracy. To ensure the accuracy of the estimated mounting parameters, an optimal configuration of target primitives and drive-runs is determined by analyzing the potential impact of bias in mounting parameters of a LiDAR unit on the resultant point cloud for different orientations of target primitives and different drive-run scenarios. This impact is also verified experimentally by simulating a bias in each mounting parameter separately. Next, the optimal configuration is used within an experimental setup to evaluate the performance of the proposed calibration procedure. Then, this proposed multi-unit LiDAR system calibration strategy is extended for multi-LiDAR multi-camera systems in order to allow a simultaneous

estimation of the mounting parameters relating the different laser scanners as well as cameras to the onboard GNSS/INS unit. Such a calibration improves the registration accuracy of point clouds derived from LiDAR data and imagery, along with their accuracy with respect to the ground truth. Finally, in order to qualitatively evaluate the calibration results for a generic mobile mapping system and allow the visualization of point clouds, imagery data, and their registration quality, an interface denoted as Image-LiDAR Interactive Visualization Environment (I-LIVE) is developed. Apart from its visualization functions (such as 3D point cloud manipulation and image display/navigation), I-LIVE mainly serves as a tool for the quality control of GNSS/INS-derived trajectory and LiDAR-camera system calibration.

The proposed multi-sensor system calibration procedures are experimentally evaluated by calibrating several mobile mapping platforms with varying number of LiDAR units and cameras. For all cases, the system calibration is seen to attain accuracies better than the ones expected based on the specifications of the involved hardware components, i.e., the LiDAR units, cameras, and GNSS/INS units.

1. INTRODUCTION

1.1 Problem Statement

Light Detection and Ranging (LiDAR) units use laser beams to measure ranges and generate precise 3D information about the scanned area. Such units onboard airborne platforms (UAVs) and terrestrial platforms (cars or trucks) have been established as a proven technology for the acquisition of dense point clouds with high positional accuracy. The main factors behind the widespread use of LiDAR systems include the ever-continuous improvement in GNSS/INS direct georeferencing technology as well as enhanced performance and reduced size and cost of laser scanning units. Currently, there are commercially available LiDAR units that are capable of emitting more than a quarter million pulses per second at a cost of less than U.S. $10k. Such availability, together with the ever-increasing range of applications – such as digital building model generation, transportation corridor monitoring, telecommunications, precision agriculture, infrastructure monitoring, seamless outdoor-indoor mapping, and power line clearance evaluation [23, 28, 36, 38] – have led to the development of multi-unit mobile LiDAR systems onboard airborne and terrestrial platforms that are either manned or unmanned. Furthermore, integrating such systems with one or more cameras would allow forward and backward projection between imagery and LiDAR data, thus facilitating several high-level data processing activities, such as reliable feature extraction and colorization of point clouds. However, the attainment of the full 3D point positioning potential of such systems is contingent on an accurate calibration of the mobile mapping unit as a whole.

This research aims at proposing a multi-sensor system calibration procedure to directly estimate the mounting parameters relating several spinning multi-beam laser scanners and cameras to the GNSS/INS unit onboard a mobile terrestrial platform

in order to derive point clouds with high positional accuracy. The proposed multi-sensor system calibration strategy allows a simultaneous estimation of the mounting parameters relating the different laser scanners as well as cameras to the onboard GNSS/INS unit. Such a simultaneous calibration technique improves the registration accuracy of point clouds derived from LiDAR data and imagery, along with their accuracy with respect to the ground truth. In order to ensure a sufficiently high accuracy of estimated mounting parameters using the proposed strategy, an optimal configuration of target primitives and drive-runs needs to be determined by analyzing the potential impact of bias in mounting parameters of a LiDAR unit on the resultant point cloud for different orientations of target primitives and different drive-run scenarios. Finally, an interactive interface is developed in this research so as to provide end-users the possibility to conduct a qualitative evaluation. The interface allows the visualization of point clouds, imagery data, and their registration quality, thus facilitating the evaluation of calibration results for a generic mobile mapping system. The primary purpose of the interface is to serve as a tool for qualitative quality control of GNSS/INS-derived trajectory and LiDAR-camera system calibration.

1.2 Thesis Organization

Chapter 1 describes the motivation of the thesis and the problem statement addressed in this research.

Chapter 2 reviews the literature of past and ongoing research related to calibration of mapping systems that utilize LiDAR units and cameras. Furthermore, it focuses on highlighting the contributions of the current research work while comparing the proposed approach to prior strategies adopted for calibration. Finally, this chapter also introduces the basic mathematical equations involved in 3D point positioning for points captured using generic mobile mapping systems consisting of LiDAR units and cameras.

Chapter 3 focuses on conducting a bias impact analysis for LiDAR-based mapping systems. In this chapter, we derive a mathematical formulation that shows the deformations/shifts of points due to the presence of a bias in system mounting parameters for different target and drive-run configurations. This analysis leads to the development of an optimal configuration of drive-runs and target primitives for conducting an accurate calibration of wheel-based mobile mapping systems. Further, the theoretical analysis is validated experimentally by simulating a bias in each mounting parameter separately.

Chapter 4 aims at developing a calibration strategy - based on the use of conjugate points and linear/planar features - to directly estimate the mounting parameters for multiple sensors (LiDAR units and cameras) onboard a mobile platform. This chapter further analyzes the experimental results from real datasets collected using different mobile mapping systems. An in-depth qualitative as well as quantitative evaluation indicates the efficiency of the proposed calibration strategy.

Chapter 5 discusses the development and functionalities of the Image-LiDAR Interactive Visualization Environment (I-LIVE) with regard to serving as a user-friendly tool for the visualization of acquired 3D point clouds and images as well as the quality control of GNSS/INS-derived trajectory and multi-sensor system calibration.

Chapter 6 summarizes the key contributions of this research and provides recommendations for future work related to this field.

Parts of this work have been recreated from:
Ravi et al. [30] and Ravi et al. [31]

2. LITERATURE REVIEW

This chapter discusses the evolution of mobile mapping systems over the past few years and their applications. The review of existing literature is conducted in three parts – first, focusing on the literature related to the calibration of mapping systems using laser scanners, second related to various approaches used for the calibration of camera-based mapping systems, and the last targeted at the past research conducted for the calibration of systems integrating LiDAR units as well as cameras.

2.1 LiDAR System Calibration

Over the past few years, extensive research has been conducted for the calibration of mobile mapping systems utilizing laser scanners. The cost-effective Velodyne laser scanner can rapidly capture a high volume of data and has been used in many mobile mapping systems and robotics applications [5, 33, 34]. A great deal of research has been devoted to modeling the inherent systematic errors in Velodyne laser scanners as well as the calibration of LiDAR systems [1, 12]. Muhammad and Lacroix [25] performed calibration of a spinning multi-beam LiDAR with the objective to align the scan data as close as possible to a ground truth environment. He et al. [20] used pairwise multi-type 3D geometric features (i.e., points, lines, and planes) to derive the extrinsic parameters between a 2D LiDAR and an integrated global positioning system (GPS)/inertial measurement unit (IMU). First, the points are segmented into different features (such as points, lines, and planes) and their quality is evaluated to compute weights to be used in the minimization of normal distance between conjugate features. However, when the initial parameters are highly inaccurate, the segments and derived weights may not be reliable. Chan et al. [4] introduced an intrinsic parameters calibration using vertical cylindrical features for Velodyne HDL32E based

on static stations and also analyzed the temporal stability of range measurements, thus indicating an approximate warm-up time of 2000 s for most laser beams. Glennie et al. [13] performed a geometric calibration using planar features scanned by stationary VLP16 to marginally improve the accuracy of the point clouds by approximately 20%. Moreover, the range accuracy of VLP16 was also investigated, which was quoted to have a root mean square error (RMSE) value between 22 to 27 mm in the factory supplied calibration certificate. It was observed that some of the laser beams have worse range accuracy than the others. Habib et al. [19] studied the impact of airborne LiDAR system calibration on the relative and absolute accuracy of the derived point clouds, both qualitatively and quantitatively. The relative accuracy was evaluated by quantifying the degree of coalignment of overlapping strips before and after calibration, whereas the absolute accuracy was evaluated by quantifying the degree of compatibility between LiDAR and control surfaces before and after calibration.

2.2 Camera System Calibration

Over the years, several techniques have been developed to accurately calibrate different types of cameras in order to obtain accurate estimates of their intrinsic and extrinsic parameters. Duane [8] suggested the widely-used mathematical model for removing radial lens distortion for close-range photogrammetry. Conrady [6] proposed a generic model for eliminating decentering distortion. Weng et al. [37] proposed a two-step stereo camera calibration procedure to obtain the intrinsic parameters and the exterior orientation parameters of the involved cameras. The first step aimed to obtain the exterior orientation parameters using a closed-form solution by assuming a distortion-free camera model. Then, the parameters obtained in the first step were improved iteratively through a nonlinear optimization, taking into account camera distortions. Zhang [41] proposed a technique for camera calibration using a planar pattern captured by a camera from different orientations. This approach used a closed-form solution, followed by a nonlinear refinement based on the maximum

likelihood criterion. The models proposed by [6, 8] for radial and decentering lens distortion are used for intrinsic calibration of the cameras in this research.

2.3 LiDAR-Camera System Calibration

Although many procedures have been developed for LiDAR system calibration and camera system calibration separately, the simultaneous calibration of a mapping system consisting of both LiDAR units and cameras is an area of research that is still under exploration. Delara et al. [7], Furukawa and Ponce [10] suggested the incorporation of LiDAR data as control points within the bundle adjustment for camera calibration. Zhang and Pless [40] performed an extrinsic calibration of a camera and a 2D laser range finder by observing a planar checkerboard pattern and solving for constraints between the views from both of these devices. This was done by first determining the pose of the camera with respect to the calibration plane, which was further used to estimate the normal direction for the planar pattern in the camera coordinate system. Then, the extrinsic parameters, i.e., the rigid transformation from the camera coordinate system to the laser coordinate system, were obtained by constraining the points (belonging to the planar pattern) captured by the laser scanner to lie on the planar pattern estimated from the camera image. Habib et al. [16] suggested alternative approaches for the registration of data captured by LiDAR and photogrammetric systems using a set of linear features by applying a bundle adjustment followed by a similarity transformation. Fremont et al. [9] proposed an approach for extrinsic calibration of a camera and a 3D laser range finder using a circle-based calibration object. First, an initial estimate of the rigid transformation between the camera and laser unit coordinate systems was obtained through parametrizing the calibration target by the 3D coordinates of the circle center and the normal vector of its plane. Then, a nonlinear 3D minimization was carried out in order to refine the estimated extrinsic parameters. Castorena et al. [3] devised a method for automatic extrinsic calibration and sensor fusion for a system comprised of a LiDAR and an

optical camera by exploiting the natural alignment of depth map and intensity edges. However, this approach demands the availability of depth maps and intensity images for accurate calibration and cannot be applied in case of an unavailability of either of the information. Le and Ng [21] proposed an approach for calibrating multiple sensors (cameras, laser unit, and robot arm) by grouping them such that each group outputs 3D data. Their approach uses geometric constraints (distance preservation, collinearity, and coplanarity constraints) applied to 3D data in order to estimate the extrinsic parameters relating the different sensors of a robotic system. However, their calibration approach was designed for stationary systems, and moreover, their framework was built upon 3D systems, i.e., the 3D data output from a combination of sensors was used for their framework. For instance, two cameras onboard a system were grouped to form a stereo vision system that outputs 3D data. On the other hand, the calibration approach proposed in this thesis deals with directly georeferenced mobile systems and it can estimate the extrinsic parameters for single or multiple cameras without having a need to group them to create 3D systems. Levinson and Thrun [22] devised an approach for real-time miscalibration detection and correction of sensor mounting parameters. Any sudden miscalibration was detected using a probabilistic background monitoring algorithm and any gradual drift in sensor parameters was tracked and adjusted by observing the change in the objective function over past few frames of data capture. Although their approach can accurately detect small incremental values to attain accurate calibration, they have not addressed the issue of accurate calibration starting with highly inaccurate initial estimates for the parameters. However, this problem is mitigated by the calibration approach proposed in this thesis where we demonstrate that it can attain accurate calibration results even on starting with inaccurate estimates. Mirzaei et al. [24] proposed an approach to jointly estimate the intrinsic parameters of a 3D LiDAR along with the LiDAR-camera transformation parameters. Their approach used planar calibration boards with fiducial markers to establish geometric constraints between the measurements from LiDAR (3D) and camera (2D), their extrinsic parameters, and the LiDARs intrinsic param-

eters. They used 2D-3D exact point-to-point correspondences for calibration. They used a two-step approach where they first obtained precise initial estimates for the unknown parameters by dividing the problem into two least-squares sub-problems and solving each of them analytically. Then, the accuracy of these parameters was increased by iteratively minimizing a batch non-linear least-squares cost function. García-Moreno et al. [11] proposed an extrinsic calibration technique using a planar target for a mobile mapping system consisting of a LiDAR sensor, video camera, GPS, and Inertial Measurement Unit (IMU). This approach used a pattern which facilitates the extraction of the same point in camera and LiDAR data. This pattern was composed of white rhombus and rhombus holes for which image points can be easily measured and this pattern can be extracted using RANSAC to determine planar surface in a LiDAR point cloud. Pandey et al. [26] proposed an automatic targetless extrinsic calibration strategy of a 3D laser scanner and camera system. They used a mutual information (MI) framework based on the registration of the laser reflectivity of a 3D LiDAR point and the corresponding grayscale value of the image pixel to which this 3D point is projected. This approach does not rely on any calibration target and thus, it is capable of in-situ calibration. Since their method relies on intensity and reflectivity information, it works under several assumptions. One of the assumptions is that the 3D LiDAR unit that is used provides meaningful surface reflectivity values, which is not always the case and hence, in order to use this approach, the LiDAR unit needs to be first calibrated for its reflectivity values. Also, their work assumes a high correlation for the reflectivity and intensity values obtained from the images and LiDAR scans. However, this might not always be true since in case of images, the ambient light plays a critical role in determining the intensity levels of the image pixels and hence, there can be a presence of shadows. But, the corresponding reflectivity values in the laser scans are not affected because it uses an active lighting principle. Thus, in such scenarios, the data between the two sensors might not show a strong correlation and hence, will produce a weak input for their proposed calibration algorithm. Also, their approach assumes the availability

of high quality approximate estimates of the calibration parameters and only focuses on their refinement. Guo and Roumeliotis [15] proposed a calibration technique to estimate the extrinsic parameters between a 2D LiDAR and a camera using a white rectangular calibration board with a black line in the middle as a calibration target. The straight line was detected in the camera image using edge detection followed by a line fitting algorithm. On the other hand, the line scan LiDAR can detect the edge ending points of the calibration board based on depth discontinuity, which were then averaged to find the point on the middle line. They formulated the problem as a nonlinear least squares minimization and solved the problem analytically to find the global minimum. However, they assume that the calibration board would be oriented with respect to the LiDAR such that a scenario where all the LiDAR measurements over the scanned board are parallel to the black line would not occur. Vel'as et al. [35] dealt with an automatic calibration to estimate the extrinsic parameters relating an RGB camera to a Velodyne LiDAR. They used special 3D markers for calibration, which were planar markers with circular holes. An edge detection algorithm based on depth discontinuities was used for detecting the circular edge from 3D LiDAR. For the camera images, the circle edges were detected by an edge detection using Sobel operator followed by a Hough transform. They proposed a two-step approach: first, they performed an approximate coarse calibration where they assumed that the translation between the laser scanner and the camera is much more significant than the rotation. Then, a fine calibration was done to estimate the translation as well as rotation using edges detected in laser scans and images. Pusztai and Hajder [29] utilized cardboard box of known dimensions as a target to calibrate the extrinsic parameters of LiDAR-camera system. First, the planes of the box were identified in the LiDAR point cloud and the corners of the box were derived according to the intersection of the plane. Then, the corresponding corners in the images were selected. The problem to find the extrinsic parameters was then equal to a PnP problem as 2D-3D point-to-point correspondences were known. With this method, the extrinsic parameters of arbitrary number of cameras and LiDAR sensors can be calibrated. [2]

introduced a fully automatic technique to calibrate a geometric mapping between LiDAR and video feeds on a mobile ground-based platform without user intervention or calibration targets. The technique estimated the intrinsic camera parameters and the extrinsic parameters relating the LiDAR and video camera. The author proposed a three-step approach wherein first, the radial distortion parameters were estimated by extracting image contours that correspond to straight real-world objects. Then, the focal length and the rotation relating the LiDAR and camera were derived by using a technique similar to bundle adjustment by either minimizing the reprojection error of identified points on the images or by minimizing the error in the reconstruction in the LiDAR. In this step, it was assumed that the camera and LiDAR are co-located, i.e., there was no significant translation between them. Finally, the previously estimated parameters were refined and the translation between the LiDAR and camera was estimated. This was achieved by extracting 2D contours from images and 3D contours from LiDAR followed by an association between the projected LiDAR contour point and the nearest image contour point. [14] proposed a technique for LiDAR/camera extrinsic calibration for both indoor and outdoor mobile mapping platforms using arbitrary trihedral objects consisting of two adjacent walls of a building together with the ground plane. It is a three-step calibration procedure. First, the LiDAR was calibrated by applying the geometric constraints associated with a trihedral object. Then, a camera calibration was done using SIFT matching between different captured images that have common trihedral planes observed in both LiDAR point cloud and camera images. Finally, a LiDAR-camera extrinsic calibration task was formulated as a non-linear least squares problem using parameters derived in the individual camera and LiDAR calibration steps. [27] improved the calibration accuracy between a camera and a 3D LiDAR. The LiDAR-camera calibration depended on using polygonal boards with known dimensions. By estimating the 3D locations of board vertices from the scanned laser data and their corresponding corners in the 2D image, the calibration approach worked to find point-to-point correspondences between the 2D image and the 3D point clouds. Since this approach was based on 2D-3D exact point-

to-point correspondences, the projection matrix was estimated without separating the intrinsic and extrinsic parameters. [39] performed a LiDAR-camera calibration using specially designed boxes with known dimensions as calibration targets to exploit 2D-2D correspondences. These calibration targets were oriented on a surface parallel to the measurement plane of the LiDAR scanner and camera such that the vertical box-edges appeared as vertical lines in the recorded camera images. [42] proposed an extrinsic calibration algorithm using planar checkerboard of known dimensions to obtain the relative orientation and translation between a camera and a LiDAR. They proposed a two-step approach where they first estimated the rotation by assigning a weight to each pose of the checkerboard based on the corresponding uncertainty of plane normal and minimizing the difference between the normal vectors derived from the LiDAR and camera modalities. Then, the translation was estimated using a closed-form solution.

The characteristics and limitations of the papers discussed above are summarized as follows:

1. The calibration approaches suggested in [9, 11, 15, 24, 27, 29, 35, 39, 40, 42] rely on the usage of specifically designed targets of known dimensions in order to attain accurate results. However, [2, 14, 26] propose a targetless calibration strategy exploiting the features available in the surrounding environment.

2. Most of the proposed calibration techniques use exact point-to-point correspondences. For instance, in [9], 3D-3D point correspondences are used; in [2, 11, 24, 26, 27, 29, 42], 2D-3D point correspondences are used, and in [15, 39, 40], 2D-2D point correspondences are used. However, [14] do not rely on exact point-to-point correspondences for calibration.

3. The LiDAR-camera calibration techniques in [9, 11, 15, 24, 26, 27, 35, 39, 40] are developed only for systems consisting of a single LiDAR and a single camera. But, the techniques of [2, 42] are applicable for systems with a single LiDAR and

multiple cameras. The approaches proposed in [14, 29] are capable of calibrating systems with multiple LiDAR units and multiple cameras.

4. Several calibration approaches, such as the ones proposed in [15, 27, 40] only target the calibration of systems with 2D LiDAR units, whereas other approaches [2, 9, 11, 14, 24, 26, 27, 28, 35, 42] are developed for 3D LiDAR units.

5. The approaches in [9, 15, 24, 27, 29, 35, 39, 40, 42] are indoor calibration approaches, whereas in [2, 11, 26] are outdoor calibration approaches. However, [14] present an approach that can be used for indoor as well as outdoor calibration.

6. Most of the papers [9, 14, 15, 24, 27, 29, 35, 39, 40, 42] propose calibration techniques for stationary systems, which do not have a GNSS/INS unit onboard. On the other hand, [2, 11, 26] use mobile mapping systems with an onboard GNSS/INS unit but they do not address the calibration of the sensors to estimate their mounting parameters with respect to the GNSS/INS unit, thus resulting in a partial calibration of the system.

7. In [11, 15, 26, 27, 39, 40], single-step calibration techniques are proposed, whereas in [2, 9, 14, 24, 29, 35, 42], multi-step calibration approaches are proposed.

8. The approaches proposed in [9, 11, 14, 15, 26, 29, 35, 40] deal with the estimation of only the mounting parameters relating the LiDAR units and cameras to the onboard GNSS/INS unit. Only [24] accounts for intrinsic LiDAR parameters along with the LiDAR and camera mounting parameters calibration. In [2, 27, 39, 42], the intrinsic camera parameters as well as the extrinsic LiDAR-camera parameters are estimated.

9. The research in [2, 9, 14, 15, 24, 26, 27, 29, 35, 39, 40, 42] include a built-in quality control strategy to estimate the accuracy of the proposed calibration

approaches, whereas [11] lacks any information about the quality of the obtained calibration results.

2.4 Comparison of Current Research with Prior Work

The previous discussion indicates that although many LiDAR system calibration procedures have been developed in the past, outdoor calibration of integrated GNSS/INS and multi-unit 3D laser scanners and cameras is still an active area of research. One of the objectives of this thesis is to develop a calibration technique for mapping systems with several spinning multi-beam laser scanners and cameras onboard terrestrial mobile mapping vehicles. The system calibration is realized by simultaneously estimating the statistically optimal solution to the mounting parameters relating the different system components. The estimation minimizes the discrepancy (in a weighted least squares sense) between conjugate points and linear and/or planar features in overlapping point clouds derived from different drive runs. More specifically, the lever arm and boresight angles relating the individual laser scanners and the onboard GNSS/INS unit are derived using an iterative modified weight matrix-based calibration procedure. The proposed approach helps in overcoming several limitations of previously developed LiDAR system calibration procedures. First, the calibration procedures suggested by Chan et al. [4] and Glennie et al. [13] only estimate the intrinsic parameters of a single laser scanner and deal with point clouds captured from stationary scanners. On the contrary, the calibration approach proposed in this thesis deals with mobile mapping systems and is capable of estimating the mounting parameters of multiple laser scanners simultaneously, thus facilitating an accurate alignment between point clouds captured by different sensors. Moreover, this research deals with directly georeferenced point clouds, which would also ensure the alignment between point clouds captured from different survey missions. While Chan et al. [4] use only vertical cylindrical features and Glennie et al. [13] use only planar features for calibration, the approach proposed in this thesis incorporates both linear and

planar features found in outdoor environments to generate more accurate calibration results. Furthermore, unlike the calibration strategy proposed by Muhammad and Lacroix [25], the research conducted in this thesis eliminates the need for ground truth by proposing a calibration approach that aims at minimizing the discrepancy between geometric tie features (lines and planes) scanned in different drive-runs. Another point of emphasis is that the proposed approach deals with a model considering a reference sensor and slave sensors, which provides the flexibility to conduct an indoor calibration of the mobile mapping system to derive the mounting parameters relating the slave sensors to the reference sensor, followed by an outdoor calibration to estimate the mounting parameters relating the reference scanner to the onboard GNSS/INS unit, which in turn, would relate all the laser scanners to the GNSS/INS unit.

Before proceeding with the calibration strategy, an optimal configuration of target primitives setup and drive-runs needs to be determined to maximize the impact of the systematic errors in question which would lead to a more accurate calibration. So, a pre-analysis needs to be conducted to deduce the impact of bias in each of the mounting parameters of a LiDAR unit on the resultant point cloud. Here, the term "bias" is used to denote the deterministic deviation of the mounting parameters from their true values. Habib et al. [17] discussed the bias impact analysis in detail for airborne linear scanners while describing the simplified and quasi-rigorous calibration strategies, whereas in this thesis, the bias impact analysis is conducted for a spinning multi-beam laser scanner starting from the 3D point positioning equation. The optimal configuration of target primitives for calibration is then established by studying the impact of biases on planes oriented in different directions. Similarly, the optimal drive-run configuration is determined according to the effect of biases on the derived planes from drive-runs in different directions and with varying separation. The conclusions drawn based on the results are then validated by simulating a bias in each of the mounting parameters one by one and studying the difference between the resultant and original point clouds. These results are quantified in terms of the RMSE of

normal distances between the derived point clouds and best-fitting plane for various planar features oriented in different directions for different drive-run configurations. Although RMSE does not account for the sign of the effect of a bias, it is still used as a measure to describe the bias impact since the only point of interest is whether a bias introduces a significant discrepancy, irrespective of the signs, in order to be able to accurately estimate the bias by exploiting the nature of its impact.

2.5 Introduction to 3D Point Positioning for a Multi-LiDAR Multi-Camera Mobile Mapping Platform

This section introduces the basic mathematical equations involved in 3D point positioning for points captured using generic mobile mapping systems consisting of LiDAR units and cameras. These point positioning equations form the bases of the research conducted in this thesis. The vector and matrix notations used in this thesis are as follows:

1. r_a^b denotes the coordinates of point "a" relative to point "b" in the coordinate system associated with point "b", as shown in Figure 2.1(a).

2. r_{ab}^c denotes the vector "ab" in the coordinate system "c", as shown in Figure 2.1(b).

3. R_a^b denotes the rotation matrix that transforms a vector defined relative to the coordinate system "a" into a vector defined relative to the coordinate system "b", as shown in Figure 2.1(c).

For instance, using the above notations, any point, A, can be transformed from coordinate system "a" to "b" as: $r_A^b = r_{ab}^b + R_a^b \, r_A^a$.

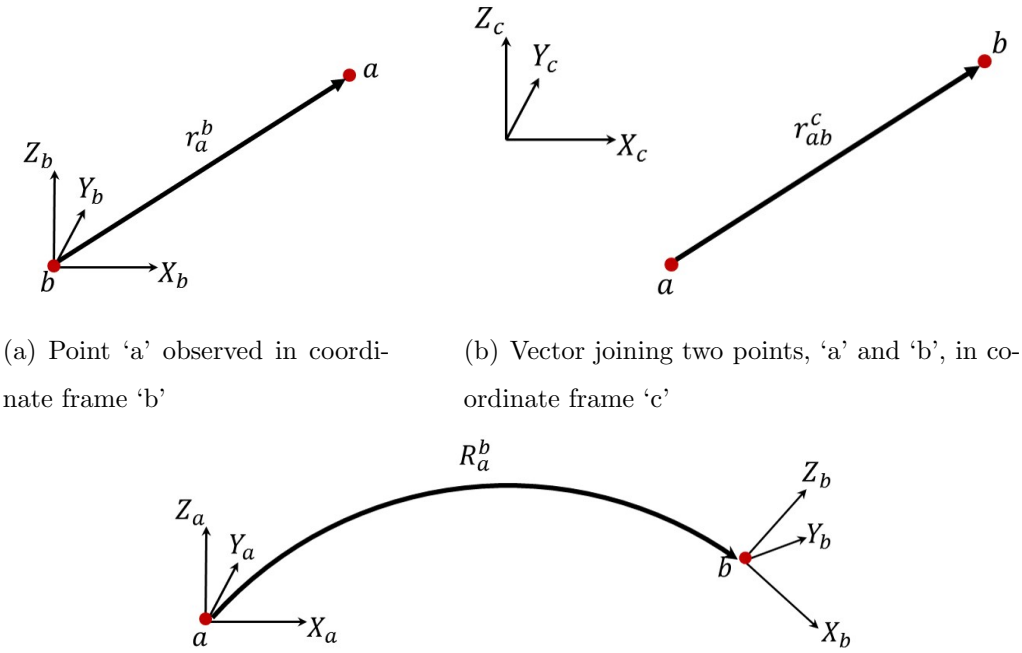

(a) Point 'a' observed in coordinate frame 'b'

(b) Vector joining two points, 'a' and 'b', in coordinate frame 'c'

(c) Rotation from coordinate system 'a' to coordinate system 'b'

Fig. 2.1.: Notations for translation and rotation used in this research

2.5.1 Point Positioning for a GNSS/INS-assisted Multi-unit LiDAR System

A typical LiDAR system consisting of spinning multi-beam laser scanners could involve three coordinate systems, i.e., the mapping frame, the IMU body frame, and the laser unit frame. In case of a mobile mapping system with a single LiDAR unit, a given object point, named I, acquired from the onboard laser scanner can be reconstructed in the mapping coordinate system using (2.1), which is graphically illustrated in Figure 2.2. For the laser unit frame, the origin is defined at the laser beams firing point and the Z-axis is along the axis of rotation of the laser unit. For a spinning multi-beam laser unit, each laser beam is fired at a fixed vertical angle, β, denoting the angle between the laser beam and the XY-plane of the laser unit; the horizontal angle (or, the angle between the projection of the laser beam onto the

XY-plane and the X-axis), α, is determined based on the rotation of the unit; and the range, ρ, is defined by the distance between firing point and its footprint (or, the scanned object point), as shown in Figure 2.3 for Velodyne VLP16 and HDL32E units. So, the coordinates of a 3D point, I, relative to the laser unit coordinate system (Lu), $r_I^{\text{Lu}}(t)$, are defined by (2.2). The laser unit frame (Lu) is related to the IMU body frame (b) by a rigidly defined lever-arm, r_{Lu}^b, and boresight matrix, R_{Lu}^b. The GNSS/INS integration provides the time-dependent position, $r_b^m(t)$, and rotation, $R_b^m(t)$, relating the mapping frame (m) and IMU body frame (b) coordinate systems, according to the optimized solution from the available GNSS and inertial measurements.

$$\begin{aligned} r_I^m &= r_b^m(t) + r_{b\text{-Lu}}^m(t) + r_{\text{Lu-}I}^m(t) \\ &= r_b^m(t) + R_b^m(t)\ r_{\text{Lu}}^b + R_b^m(t)\ R_{\text{Lu}}^b\ r_I^{\text{Lu}}(t) \end{aligned} \tag{2.1}$$

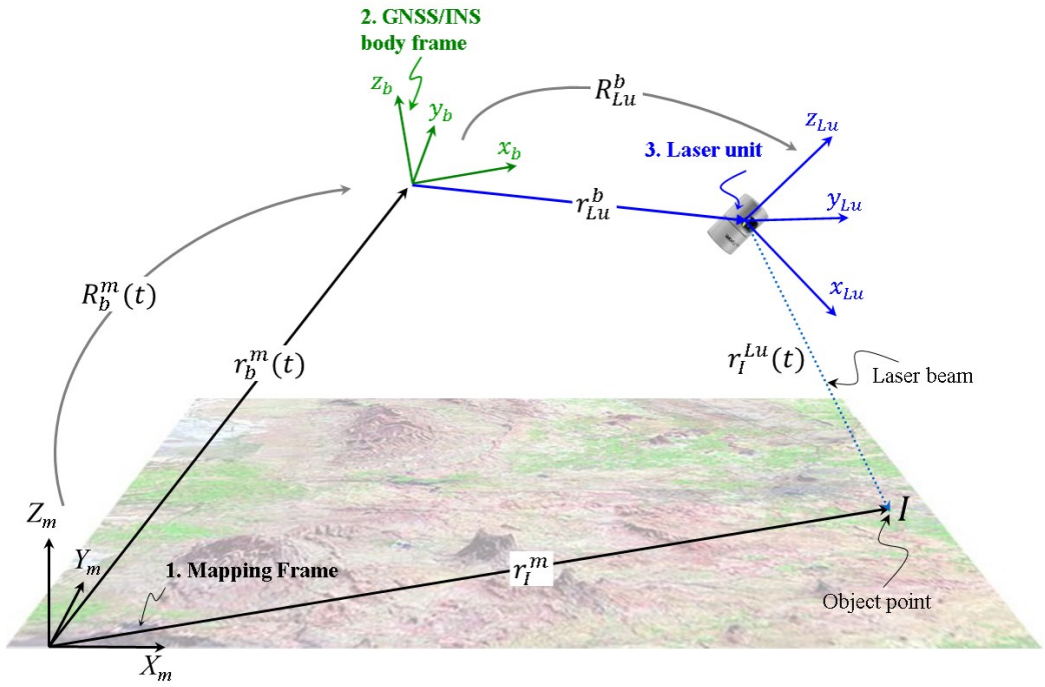

Fig. 2.2.: Illustration of point positioning for a single-unit LiDAR system

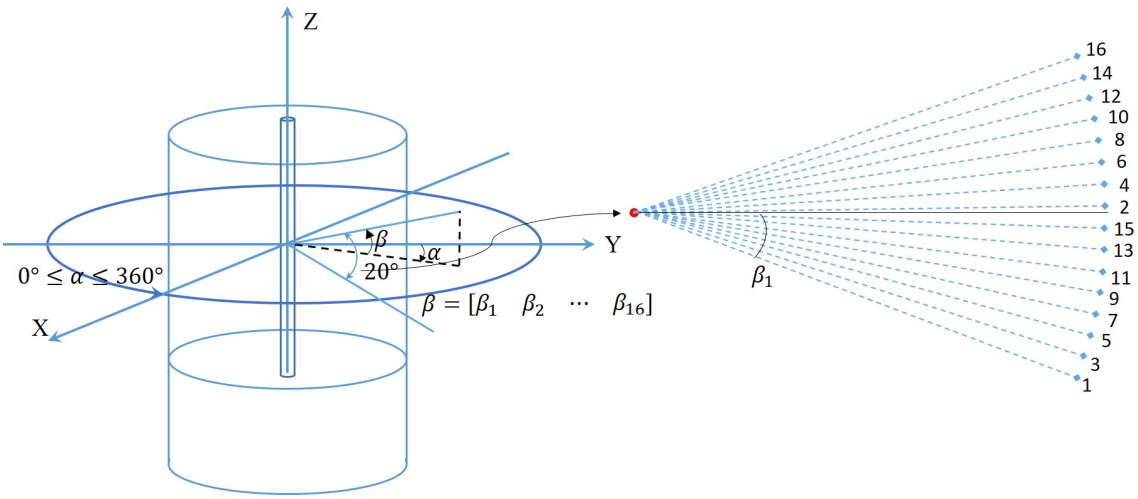

(a) Velodyne VLP16

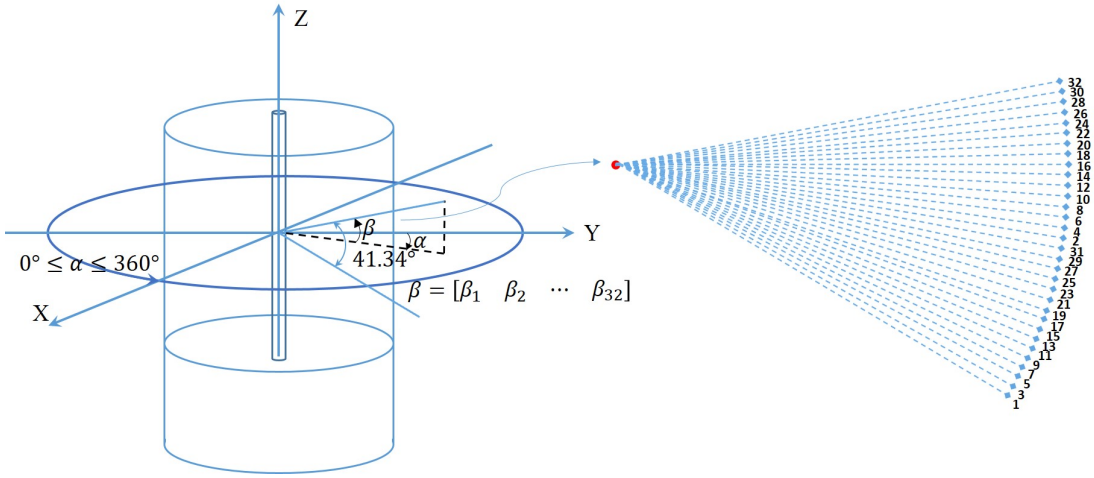

(b) Velodyne HDL32E

Fig. 2.3.: Illustration of spinning multi-beam laser scanners

$$r_I^{\mathrm{Lu}}(t) = \begin{bmatrix} x(t) \\ y(t) \\ z(t) \end{bmatrix}_I^{\mathrm{Lu}} = \begin{bmatrix} \rho(t) \ \cos\beta \ \cos\alpha(t) \\ \rho(t) \ \cos\beta \ \sin\alpha(t) \\ \rho(t) \ \sin\beta \end{bmatrix}_I^{\mathrm{Lu}} \tag{2.2}$$

In the case of a multi-unit LiDAR system, which is graphically illustrated in Figure 2.4, the point positioning equation for a given point, I, captured by the j^{th} onboard

laser scanner is given by (2.3). Here, one of the laser scanners is set as reference and the rest are considered to be slave sensors. The reference sensor (Lu_r) is related to the IMU body frame by a rigidly defined lever-arm, $r^b_{\mathrm{Lu}_r}$, and boresight matrix, $R^b_{\mathrm{Lu}_r}$. Similarly, each slave sensor (Lu_j) is related to the reference one (Lu_r) by a rigidly defined lever-arm, $r^{\mathrm{Lu}_r}_{\mathrm{Lu}_j}$, and boresight matrix, $R^{\mathrm{Lu}_r}_{\mathrm{Lu}_j}$. One should note that such a LiDAR system can also be modeled by directly relating each of the laser scanners to the IMU body frame but the current model is preferred due to the fact that it allows for the derivation of the mounting parameters relating the slave sensors to the reference one without the need for GNSS/INS position and orientation information.

$$\begin{aligned} r^m_I &= r^m_b(t) + r^m_{b\text{-}\mathrm{Lu}_r}(t) + r^m_{\mathrm{Lu}_r\text{-}\mathrm{Lu}_j}(t) + r^m_{\mathrm{Lu}_j\text{-}I}(t) \\ &= r^m_b(t) + R^m_b(t)\; r^b_{\mathrm{Lu}_r} + R^m_b(t)\; R^b_{\mathrm{Lu}_r}\; r^{\mathrm{Lu}_r}_{\mathrm{Lu}_j} + R^m_b(t)\; R^b_{\mathrm{Lu}_r}\; R^{\mathrm{Lu}_r}_{\mathrm{Lu}_j}\; r^{\mathrm{Lu}_j}_I(t) \end{aligned} \tag{2.3}$$

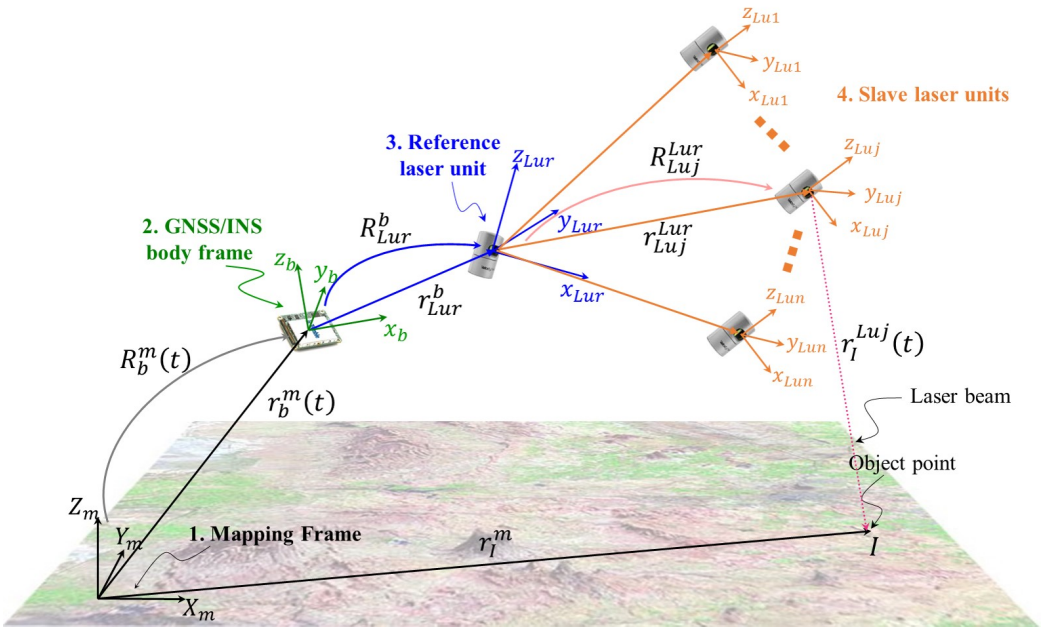

Fig. 2.4.: Illustration of point positioning for a multi-unit LiDAR system

2.5.2 Point Positioning for a GNSS/INS-assisted Multi-camera System

A typical GNSS/INS-assisted multi-camera system involves three coordinate systems (i.e., mapping frame, IMU body frame, and camera coordinate frame). A given point, I, captured in an image as point, i, from a mobile mapping system comprising multiple cameras can be reconstructed in the mapping coordinate system using (2.4), which is graphically illustrated in Figure 2.5.

$$\begin{aligned} r_I^m &= r_b^m(t) + r_{b\text{-}C_r}^m(t) + r_{C_r\text{-}C_j}^m(t) + r_{C_j\text{-}i}^m(t) \\ &= r_b^m(t) + R_b^m(t)\ r_{C_r}^b + R_b^m(t)\ R_{C_r}^b\ r_{C_j}^{C_r} + \lambda(i, C_j, t)\ R_b^m(t)\ R_{C_r}^b\ R_{C_j}^{C_r}\ r_i^{C_j}(t) \end{aligned} \tag{2.4}$$

For the camera coordinate frame, the origin is defined at the perspective center and its x, y-axes are defined along the direction of the rows and columns of the image, respectively. So, the coordinates of a point, i, in an image captured by camera, C_j, relative to the camera coordinate system, $r_i^{C_j}(t)$ are defined by (2.5). Here, x_{pj} and y_{pj} denote the location of the principal point, f_j denotes the principal distance, and $\text{dist}_{x_{ij}}$ and $\text{dist}_{y_{ij}}$ denote the distortion in image coordinate measurements for point, i in the j^{th} camera. These intrinsic parameters (x_{pj}, y_{pj}, f_j), along with the distortion parameters for C_j, are known *a priori* for a calibrated camera. For a multi-camera system, one of the cameras is set as reference and the rest are considered to be slave cameras. The reference camera (C_r) is related to the IMU body frame by a rigidly defined lever-arm, $r_{C_r}^b$, and boresight matrix, $R_{C_r}^b$. Similarly, each slave camera (C_j) is related to the reference one (C_r) by a rigidly defined lever-arm, $r_{C_j}^{C_r}$, and boresight matrix, $R_{C_j}^{C_r}$. Finally, each point, i, in an image captured by camera C_j at time t has a scaling factor associated with it, which is denoted by $\lambda(i, C_j, t)$.

$$r_I^{C_j}(t) = \begin{bmatrix} x_{ij} - x_{pj} - \text{dist}_{x_{ij}} \\ y_{ij} - y_{pj} - \text{dist}_{y_{ij}} \\ -f_j \end{bmatrix}_I^{C_j} \tag{2.5}$$

The forthcoming chapters focus on the novel multi-sensor calibration strategy proposed in this thesis and its experimental validation.

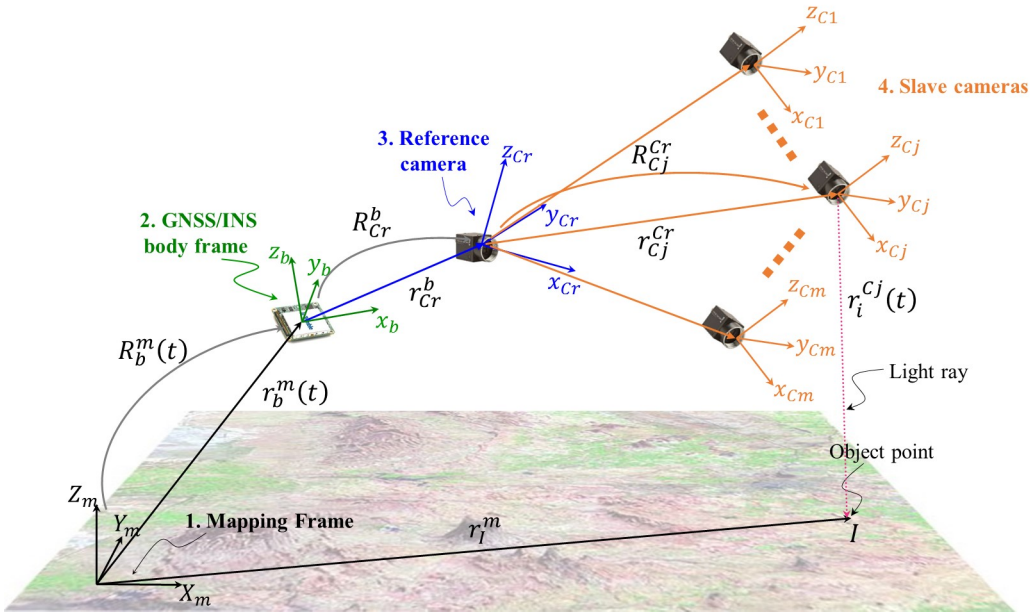

Fig. 2.5.: Illustration of point positioning for a multi-camera system

3. THEORETICAL BIAS IMPACT ANALYSIS FOR TERRESTRIAL MOBILE LIDAR SYSTEM WITH SEVERAL SPINNING MULTI-BEAM LASER SCANNERS

Before proceeding with devising a calibration strategy for mobile mapping systems, first an optimal configuration of target primitives setup and drive-runs needs to be determined to maximize the impact of the systematic errors in question, which would lead to a more accurate calibration. The objective of bias impact analysis is to derive a mathematical formulation that shows the deformations/shifts of points along planar patches (with different orientations and scanned from different drive-runs) due to the presence of bias in the system mounting parameters. This analysis is carried out for a single unit LiDAR system, which implies that all the points are acquired by the reference laser unit and hence, (2.1) will be used for conducting further theoretical analysis. It is to be noted that this analysis for single unit LiDAR systems would also be valid for multi-unit LiDAR systems as the latter can be considered as an integration of several single unit LiDAR systems together.

Planar features are specifically used for conducting this analysis because they facilitate the observation of positional deformations in one direction at a time, i.e., the effect in the direction normal to the plane. Ideally, the IMU is assumed to be perfectly vertical, i.e., the Z-axis of the IMU body frame is assumed to be perfectly aligned with the vertical direction of the mapping frame. However, this assumption might not always hold. So, in this thesis, we first conduct a bias impact analysis for the ideal scenario where the IMU is perfectly vertical and then, extend the analysis for a *nearly* vertical system, i.e., the potential tilt of the IMU body frame is incorporated in the analysis. The mathematical impact for the latter case is verified through a numerical analysis of LiDAR data captured by a spinning multi-beam laser scanner (for instance, Velodyne HDL32E).

3.1 Bias Impact Analysis: Perfectly Vertical System

For mobile mapping systems, the IMU is usually set up on the vehicle such that its X-, Y-, and Z-axes are aligned along the starboard, drive-run, and vertical directions, respectively. In other words, the IMU body frame is parallel to the vehicle coordinate system. In order to generalize the bias impact analysis regardless of the orientation of the LiDAR unit relative to the IMU/vehicle coordinate system, the LiDAR point positioning equation given by (2.1) is slightly modified by introducing a virtual LiDAR unit frame, Lu$'$, which is almost aligned with the IMU body frame (or, the vehicle coordinate system). Here, two coordinate systems are said to be "aligned" if the rotation between them is approximately zero, but this does not necessarily mean that they share the same origin. This modification facilitates determining whether the impact is along/across the drive-run and vertical directions. Moreover, the use of a virtual LiDAR unit frame also prevents gimbal lock in the mounting parameter estimation. This modification is implemented by expressing the term, R^b_{Lu} in (2.1) as: $R^b_{\text{Lu}} = R^b_{\text{Lu}'}\ R^{\text{Lu}'}_{\text{Lu}}$, where $R^{\text{Lu}'}_{\text{Lu}}$ is defined according to the laser scanner unit alignment relative to the IMU. The modified LiDAR point positioning is given by (3.1). One should note that there is no shift between the virtual and actual LiDAR unit frames, i.e., the origins of these two coordinate systems are assumed to be coinciding.

$$r^m_I = r^m_b(t) + R^m_b(t)\ r^b_{\text{Lu}} + R^m_b(t)\ R^b_{\text{Lu}'}\ R^{\text{Lu}'}_{\text{Lu}}\ r^{\text{Lu}}_I(t) \tag{3.1}$$

Since the virtual LiDAR unit frame is almost aligned with the IMU body frame, it results in small values for the differential angular boresight parameters ($\Delta\omega,\ \Delta\phi,\ \Delta\kappa$) relating the two frames. So, for such an incremental rotation, the matrix R^b_{Lu} can be approximated as shown in (3.2), using the small angle approximations. Here, $\Delta\omega,\ \Delta\phi$, and $\Delta\kappa$ denote the rotation around the X-, Y-, and Z-axes of the IMU body frame (i.e., across drive-run, along drive-run, and vertical directions), respectively. Hence, these parameters denote the boresight pitch, roll, and heading angles, respectively. The point coordinates relative to the virtual LiDAR unit frame are

given by (3.3). These coordinates (x', y', and z') also denote the location of a point with respect to the vehicle because the virtual LiDAR unit frame is almost parallel to the IMU body frame, which is parallel to the vehicle coordinate system. Thus, x', y' and z' denote the distance of a point from the laser beam firing point across the drive-run direction, along the drive-run direction, and in the vertical direction, respectively. Substituting (3.2) and (3.3) in (3.1), we get the revised form of the LiDAR point positioning equation, as given in (3.4), where ΔX, ΔY, and ΔZ are the lever-arm offset components of the LiDAR unit frame relative to the IMU body frame.

$$R^{b}_{\mathrm{Lu}} \approx \begin{bmatrix} 1 & -\Delta\kappa & \Delta\phi \\ \Delta\kappa & 1 & -\Delta\omega \\ -\Delta\phi & \Delta\omega & 1 \end{bmatrix} \tag{3.2}$$

$$r_I^{\mathrm{Lu}'} = R^{\mathrm{Lu}'}_{\mathrm{Lu}}\, r_I^{\mathrm{Lu}}(t) = \begin{bmatrix} x' \\ y' \\ z' \end{bmatrix}^{\mathrm{Lu}'}_{I} \tag{3.3}$$

$$r_I^m \approx r_b^m(t) + R_b^m(t) \begin{bmatrix} \Delta X \\ \Delta Y \\ \Delta Z \end{bmatrix}^{b}_{\mathrm{Lu}} + R_b^m(t) \begin{bmatrix} 1 & -\Delta\kappa & \Delta\phi \\ \Delta\kappa & 1 & -\Delta\omega \\ -\Delta\phi & \Delta\omega & 1 \end{bmatrix} \begin{bmatrix} x' \\ y' \\ z' \end{bmatrix}^{\mathrm{Lu}'}_{I} \tag{3.4}$$

A perfectly vertical system implies that the Z-axis of the IMU body frame is perfectly aligned with the vertical direction of the mapping frame. So, the angles ω and ϕ relating the IMU body frame and the mapping frame will be zero. Moreover, we assume that the drive-run directions are either from south-to-north ($\kappa = 0°$) or from north-to-south ($\kappa = 180°$) directions. This assumption facilitates the decision as to whether the impact is along/across the drive-run and vertical directions. As a result, the rotation matrix $R_b^m(t)$ would be given by (3.5), where the top sign is for S-N and bottom sign is for N-S drive-run directions. These assumptions would simplify the LiDAR point positioning equation to the form in (3.6). Now, the impact on mapping

frame coordinates due to the presence of bias in the system mounting parameters can be analyzed by differentiating (3.6) with respect to the system mounting parameters. This impact is given by (3.7).

$$R_b^m(t) = \begin{bmatrix} \pm 1 & 0 & 0 \\ 0 & \pm 1 & 0 \\ 0 & 0 & 1 \end{bmatrix} \tag{3.5}$$

$$r_I^m \approx r_b^m(t) + \begin{bmatrix} \pm 1 & 0 & 0 \\ 0 & \pm 1 & 0 \\ 0 & 0 & 1 \end{bmatrix} \begin{bmatrix} \Delta X \\ \Delta Y \\ \Delta Z \end{bmatrix} + \begin{bmatrix} \pm 1 & 0 & 0 \\ 0 & \pm 1 & 0 \\ 0 & 0 & 1 \end{bmatrix} \begin{bmatrix} 1 & -\Delta\kappa & \Delta\phi \\ \Delta\kappa & 1 & -\Delta\omega \\ -\Delta\phi & \Delta\omega & 1 \end{bmatrix} \begin{bmatrix} x' \\ y' \\ z' \end{bmatrix} \tag{3.6}$$

$$\delta r_I^m(\delta\Delta X,\ \delta\Delta Y,\ \delta\Delta Z,\ \delta\Delta\omega,\ \delta\Delta\phi,\ \delta\Delta\kappa) \approx \begin{bmatrix} \pm\ \delta\Delta X \\ \pm\ \delta\Delta Y \\ \delta\Delta Z \end{bmatrix} + \begin{bmatrix} \mp\ y'\ \delta\Delta\kappa \pm\ z'\ \delta\Delta\phi \\ \pm\ x'\ \delta\Delta\kappa \mp\ z'\ \delta\Delta\omega \\ -\ x'\ \delta\Delta\phi + y'\ \delta\Delta\omega \end{bmatrix} \tag{3.7}$$

Finally, the bias impact can be studied by isolating the terms in (3.7) corresponding to the bias in one of the mounting parameters at a time, as given by Table 3.1. Here, the terms $\delta\Delta X$, $\delta\Delta Y$, $\delta\Delta Z$, $\delta\Delta\omega$, $\delta\Delta\phi$, and $\delta\Delta\kappa$ denote the biases in the available values of the mounting parameters: ΔX, ΔY, ΔZ, $\Delta\omega$, $\Delta\phi$, and $\Delta\kappa$, respectively. Also, δX_m, δY_m, and δZ_m denote the impact on the mapping coordinates: X, Y, and Z, respectively. Now, Table 3.1 can be used to conduct a bias impact analysis for planar surfaces in the three main orientations (vertical planes parallel to drive-run direction, vertical planes perpendicular to drive-run direction, and horizontal planes) in order to observe the impact of each bias on one direction at a time, i.e., in the direction normal to the planes (across drive-run direction, along drive-run direction, and vertical direction). In order to quantify the effect of biases on planar surfaces, the RMSE of plane-fitting is computed separately for the planes generated in the absence of bias and those generated in the presence of bias in mounting

parameters. Here, the RMSE of plane-fitting refers to the RMSE of normal distances of the points belonging to a planar feature from the corresponding best-fitting plane determined using LSA. The change in RMSE between the two cases for each of the planes signifies the introduced deformations/discrepancies, which in turn enhances our ability for bias detection and estimation of mounting parameters. One should note that the 3D point cloud data will also have a noise associated with it, which will be implicated in the computed RMSE of the planar features. Hence, the ability to detect and estimate the bias in mounting parameters also depends on the sensor noise, i.e., a higher noise level in the data will result in less accurate estimation of biases in the mounting parameters. There are three different scenarios in terms of the drive-run configuration to be considered while evaluating the RMSE:

1. planar points scanned in a single drive-run;
2. planar points scanned in two drive-runs in same direction;
3. planar points scanned in two drive-runs in opposite directions.

Table 3.1.: Impact of bias in each of the mounting parameters on 3D point coordinates for perfectly vertical systems

	$\boldsymbol{\delta X_m}$	$\boldsymbol{\delta Y_m}$	$\boldsymbol{\delta Z_m}$
$\boldsymbol{\delta\Delta X}$	$\pm\ \delta\Delta X$	0	0
$\boldsymbol{\delta\Delta Y}$	0	$\pm\ \delta\Delta Y$	0
$\boldsymbol{\delta\Delta Z}$	0	0	$\delta\Delta Z$
$\boldsymbol{\delta\Delta\omega}$	0	$\mp\ z'\ \delta\Delta\omega$	$y'\ \delta\Delta\omega$
$\boldsymbol{\delta\Delta\phi}$	$\pm\ z'\ \delta\Delta\phi$	0	$-\ x'\ \delta\Delta\phi$
$\boldsymbol{\delta\Delta\kappa}$	$\mp\ y'\ \delta\Delta\kappa$	$\pm\ x'\ \delta\Delta\kappa$	0

The assessment of the above impacts for different plane orientations and drive-run configurations is discussed in more detail in Section 3.1.1. One should note that the

drive-run directions are assumed to be either N-S or S-N, and the mapping frame coordinate system is defined such that the X-, Y-, and Z-axes correspond to across drive-run, along drive-run, and vertical directions, respectively. However, this is only done to simplify the analysis of bias impact.

3.1.1 Perfectly Vertical System: Impact Assessment for Different Plane Orientations and Drive-run Configurations

In this subsection, we assess each of the bias impact terms listed in Table 3.1 individually in order to draw conclusions about how a bias in each of the mounting parameters would be manifested in the resultant point cloud. The hypotheses are based on four criteria:

1. Planar orientation(s) affected by the bias: Analyze whether the bias impacts the vertical planes parallel to the drive-run, vertical planes perpendicular to the drive-run, and/or horizontal planes.

2. Type of impact on planar features: Analyze whether the bias results in a constant shift of the plane, a tilt of the plane, or a varying shift of each planar point resulting in an increased scattering of the plane.

3. Impact on RMSE of a planar feature captured in a single drive-run: Analyze whether the bias results in an increase in the RMSE of feature fitting for a planar feature that is captured within a single drive-run.

4. Impact on RMSE of a planar feature captured in two drive-runs: Analyze whether the bias results in an increase in the feature-fitting RMSE computed using the points along a planar feature captured by two drive-runs in same or opposite direction. Also, check whether the impact is a function of the relative drive-run direction, the lateral separation between the two drive-runs, and/or the lateral distance of the planar feature from the drive-runs.

Now, we proceed to analyze the impact of a bias in each of the six mounting parameters one-by-one to make an inference regarding the impact with respect to each of the above criteria based on the resultant bias impact terms listed in Table 3.1.

1. *Impact of Bias in Lever-arm Component Across the Drive-run Direction* (ΔX)*:* A bias in this component ($\delta\Delta X$) will introduce a constant shift ($\pm\ \delta\Delta X$) across the drive-run direction, as shown schematically in Figure 3.1. The introduced shift is drive-run direction dependent the two signs in the impact term correspond to opposite drive-run directions, as mentioned earlier in Section 3.1. The different signs imply that the shift of planar feature will be in opposite directions for the points captured along the feature from two opposite drive-runs. The resultant shift does not depend on the location of the point in question relative to the laser beam firing point, i.e., the shift of the point is independent of x', y', and z'. As a result, the RMSE for all the planes scanned from a single drive-run or two drive-runs in same direction will remain the same whether or not there is a bias in this parameter. On the other hand, in case of planes scanned from two drive-runs in opposite directions, the RMSE of normal distance of the points from the corresponding best-fitting plane will maximally increase for vertical planes parallel to the drive-run direction due to the points captured from each drive-run shifted in opposite directions.

2. *Impact of Bias in Lever-arm Component Along the Drive-run Direction* (ΔY)*:* A bias in this component ($\delta\Delta Y$) will introduce a constant shift ($\pm\ \delta\Delta Y$) along the drive-run direction, as shown schematically in Figure 3.2. The introduced shift is drive-run direction dependent. It does not depend on the location of the point in question relative to the laser beam firing point. Again, the RMSE for all the planes scanned from a single drive-run or two drive-runs in same direction will remain the same whether or not there is a bias in this parameter. On the other hand, in case of planes scanned from two drive-runs in opposite directions,

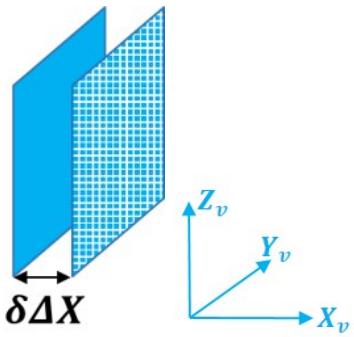

Fig. 3.1.: Schematic impact of bias in ΔX on a vertical plane parallel to drive-run direction

the RMSE will maximally increase for the vertical planes perpendicular to the drive-run direction.

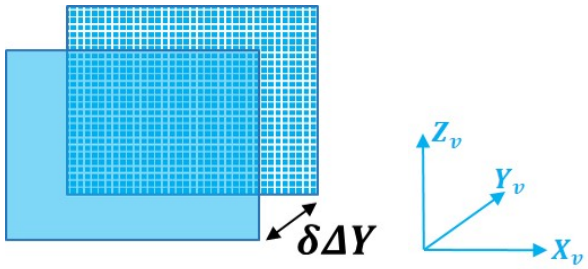

Fig. 3.2.: Schematic impact of bias in ΔY on a vertical plane perpendicular to drive-run direction

3. *Impact of Bias in Lever-arm Component in the Vertical Direction* (ΔZ)*:* A bias in this component ($\delta\Delta Z$) will introduce a constant shift ($\delta\Delta Z$) in the vertical direction. The introduced shift is drive-run direction independent. It does not depend on the location of the point in question relative to the laser beam firing point. As a result, the entire point cloud would be shifted in the vertical direction by the same amount. So, this bias would not affect the RMSE of planes in any of the orientations for any drive-run configuration.

4. *Impact of Bias in Boresight Pitch* ($\Delta\omega$)*:*

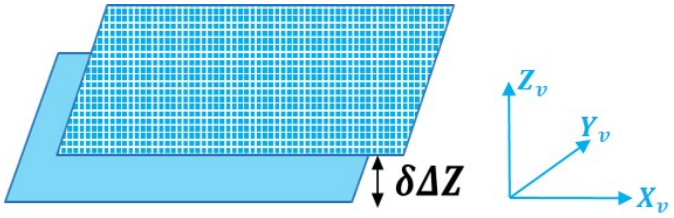

Fig. 3.3.: Schematic impact of bias in ΔZ on a horizontal plane

(a) *Shift along drive-run direction:* The impact of boresight pitch bias along the drive-run direction ($\pm\ z'\ \delta\Delta\omega$) is drive-run direction dependent and its magnitude depends on the height (z') of the point in question relative to the laser beam firing point. Whenever the height and boresight pitch bias are small, this impact might be insignificant. In case of vertical planes perpendicular to the drive-run direction scanned from a single track, all the points lying at the same height will be shifted by the same amount along the drive-run direction, thus resulting in a tilt in the plane, as shown schematically in Figure 3.4. So, the RMSE will not be affected by this term. Similarly, the RMSE will remain the same on combining two tracks in the same direction. But, since this shift is drive-run direction dependent, this would result in an increase in RMSE of the planes on combining two tracks in opposite directions.

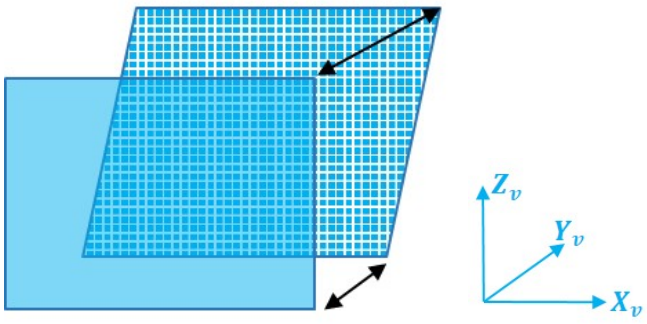

Fig. 3.4.: Schematic impact of bias in $\Delta\omega$ on a vertical plane perpendicular to drive-run direction

(b) *Shift in vertical direction:* The impact of boresight pitch bias in the vertical direction ($y'\ \delta\Delta\omega$) depends on the y'-coordinate of the point in question, i.e., the shift for each point is dependent on its distance along the drive-run direction from the laser beam firing point. So, all the points belonging to a planar patch will be shifted by different amounts as each point might have a different y' value depending on the instantaneous location of the vehicle when the point was scanned. This would cause an increase in RMSE of horizontal planes for a single track, which in turn will lead to a large RMSE on combining tracks oriented in same or opposite directions.

5. *Impact of Bias in Boresight Roll* ($\Delta\phi$)*:*

(a) *Shift across drive-run direction:* The impact of this bias across the drive-run direction ($\pm\ z'\ \delta\Delta\phi$) is drive-run direction dependent and its magnitude depends on the height (z') of the point in question relative to the laser beam firing point. Whenever the height and boresight roll bias are small, this impact might be insignificant. In case of vertical planes parallel to the drive-run direction scanned from a single track, all the points lying at the same height will be shifted by the same amount across the drive-run direction, thus resulting in a tilt in the plane, as shown schematically in Figure 3.5. So, the RMSE for a single track will not be affected by this term. Similarly, the RMSE will remain the same on combining two tracks in the same direction. But, since the shift is drive-run direction dependent, this would result in an increase in RMSE of the planes on combining two tracks in opposite directions.

(b) *Shift in vertical direction:* The impact of this bias in the vertical direction ($-\ x'\ \delta\Delta\phi$) is drive-run direction dependent and its magnitude depends on the x'-coordinate of the point in question. In case of horizontal planes scanned from a single track, all the points located at the same lateral distance from the track will be shifted vertically by the same amount,

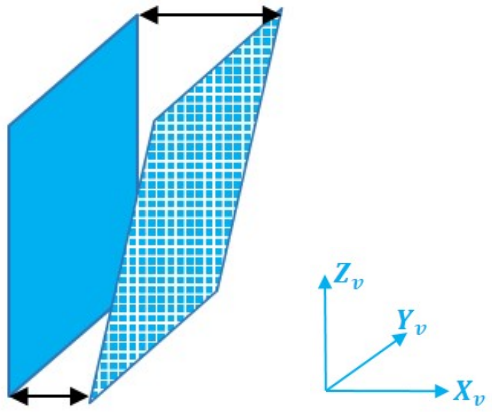

Fig. 3.5.: Schematic impact of bias in $\Delta\phi$ on a vertical plane parallel to drive-run direction

thus resulting in a tilt in the plane, as shown schematically in Figure 3.6. So, the RMSE for single tracks will not be affected by this term. Now, using Figure 3.7 as reference, the discrepancies in the vertical direction on combining two tracks in the same direction and in opposite directions are given by (3.8) and (3.9), respectively. The term X in (3.9) denotes the distance of the point from the line bisecting the lateral distance between the two drive-runs, as can be seen in Figure 3.7. Hence, for two tracks in the same direction, the RMSE will increase according to the lateral distance between the tracks. On the other hand, for two tracks in opposite directions, RMSE will increase depending on the lateral location of the planar patch of interest relative to the bisecting direction between the tracks.

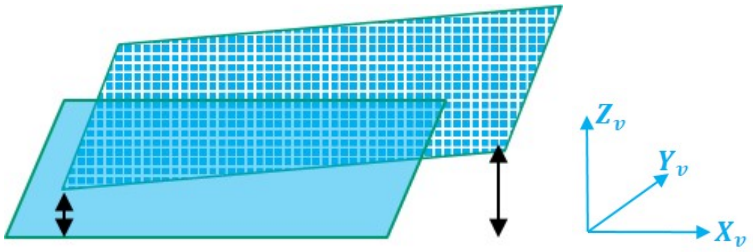

Fig. 3.6.: Schematic impact of bias in $\Delta\phi$ on a horizontal plane

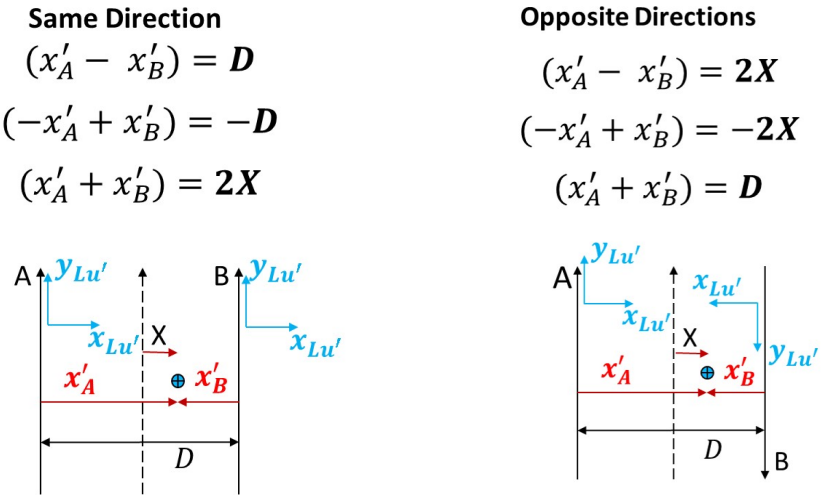

(a) Two drive-runs in same direction

(b) Two drive-runs in opposite directions

Fig. 3.7.: Relationship between x'-coordinates for a point captured by two drive-runs in same and opposite directions

$$\text{Same Direction: } \delta Z_{m_A} - \delta Z_{m_B} = (-x'_A + x'_B)\ \delta\Delta\phi = -D_{AB}\ \delta\Delta\phi \tag{3.8}$$

$$\text{Opposite Directions: } \delta Z_{m_A} - \delta Z_{m_B} = (-x'_A + x'_B)\ \delta\Delta\phi = -2X\ \delta\Delta\phi \tag{3.9}$$

6. *Impact of Bias in Boresight Heading* ($\Delta\kappa$)*:*

   (a) *Shift across drive-run direction:* The impact of this bias across the drive-run direction ($\mp\ y'\ \delta\Delta\kappa$) is y'-coordinate dependent. So, this would cause an increase in RMSE for the vertical planes parallel to the drive-run direction for a single track. Moreover, the RMSE on combining two tracks in same or opposite directions would depend on the $\mp\ y'$ variability within the points comprising the planes.

   (b) *Shift along drive-run direction:* The impact of this bias along the drive-run direction ($\pm\ x'\ \delta\Delta\kappa$) is drive-run direction independent since the dual signs will be nullified by x', which will also have opposite signs for two tracks in opposite directions. Also, the shift for each point is dependent on its x'-coordinate. However, in case of vertical planes perpendicular to the drive-run direction, the RMSE for a single track would not be affected as the presence of this bias would only cause a tilt in the planar surface, as shown schematically in Figure 3.8. Again, referring to Figure 3.7, the discrepancies along the drive-run direction on combining two tracks in the same direction and in opposite directions are given by (3.10) and (3.11), respectively. So, it can be concluded that the RMSE on combining two tracks in the same or opposite directions would increase according to the lateral distance between the tracks.

$$\text{Same Direction: } \delta Y_{m_A} - \delta Y_{m_B} = (x'_A - x'_B)\ \delta\Delta\kappa = D_{AB}\ \delta\Delta\kappa \tag{3.10}$$

$$\text{Opposite Directions: } \delta Y_{m_A} - \delta Y_{m_B} = (x'_A + x'_B)\ \delta\Delta\kappa = D_{AB}\ \delta\Delta\kappa \tag{3.11}$$

Table 3.2 summarizes the above discussion by listing whether the RMSE of plane fitting on introducing a bias in mounting parameters ($\text{RMSE}_{\text{Bias}}$) would potentially increase or remain the same as compared to the RMSE from the original point cloud

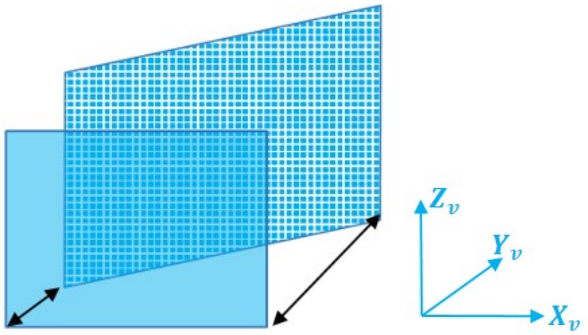

Fig. 3.8.: Schematic impact of bias in $\Delta\kappa$ on a vertical plane perpendicular to drive-run direction

($\text{RMSE}_{\text{True}}$) for different plane orientations and drive-run configurations in case of a perfectly vertical system.

3.2 Bias Impact Analysis: Nearly Vertical System

A nearly vertical system implies that the Z-axis of the IMU body frame is not perfectly aligned with the vertical direction of the mapping frame, i.e., the IMU unit has a slight tilt along and/or across the drive-run direction. Let these tilt values be denoted by $D\omega$ and $D\phi$, respectively. Again, under the assumption that the drive-run directions are either in S-N or N-S directions, the rotation matrix $R_b^m(t)$ for a nearly vertical system would be given by (3.12) (using the small angle approximations for the IMU tilt angles).

$$R_b^m(t) \approx \begin{bmatrix} \pm 1 & 0 & \pm D\phi \\ 0 & \pm 1 & \mp D\omega \\ -D\phi & D\omega & 1 \end{bmatrix} \tag{3.12}$$

Substituting the newly derived expression of the rotation matrix $R_b^m(t)$ for a nearly vertical system in (3.6), the revised form of the LiDAR point positioning equation is obtained for nearly vertical systems, as given in (3.13). Now, the impact on mapping frame coordinates due to the presence of bias in the system mounting parameters can

Table 3.2.: Potential qualitative impact on RMSE of plane fitting based on the theoretical bias impact analysis for perfectly vertical systems

Bias Type	**Plane Orientation**	**Vertical & Parallel to Drive-run Direction**	**Vertical & Perpendicular to Drive-run Direction**	**Horizontal Planes**
	Normal Direction	**Across Drive-run Direction**	**Along Drive-run Direction**	**Vertical Direction**
	Drive-run Configuration			
$\delta\Delta X$	Single Track	Same	Same	Same
	Two Tracks (Same Direction)	Same	Same	Same
	Two Tracks (Opposite Directions)	Increase	Same	Same
$\delta\Delta Y$	Single Track	Same	Same	Same
	Two Tracks (Same Direction)	Same	Same	Same
	Two Tracks (Opposite Directions)	Same	Increase	Same
$\delta\Delta Z$	Single Track	Same	Same	Same
	Two Tracks (Same Direction)	Same	Same	Same
	Two Tracks (Opposite Directions)	Same	Same	Same
$\delta\Delta\omega$	Single Track	Same	Same	Increase
	Two Tracks (Same Direction)	Same	Same	Increase
	Two Tracks (Opposite Directions)	Same	Increase	Increase
$\delta\Delta\phi$	Single Track	Same	Same	Same
	Two Tracks (Same Direction)	Same	Same	Increase
	Two Tracks (Opposite Directions)	Increase	Same	Increase
$\delta\Delta\kappa$	Single Track	Increase	Same	Same
	Two Tracks (Same Direction)	Increase	Increase	Same
	Two Tracks (Opposite Directions)	Increase	Increase	Same

be analyzed by differentiating (3.13) with respect to the system mounting parameters. This impact is given by (3.14).

$$
\begin{aligned}
r_I^m = r_b^m(t) + &\begin{bmatrix} \pm 1 & 0 & \pm D\phi \\ 0 & \pm 1 & \mp D\omega \\ -D\phi & D\omega & 1 \end{bmatrix} \begin{bmatrix} \Delta X \\ \Delta Y \\ \Delta Z \end{bmatrix} \\
&+ \begin{bmatrix} \pm 1 & 0 & \pm D\phi \\ 0 & \pm 1 & \mp D\omega \\ -D\phi & D\omega & 1 \end{bmatrix} \begin{bmatrix} 1 & -\Delta\kappa & \Delta\phi \\ \Delta\kappa & 1 & -\Delta\omega \\ -\Delta\phi & \Delta\omega & 1 \end{bmatrix} \begin{bmatrix} x' \\ y' \\ z' \end{bmatrix}
\end{aligned} \tag{3.13}
$$

$$
\begin{aligned}
\delta r_I^m(\delta\Delta X,\ \delta\Delta Y,\ \delta\Delta Z,\ \delta\Delta\omega,\ \delta\Delta\phi,\ \delta\Delta\kappa) = &\begin{bmatrix} \pm\ \delta\Delta X \\ \pm\ \delta\Delta Y \\ \delta\Delta Z \end{bmatrix} \\
+ &\begin{bmatrix} \pm\ y'\ D\phi\ \delta\Delta\omega\ \pm\ z'\ \delta\Delta\phi\ \mp\ x'\ D\phi\ \delta\Delta\phi\ \mp\ y'\ \delta\Delta\kappa \\ \mp\ z'\ \delta\Delta\omega\ \mp\ y'\ D\omega\ \delta\Delta\omega\ \pm\ x'\ D\omega\ \delta\Delta\phi\ \pm\ x'\ \delta\Delta\kappa \\ y'\ \delta\Delta\omega\ -\ z'\ D\omega\ \delta\Delta\omega\ -\ x'\ \delta\Delta\phi\ -\ z'\ D\phi\ \delta\Delta\phi\ +\ x'\ D\omega\ \delta\Delta\kappa\ +\ y'\ D\phi\ \delta\Delta\kappa \end{bmatrix}
\end{aligned} \tag{3.14}
$$

The bias impact analysis previously conducted for perfectly vertical systems constitutes the first part of bias impact for nearly vertical systems and it can be extended further to derive the total impact for such systems by focusing on the additional terms that are introduced in (3.14) as compared to (3.7). Table 3.3 lists the impact for a nearly vertical system corresponding to a bias in one of the mounting parameters at a time. Here, the additional terms as compared to a perfectly vertical system are highlighted in red.

3.2.1 Nearly Vertical System: Impact Assessment for Different Plane Orientations and Drive-run Configurations

1. *Impact of Bias in Boresight Pitch* ($\Delta\omega$)*:*

   (a) *Shift across drive-run direction:* The impact of boresight pitch bias across the drive-run direction due to the additional term introduced for a nearly

Table 3.3.: Impact of bias in each of the mounting parameters on 3D point coordinates for nearly vertical systems

	$\boldsymbol{\delta X_m}$	$\boldsymbol{\delta Y_m}$	$\boldsymbol{\delta Z_m}$
$\boldsymbol{\delta\Delta X}$	$\pm\ \delta\Delta X$	0	0
$\boldsymbol{\delta\Delta Y}$	0	$\pm\ \delta\Delta Y$	0
$\boldsymbol{\delta\Delta Z}$	0	0	$\delta\Delta Z$
$\boldsymbol{\delta\Delta\omega}$	$\pm\ y'\ D\phi\ \delta\Delta\omega$	$\mp\ z'\ \delta\Delta\omega\ \mp\ y'\ D\omega\ \delta\Delta\omega$	$y'\ \delta\Delta\omega\ -\ z'\ D\omega\ \delta\Delta\omega$
$\boldsymbol{\delta\Delta\phi}$	$\pm\ z'\ \delta\Delta\phi\ \mp\ x'\ D\phi\ \delta\Delta\phi$	$\pm\ x'\ D\omega\ \delta\Delta\phi$	$-\ x'\ \delta\Delta\phi\ -\ z'\ D\phi\ \delta\Delta\phi$
$\boldsymbol{\delta\Delta\kappa}$	$\mp\ y'\ \delta\Delta\kappa$	$\pm\ x'\ \delta\Delta\kappa$	$x'\ D\omega\ \delta\Delta\kappa\ +\ y'\ D\phi\ \delta\Delta\kappa$

vertical systems ($\pm\ y'\ D\phi\ \delta\Delta\omega$) is y'-coordinate dependent, i.e., the shift for each point is dependent on its distance along the drive-run direction from the laser beam firing point. This would cause an increase in RMSE of vertical planes parallel to the drive-run direction for a single track. However, this increase would be negligible as $D\phi$ and $\delta\Delta\omega$ are very small and so, the shift $y'\ D\phi\ \delta\Delta\omega$ would be small unless the y'-coordinate for the planar points is large enough. Furthermore, the RMSE on combining two tracks in the same or opposite directions would depend on the $\pm\ y'$ variability within the point comprising the planes.

(b) *Shift along drive-run direction:* The impact of boresight pitch bias along the drive-run direction due to the additional term introduced for a nearly vertical system ($\mp\ y'\ D\omega\ \delta\Delta\omega$) is y'-coordinate dependent. This would cause an increase in RMSE of the planes perpendicular to the drive-run direction for a single track. However, this increase would be negligible as $D\omega$ and $\delta\Delta\omega$ are very small and so, the shift $y'\ D\omega\ \delta\Delta\omega$ would be small unless the y'-coordinate for the planar points is large enough. Also,

the RMSE on combining two tracks in same or opposite directions would depend on the $\pm\ y'$ variability within the point comprising the planes.

(c) *Shift in vertical direction:* The additional impact of boresight pitch bias in the vertical direction ($-\ z'\ D\omega\ \delta\Delta\omega$) is drive-run direction independent but depends on the height (z') of the point in question relative to the laser beam firing point. For a horizontal plane, z'-coordinate of all points will be almost same. So, this term will not impact the RMSE of horizontal planes for any of the three drive-run configurations.

2. *Impact of Bias in Boresight Roll* ($\Delta\phi$)*:*

(a) *Shift across drive-run direction:* The additional impact of this bias across the drive-run direction for a nearly vertical system ($\mp\ x'\ D\phi\ \delta\Delta\phi$) is drive-run direction independent. Also, the shift for each point is dependent on its distance across the drive-run direction from the laser scanner trajectory (x'). However, in case of vertical planes parallel to the drive-run direction, x'-coordinate of all the points will be almost the same. So, the RMSE of such planes will not change for single tracks. However, on combining two tracks (say, A and B) in the same direction (Figure 3.7(a)), the discrepancy across the drive-run direction for a point scanned in the two tracks is given by (3.15). Similarly, on combining two tracks in opposite directions (Figure 3.7(b)), the discrepancy across the drive-run direction is given by (3.16). Here, D_{AB} denotes the lateral distance between the two tracks. Hence, the RMSE on combining two tracks in the same or opposite directions would increase according to the lateral distance between the tracks.

$$\text{Same Direction:} \quad \begin{aligned} \delta X_{m_A} - \delta X_{m_B} &= (-x'_A + x'_B)\ D\phi\ \delta\Delta\phi \\ &= -D_{AB}\ D\phi\ \delta\Delta\phi \end{aligned} \tag{3.15}$$

$$\text{Opposite Directions:} \quad \begin{aligned} \delta X_{m_A} - \delta X_{m_B} &= (-x'_A - x'_B)\ D\omega\ \delta\Delta\phi \\ &= -D_{AB}\ D\omega\ \delta\Delta\phi \end{aligned} \tag{3.16}$$

(b) *Shift along drive-run direction:* The impact of this bias along the drive-run direction for nearly vertical systems ($\pm\ x'\ D\omega\ \delta\Delta\phi$) is drive-run direction independent. Also, the shift for each point is dependent on its x'-coordinate. For a vertical plane perpendicular to the drive-run direction, all the points which have the same lateral distance will be shifted by the same amount along the drive-run direction. This would only cause a tilt in the planar surface and thus, it would not affect its RMSE when dealing with a single drive-run. Furthermore, referring to Figure 3.7, the discrepancies along the drive-run direction on combining two tracks in the same direction and in opposite directions are given by (3.17) and (3.18), respectively. So, it can be concluded that the RMSE on combining two tracks in same or opposite directions would increase according to the lateral distance between the tracks.

$$\text{Same Direction:} \quad \begin{aligned} \delta Y_{m_A} - \delta Y_{m_B} &= (x'_A - x'_B)\ D\omega\ \delta\Delta\phi \\ &= D_{AB}\ D\omega\ \delta\Delta\phi \end{aligned} \tag{3.17}$$

$$\text{Opposite Directions:} \quad \begin{aligned} \delta Y_{m_A} - \delta Y_{m_B} &= (x'_A + x'_B)\ D\omega\ \delta\Delta\phi \\ &= D_{AB}\ D\omega\ \delta\Delta\phi \end{aligned} \tag{3.18}$$

(c) *Shift in vertical direction:* The additional impact of this bias in the vertical direction ($-\ z'\ D\phi\ \delta\Delta\phi$) is drive-run direction independent. Also, the shift for each point is dependent on its height (z') relative to the laser beam firing point. For a horizontal plane, z'-coordinate of all the points will be almost

same. So, this term will not impact the RMSE of horizontal planes for any of the three drive-run configurations.

3. *Impact of Bias in Boresight Heading* ($\Delta\kappa$)*:*

   (a) *Shift in vertical direction:* The additional impact of this bias in the vertical direction that is introduced for a nearly vertical system consists of two terms. The shift caused by the first term ($x'\ D\omega\ \delta\Delta\kappa$) is drive-run direction dependent and its magnitude depends on the x'-coordinate of the point in question. In case of horizontal planes scanned from a single track, all the points located at the same lateral distance from the track will be shifted vertically by the same amount, thus resulting in a tilt in the plane. So, the RMSE for single tracks will not be affected by this term. Now, according to Figure 3.7, the discrepancies along the drive-run direction on combining two tracks in the same direction and in opposite directions are given by (3.19) and (3.20), respectively. Hence, for two tracks in the same direction, the RMSE will increase according to the lateral distance between the tracks. On the other hand, for two tracks in opposite directions, RMSE will increase depending on the extent of the lateral distance variability of the planar patch of interest relative to the bisecting direction between the tracks.

$$\text{Same Direction:} \quad \begin{aligned} \delta Z_{m_A} - \delta Z_{m_B} &= (x'_A - x'_B)\ D\omega\ \delta\Delta\kappa \\ &= D_{AB}\ D\omega\ \delta\Delta\kappa \end{aligned} \tag{3.19}$$

$$\text{Opposite Directions:} \quad \begin{aligned} \delta Z_{m_A} - \delta Z_{m_B} &= (x'_A - x'_B)\ D\omega\ \delta\Delta\kappa \\ &= 2X\ D\omega\ \delta\Delta\kappa \end{aligned} \tag{3.20}$$

Now, the shift caused by the second term ($y'\ D\phi\ \delta\Delta\kappa$) is y'-coordinate dependent. So, this would cause an increase in RMSE of the horizontal planes for a single track, which in turn will lead to an increase in RMSE

on combining tracks oriented in the same or opposite directions. However, this increase would be negligible as $D\phi$ and $\delta\Delta\kappa$ are very small and so, the shift $y'\ D\phi\ \delta\Delta\kappa$ would be small unless the y'-coordinate for the planar points is large enough.

Note that throughout the above discussion, we refer to the coordinates or bias values being "small" or "large enough". In this context, a coordinate or bias is considered "small" if its impact on the point cloud lies within the limits of the expected accuracy in point positioning according to the specifications of the hardware components included in the mobile mapping system, i.e., the LiDAR and GNSS/INS units. Similarly, a coordinate or bias is considered "large enough" if the resultant bias impact is beyond the expected accuracy in point positioning.

Table 3.4 summarizes whether the RMSE of plane fitting on introducing a bias in mounting parameters ($\text{RMSE}_{\text{Bias}}$) would potentially increase or remain the same as compared to the RMSE from the original point cloud ($\text{RMSE}_{\text{True}}$) for different plane orientations and drive-run configurations by combining the additional bias impact introduced in case of nearly vertical systems with the already existing bias impact terms for perfectly vertical systems. One should note that Table 3.4 consists of some cases where it is listed that the RMSE of plane fitting "might increase" as a result of the bias. This uncertainty arises because of second order bias impact terms, which are dependent on the y' coordinates of the points (as discussed previously), thus indicating that the RMSE would increase only in cases with large y'-coordinate values or large y'-variability of the planar feature points.

The above analysis can be used to draw conclusions about the target primitives and drive-run configurations required to estimate each mounting parameter:

1. The lever-arm ΔX can be estimated using opposite drive-runs while scanning vertical planar features parallel to the drive-run direction.

2. The lever-arm ΔY can be estimated using opposite drive-runs while scanning vertical planar features perpendicular to the drive-run direction.

Table 3.4.: Potential qualitative impact on RMSE of plane fitting based on the theoretical bias impact analysis for nearly vertical systems

Bias Type	Plane Orientation	Vertical & Parallel to Drive-run Direction	Vertical & Perpendicular to Drive-run Direction	Horizontal Planes
	Normal Direction	Across Drive-run Direction	Along Drive-run Direction	Vertical Direction
	Drive-run Configuration			
$\delta\Delta X$	Single Track	Same	Same	Same
	Two Tracks (Same Direction)	Same	Same	Same
	Two Tracks (Opposite Directions)	Increase	Same	Same
$\delta\Delta Y$	Single Track	Same	Same	Same
	Two Tracks (Same Direction)	Same	Same	Same
	Two Tracks (Opposite Directions)	Same	Increase	Same
$\delta\Delta Z$	Single Track	Same	Same	Same
	Two Tracks (Same Direction)	Same	Same	Same
	Two Tracks (Opposite Directions)	Same	Same	Same
$\delta\Delta\omega$	Single Track	Might increase	Might increase	Increase
	Two Tracks (Same Direction)	Might increase	Might increase	Increase
	Two Tracks (Opposite Directions)	Might increase	Increase	Increase
$\delta\Delta\phi$	Single Track	Same	Same	Same
	Two Tracks (Same Direction)	Increase	Increase	Increase
	Two Tracks (Opposite Directions)	Increase	Increase	Increase
$\delta\Delta\kappa$	Single Track	Increase	Same	Same
	Two Tracks (Same Direction)	Increase	Increase	Increase
	Two Tracks (Opposite Directions)	Increase	Increase	Increase

3. The lever-arm ΔZ for a given spinning multi-beam laser scanner can be estimated only using vertical control.

4. The boresight pitch ($\Delta\omega$) can be estimated using horizontal planar features in addition to using two opposite drive-runs while scanning vertical planar features perpendicular to the drive-run direction. The height of the planar features is critical to decouple this parameter from the lever-arm ΔY.

5. The boresight roll ($\Delta\phi$) can be estimated using two opposite drive-runs while scanning vertical planar features parallel to the drive-run direction. The height

of the planar features is critical to decouple this parameter from the lever-arm ΔX. The setup should also include horizontal planar features scanned from opposite drive-runs at different lateral distances from the features and scanned from drive-runs in the same direction but with different lateral separations.

6. The boresight heading ($\Delta\kappa$) can be estimated by scanning vertical planes from two drive-runs in the same direction with a significant lateral separation between them. This configuration would eliminate any discrepancies caused by lever-arm components. This setup should also include horizontal planar features scanned from opposite drive-runs at different lateral distances from the features and scanned from drive-runs in the same direction but with different lateral separations.

3.3 Experimental Results

3.3.1 System Integration and Synchronization Process

In order to experimentally validate the theoretical bias impact analysis, a car-mount system (shown in Figure 3.9) is used to collect LiDAR data for 3D point cloud reconstruction. In this regard, system integration is considered one of the factors that have a significant effect on the ability to provide accurate geospatial information. This system consists of a Velodyne HDL32E sensor and a direct georeferencing unit based on an integrated INS and GNSS receiver boards (SPAN-CPT). All these components are rigidly fixed within the car-mount system. According to manufacturer specifications, the range accuracy of Velodyne HDL32E is 2 cm. Also, for the SPAN-CPT, the postprocessing accuracy in position can be less than 2 cm and the achieved accuracy for the roll/pitch and heading can be 0.008° and 0.025°, respectively. Based on error propagation calculation using these specified accuracies of the involved hardware, we should expect a point positioning accuracy of around 2 cm in the derived 3D coordinates for points captured using this system.

Fig. 3.9.: Car-mount MMS

In order to derive direct georeferencing data, the SPAN-CPT supplies sequentially precise time pulses, known as pulse-per-second signals, which give the ability to generate a time-tagged point cloud. Furthermore, the SPAN-CPT provides a navigation message, also known as GPRMC message (including information regarding position, rotation, and GPS time), which is recorded over a dedicated RS-232 serial port and received by the LiDAR unit via the interface box in the form of serial data. This synchronization process is illustrated in Figure 3.10.

3.3.2 Experimental Verification of Bias Impact Analysis

The numerical verification of the theoretical impact for a nearly vertical system is done by first, extracting vertical planes that are parallel or perpendicular to the drive-run direction, and horizontal planes from a point cloud obtained using a pre-calibrated system that is assumed to have no biases in the system mounting parameters. Then,

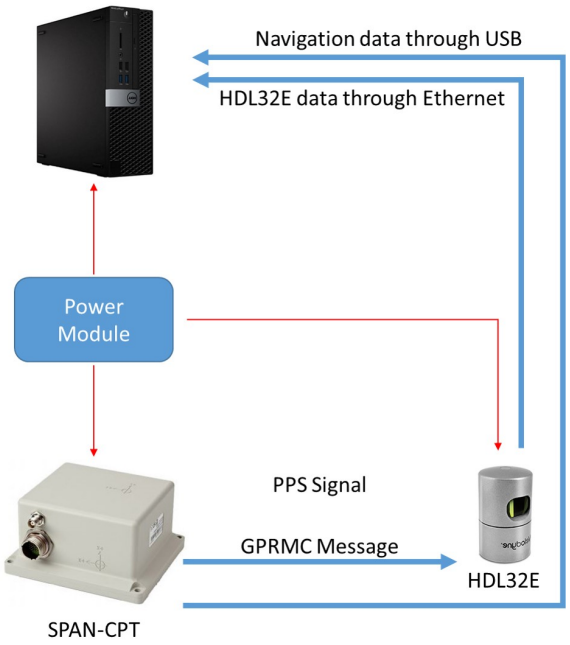

Fig. 3.10.: Synchronization process and data storage for the car-mount MMS

for each of the planar features, the RMSE of normal distances of the points from the best-fitting plane are determined to describe the quality of fit for these planes before adding biases to the system mounting parameters. Next, a bias is introduced in the system mounting parameters, one by one, and the point clouds are reconstructed for each case. For this research, the bias introduced in the lever-arm components is 20 cm, and the bias introduced in the boresight angles is 120 arc-min. These values for simulated bias are chosen to be large enough to amplify the numerical impact on the RMSE of plane fitting in order to draw conclusions whether the impact of simulated biases validate the theoretically determined bias impact for the different target and drive-run configurations. Finally, the RMSE values for the planar features are estimated for the individual drive-runs as well as combined drive-runs with different configurations. These values are compared with the original RMSE values to verify the hypotheses about the impact of various biases in the system mounting parameters. Four different drive-run configurations are used for this research: a pair of drive-runs

in the same direction and opposite directions at two different lateral distances for each case, schematically shown in Figure 3.11. The target primitives and the relative location of the drive-runs that are used to observe the impact of biases are depicted in Figure 3.12, along with the orientation of these calibration primitives relative to the drive-runs. Here, G0∼G2 are ground patches, B0∼B4 are highly reflective sign boards, and W1 is a wall patch. The orientation of mapping frame is also indicated in the top left corner of Figure 3.12 as X_m and Y_m.

Fig. 3.11.: Drive-run configurations for bias impact analysis

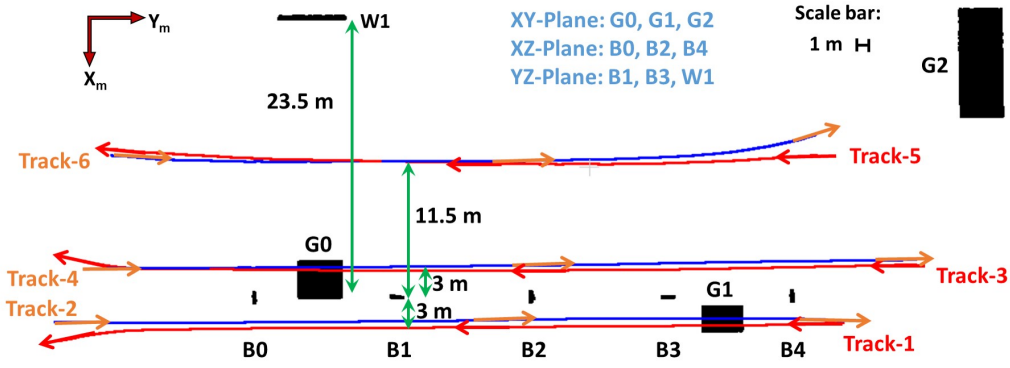

Fig. 3.12.: Target primitives and drive-runs used for bias impact analysis

Tables 3.5, 3.6, and 3.7 list the RMSE of plane fitting (in meters) for the target primitives in each of the three orientations (YZ, XZ, and XY), respectively, for the four drive-run configurations. The RMSE is listed for each track separately (where Track A denotes the first track and Track B denotes the second track in the

corresponding configuration) as well as for the two tracks combined together. The values in green denote the RMSE of plane fitting for the planar feature reconstructed with no simulated bias in any of the mounting parameters. These RMSE values with unbiased mounting parameters computed for each track separately and for combined tracks in each configuration will be used as the reference to quantify the increase in RMSE values for the different drive-run configurations when a bias is introduced in the mounting parameters. The values highlighted in yellow denote the ones which can be expected to have a potential increase in RMSE according to the theoretical analysis. It is worth mentioning that all the nine target primitives which were used for experimental validation upheld the theoretically derived hypotheses, i.e., each set of planar features – (B1, B3, W1); (B0, B2, B4); and (G0, G1, G2) – oriented in the same direction with respect to the drive-run direction are seen to exhibit similar trends (in keeping with the expected impact based on their lateral separation from the drive-runs). Table 3.5 indicates that vertical planes parallel to the drive-run direction would aid in estimating ΔX, $\Delta\phi$, and $\Delta\kappa$, along with a relatively weaker contribution toward $\Delta\omega$. Table 3.6 indicates that vertical planes perpendicular to the drive-run direction would facilitate the estimation of ΔY, $\Delta\omega$, and, $\Delta\kappa$, along with a weaker contribution toward $\Delta\phi$. Also, Table 3.7 indicates that horizontal planes would indeed help in estimating $\Delta\omega$ and $\Delta\phi$, along with a lesser contribution toward $\Delta\kappa$. The values highlighted in red in Tables 3.5 and 3.7 indicate a significant increase in the RMSE for Tracks 5 and 6. However, this is not expected theoretically. This is attributed to the points of the planar patch that are captured toward the curved ends of the trajectories, thus leading to a significant change in their x'-coordinates, which is otherwise assumed to be constant in case of straight tracks capturing such patches. These results reveal that the numerical results validate the theoretically drawn conclusions about bias impact. So, for proceeding with the calibration of a GNSS/INS-assisted multi-unit LiDAR unit system, the test field and drive-run configurations are set up while taking these results of bias impact analysis into consideration.

Table 3.5.: Quantitative bias impact on vertical planes parallel to drive-run direction (YZ-plane)

RMSE (m)		Sign Board B1				Sign Board B3				Wall Patch W1			
		Same direction		Opposite directions		Same direction		Opposite directions		Same direction		Opposite directions	
		C1 (1, 3)	C3 (1, 5)	C2 (2, 3)	C4 (1, 6)	C1 (1, 3)	C3 (1, 5)	C2 (2, 3)	C4 (1, 6)	C1 (1, 3)	C3 (1, 5)	C2 (2, 3)	C4 (1, 6)
No Bias	Track A	0.0268	0.0268	0.0089	0.0268	0.0222	0.0222	0.0174	0.0222	0.0259	0.0259	0.0152	0.0259
	Track B	0.0133	0.0246	0.0133	0.0205	0.0084	0.0169	0.0084	0.0160	0.0158	0.0154	0.0158	0.0379
	Combined	0.0214	0.0288	0.0116	0.0231	0.0210	0.0247	0.0156	0.0202	0.0206	0.0176	0.0158	0.0351
$\delta\Delta X$	Track A	0.0268	0.0268	0.0089	0.0268	0.0222	0.0222	0.0174	0.0222	0.0258	0.0258	0.0152	0.0258
	Track B	0.0134	0.0242	0.0134	0.0207	0.0084	0.0163	0.0084	0.0164	0.0158	0.0153	0.0158	0.0381
	Combined	0.0214	0.0284	0.1827	0.1779	0.0209	0.0239	0.1821	0.1763	0.0206	0.0175	0.1451	0.1845
$\delta\Delta Y$	Track A	0.0267	0.0267	0.0088	0.0267	0.0227	0.0227	0.0182	0.0227	0.0248	0.0248	0.0152	0.0248
	Track B	0.0137	0.0217	0.0137	0.0237	0.0085	0.0091	0.0085	0.0224	0.0167	0.0148	0.0167	0.0426
	Combined	0.0218	0.0297	0.0173	0.0304	0.0208	0.0211	0.0156	0.0290	0.0204	0.0178	0.0178	0.0388
$\delta\Delta Z$	Track A	0.0271	0.0271	0.0089	0.0271	0.0225	0.0225	0.0176	0.0225	0.0254	0.0254	0.0151	0.0254
	Track B	0.0133	0.0240	0.0133	0.0214	0.0083	0.0226	0.0083	0.0219	0.0168	0.0158	0.0168	0.0377
	Combined	0.0216	0.0256	0.0116	0.0250	0.0212	0.0234	0.0156	0.0229	0.0208	0.0195	0.0166	0.0381
$\delta\Delta\omega$	Track A	0.0215	0.0215	0.0088	0.0215	0.0210	0.0210	0.0129	0.0210	0.0194	0.0194	0.0152	0.0194
	Track B	0.0126	0.0155	0.0126	0.0328	0.0085	0.0158	0.0085	0.0257	0.0126	0.0255	0.0126	0.0709
	Combined	0.0199	0.0210	0.0121	0.0325	0.0207	0.0246	0.0124	0.0266	0.0162	0.0248	0.0131	0.0620
$\delta\Delta\phi$	Track A	0.0078	0.0078	0.0157	0.0078	0.0100	0.0100	0.0146	0.0100	0.0300	0.0300	0.0408	0.0300
	Track B	0.0166	0.0828	0.0166	0.0644	0.0189	0.0596	0.0189	0.0528	0.0452	0.0624	0.0452	0.0918
	Combined	0.0179	0.0652	0.0571	0.0785	0.0239	0.0476	0.0533	0.0685	0.0399	0.0584	0.0532	0.0858
$\delta\Delta\kappa$	Track A	0.1704	0.1704	0.0911	0.1704	0.1617	0.1617	0.1548	0.1617	0.3099	0.3099	0.1978	0.3099
	Track B	0.1334	0.1837	0.1334	0.1869	0.0943	0.1837	0.0943	0.1843	0.3120	0.3109	0.3120	0.2969
	Combined	0.1519	0.1838	0.1460	0.1860	0.1300	0.1814	0.1573	0.1827	0.3124	0.3108	0.3088	0.3008

3.4 Summary

In this chapter, a thorough bias impact analysis was conducted for perfectly vertical as well as nearly vertical terrestrial mobile mapping systems utilizing spinning multi-beam laser scanners. The analytically driven conclusions were further validated by evaluating the results from an experimental setup. Based on this analysis, an optimal target primitive setup and drive-run configuration was devised for calibrating a multi-sensor LiDAR system, which in turn would ensure a sufficiently accurate calibration result.

Table 3.6.: Quantitative bias impact on vertical planes perpendicular to drive-run direction (XZ-plane)

RMSE (m)		Sign Board B0				Sign Board B2				Sign Board B4			
		Same direction		Opposite directions		Same direction		Opposite directions		Same direction		Opposite directions	
		C1 (1, 3)	C3 (1, 5)	C2 (2, 3)	C4 (1, 6)	C1 (1, 3)	C3 (1, 5)	C2 (2, 3)	C4 (1, 6)	C1 (1, 3)	C3 (1, 5)	C2 (2, 3)	C4 (1, 6)
No Bias	Track A	0.0097	0.0097	0.0132	0.0097	0.0122	0.0122	0.0129	0.0122	0.0118	0.0118	0.0161	0.0118
	Track B	0.0133	0.0076	0.0133	0.0134	0.0137	0.0150	0.0137	0.0134	0.0117	0.0144	0.0117	0.0064
	Combined	0.0151	0.0098	0.0187	0.0120	0.0143	0.0140	0.0155	0.0160	0.0127	0.0121	0.0169	0.0181
$\delta\Delta X$	Track A	0.0144	0.0144	0.0123	0.0144	0.0125	0.0125	0.0126	0.0125	0.0201	0.0201	0.0204	0.0201
	Track B	0.0136	0.0087	0.0136	0.0172	0.0149	0.0250	0.0149	0.0165	0.0115	0.0182	0.0115	0.0076
	Combined	0.0191	0.0140	0.0168	0.0158	0.0151	0.0170	0.0145	0.0150	0.0225	0.0211	0.0159	0.0191
$\delta\Delta Y$	Track A	0.0095	0.0095	0.0131	0.0095	0.0122	0.0122	0.0129	0.0122	0.0129	0.0129	0.0161	0.0129
	Track B	0.0133	0.0076	0.0133	0.0131	0.0137	0.0143	0.0137	0.0137	0.0117	0.0142	0.0117	0.0064
	Combined	0.0150	0.0096	0.1765	0.1557	0.0142	0.0138	0.1904	0.1588	0.0128	0.0133	0.1821	0.1134
$\delta\Delta Z$	Track A	0.0098	0.0098	0.0130	0.0098	0.0123	0.0123	0.0132	0.0123	0.0122	0.0122	0.0161	0.0122
	Track B	0.0134	0.0075	0.0134	0.0169	0.0138	0.0152	0.0139	0.0137	0.0114	0.0164	0.0114	0.0066
	Combined	0.0153	0.0099	0.0132	0.0133	0.0143	0.0137	0.0151	0.0134	0.0127	0.0128	0.0138	0.0128
$\delta\Delta\omega$	Track A	0.0168	0.0168	0.0229	0.0168	0.0123	0.0123	0.0141	0.0123	0.0132	0.0132	0.0166	0.0132
	Track B	0.0164	0.0142	0.0164	0.0210	0.0123	0.0183	0.0123	0.0122	0.0123	0.0151	0.0123	0.0106
	Combined	0.0195	0.0200	0.0640	0.0422	0.0139	0.0173	0.0703	0.0394	0.0134	0.0178	0.0630	0.0189
$\delta\Delta\phi$	Track A	0.0092	0.0092	0.0134	0.0092	0.0122	0.0122	0.0136	0.0122	0.0155	0.0155	0.0157	0.0155
	Track B	0.0129	0.0107	0.0129	0.0135	0.0143	0.0152	0.0143	0.0165	0.0118	0.0183	0.0118	0.0074
	Combined	0.0110	0.0160	0.0135	0.0388	0.0146	0.0279	0.0145	0.0463	0.0162	0.0217	0.0139	0.0484
$\delta\Delta\kappa$	Track A	0.0145	0.0145	0.0185	0.0145	0.0121	0.0121	0.0126	0.0121	0.0121	0.0121	0.0179	0.0121
	Track B	0.0189	0.0212	0.0189	0.0145	0.0116	0.0108	0.0116	0.0151	0.0124	0.0141	0.0124	0.0077
	Combined	0.0966	0.1618	0.1022	0.1649	0.0888	0.1835	0.0952	0.1842	0.0868	0.1242	0.0954	0.1312

Table 3.7.: Quantitative bias impact on horizontal planes (XY-plane)

RMSE (m)		Ground Patch G0				Ground Patch G1				Ground Patch G2			
		Same direction		Opposite directions		Same direction		Opposite directions		Same direction		Opposite directions	
		C1 (1, 3)	C3 (1, 5)	C2 (2, 3)	C4 (1, 6)	C1 (1, 3)	C3 (1, 5)	C2 (2, 3)	C4 (1, 6)	C1 (1, 3)	C3 (1, 5)	C2 (2, 3)	C4 (1, 6)
No Bias	Track A	0.0094	0.0094	0.0102	0.0094	0.0094	0.0094	0.0102	0.0094	0.0156	0.0156	0.0166	0.0156
	Track B	0.0116	0.0127	0.0116	0.0117	0.0116	0.0127	0.0116	0.0117	0.0160	0.0154	0.0160	0.0138
	Combined	0.0106	0.0125	0.0125	0.0131	0.0106	0.0125	0.0125	0.0131	0.0160	0.0154	0.0176	0.0164
$\delta\Delta X$	Track A	0.0094	0.0094	0.0101	0.0094	0.0094	0.0094	0.0101	0.0094	0.0153	0.0153	0.0170	0.0153
	Track B	0.0124	0.0164	0.0124	0.0125	0.0124	0.0164	0.0124	0.0125	0.0161	0.0175	0.0161	0.0161
	Combined	0.0109	0.0217	0.0120	0.0115	0.0109	0.0217	0.0120	0.0115	0.0160	0.0181	0.0194	0.0172
$\delta\Delta Y$	Track A	0.0089	0.0089	0.0101	0.0089	0.0089	0.0089	0.0101	0.0089	0.0153	0.0153	0.0167	0.0153
	Track B	0.0112	0.0144	0.0112	0.0135	0.0112	0.0144	0.0112	0.0135	0.0161	0.0157	0.0161	0.0141
	Combined	0.0102	0.0132	0.0123	0.0139	0.0102	0.0132	0.0123	0.0139	0.0160	0.0156	0.0194	0.0187
$\delta\Delta Z$	Track A	0.0093	0.0093	0.0102	0.0093	0.0093	0.0093	0.0102	0.0093	0.0155	0.0155	0.0166	0.0155
	Track B	0.0116	0.0125	0.0116	0.0118	0.0116	0.0125	0.0116	0.0118	0.0160	0.0153	0.0160	0.0139
	Combined	0.0106	0.0121	0.0125	0.0126	0.0106	0.0121	0.0125	0.0126	0.0160	0.0153	0.0177	0.0165
$\delta\Delta\omega$	Track A	0.2423	0.2423	0.2613	0.2423	0.2423	0.2423	0.2613	0.2423	0.0792	0.0792	0.1754	0.0792
	Track B	0.2889	0.3733	0.2889	0.2970	0.2889	0.3733	0.2889	0.2970	0.2229	0.1240	0.2229	0.1240
	Combined	0.2648	0.2883	0.2783	0.2632	0.2648	0.2883	0.2783	0.2632	0.2323	0.1177	0.3733	0.5391
$\delta\Delta\phi$	Track A	0.0153	0.0153	0.0146	0.0153	0.0153	0.0153	0.0146	0.0153	0.0353	0.0353	0.0227	0.0353
	Track B	0.0121	0.0134	0.0121	0.0156	0.0121	0.0134	0.0121	0.0156	0.0187	0.0312	0.0187	0.0386
	Combined	0.0815	0.2196	0.0519	0.0775	0.0815	0.2196	0.0519	0.0775	0.0548	0.1832	0.4916	0.3369
$\delta\Delta\kappa$	Track A	0.0107	0.0107	0.0115	0.0107	0.0107	0.0107	0.0115	0.0107	0.0156	0.0156	0.0159	0.0156
	Track B	0.0136	0.0297	0.0136	0.0480	0.0136	0.0297	0.0136	0.0480	0.0185	0.0304	0.0185	0.0368
	Combined	0.0198	0.0372	0.0143	0.0326	0.0198	0.0372	0.0143	0.0326	0.0230	0.0600	0.0953	0.1032

4. SIMULTANEOUS SYSTEM CALIBRATION OF A MULTI-LIDAR MULTI-CAMERA MOBILE MAPPING PLATFORM

In this chapter, we propose a strategy to calibrate the mounting parameters for a multi-sensor system consisting of multiple spinning multi-beam laser scanners and multiple cameras using points and geometric tie features (e.g., planar, and linear/cylindrical features). The conceptual basis for multi-sensor system calibration is to minimize the discrepancies among conjugate points, linear features, and/or planar features obtained from different sensors and/or drive-runs. Owing to the irregular distribution of LiDAR points, conjugate LiDAR point pairs cannot be used since there is no accurate point-to-point correspondence. However, the same limitation does not apply to imagery data, where a conjugate-point-pairing-based bundle adjustment can be adopted for calibration. This chapter starts by first discussing the conventional photogrammetric bundle adjustment and then, analyzing its equivalency to a newly proposed point-pairing-based bundle adjustment model. Apart from conjugate point pairings, conjugate linear/cylindrical and planar features, such as building facades, ground patches, light poles, and lane markers, are also used for multi-sensor calibration and these can be directly extracted from overlapping areas among the acquired data from different drive-runs. The representation scheme and semi-automatic feature extraction procedure used in this study for such features is also discussed in this chapter. Finally, an iterative multi-sensor system calibration with weight modification is proposed to derive the mounting parameters based on the minimization of discrepancy between 3D coordinates of conjugate points and that of the normal distance between conjugate features. Figure 4.1 shows a flowchart listing the steps involved in multi-sensor system calibration. Each of these steps is discussed in more detail in the forthcoming sections.

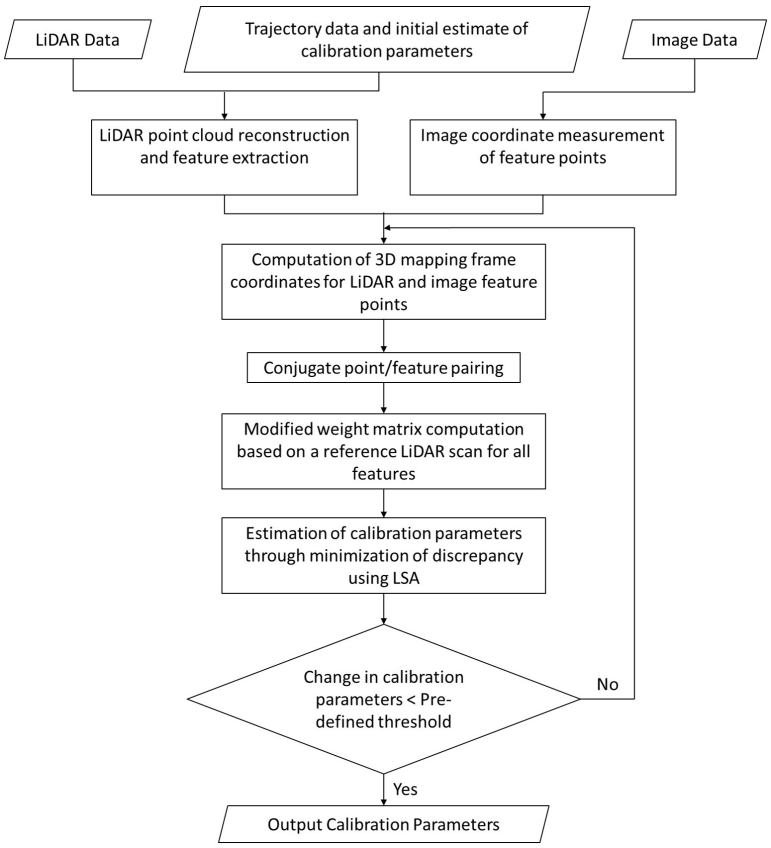

Fig. 4.1.: Flowchart of the steps involved in the proposed multi-sensor system calibration strategy

4.1 New Point-Pairing-Based Bundle Adjustment and Its Comparison to the Conventional Model

In this section, first, we briefly discuss the conventional photogrammetric bundle adjustment for single/multi-camera systems. Then, a new approach for bundle adjustment is proposed that uses point pairings between various image points. The new model is compared to the conventional bundle adjustment to examine the equivalency of the two models in terms of their parameter estimation ability.

In case of a conventional photogrammetric bundle adjustment for single/multi-camera systems, (2.4) is modified in order to eliminate the scaling factor. The terms in the equation are first rearranged to produce (4.1), which is further simplified to

result in (4.2a) and (4.2b), where the scaling factor has been eliminated by reducing three equations to two. In this model, the unknowns involved for an image point are its 3D mapping frame coordinates r_I^m (assuming that the intrinsic camera parameters, GNSS/INS position and orientation, and inter-sensor mounting parameters are available). So, if a point I is observed in m different images, then based on this model, there will be a total of $2m$ equations in three unknowns (r_I^m), thus resulting in a point definition redundancy of $(2m-3)$.

$$\begin{aligned} r_I^{C_j}(t) &= \frac{1}{\lambda(i, C_j, t)} \left[R_{C_r}^{C_j} \; R_b^{C_r} \; R_m^b(t) \; [r_I^m - r_b^m(t)] - R_{C_r}^{C_j} \; R_b^{C_r} \; r_{C_r}^b - R_{C_r}^{C_j} \; r_{C_j}^{C_r} \right] \\ &= \frac{1}{\lambda(i, C_j, t)} \begin{bmatrix} N_x \\ N_y \\ D \end{bmatrix} \end{aligned} \tag{4.1}$$

$$x_{ij} = x_{pj} - f_j \frac{N_x}{D} + \text{dist}_{x_{ij}} \tag{4.2a}$$

$$y_{ij} = y_{pj} - f_j \frac{N_y}{D} + \text{dist}_{y_{ij}} \tag{4.2b}$$

We propose a point-pairing-based bundle adjustment where (2.4) is retained in its original form, i.e., the scaling factors are not eliminated by reducing the three equations to two. Rather, the scaling factors are treated as unknowns to be estimated. This model aims to eliminate the 3D mapping frame coordinates of a point in order to allow for the estimation of scaling factors for the corresponding image points along with the calibration parameters. This is achieved by imposing an equality constraint on the 3D mapping frame coordinates computed for different image points representing the same object point by pairing them together. For instance, for a point I captured in two different images - one by camera C_j at time t_1 and another by camera C_k at time t_2 - the difference between the mapping coordinates computed from both images should be zero, (4.3). Here, the unknowns include the scaling factors for the two image points, $\lambda(i,\ C_j,\ t_1)$ and $\lambda(i',\ C_k,\ t_2)$. So, if a point I is observed in m different images, then based on this model, there will be a total of $(m-1)$

independent pairings between the images, where each pairing would result in three equations and each image point will have an associated scaling factor. Hence, there will be a total of $3(m-1)$ equations in m unknowns (scaling factors), thus resulting in a point definition redundancy of $(2m-3)$. This is the same as that obtained for the conventional model for bundle adjustment. The identical point definition redundancy, in turn, indicates the equivalency of the traditional model and the proposed point-pairing-based bundle adjustment. In this research, we use the latter model as it facilitates having a direct expression of the 3D mapping frame coordinates for the image points so that they can also be paired with the corresponding LiDAR points; as will be discussed in the forthcoming sections.

$$r_I^m(i, C_j, t_1) - r_I^m(i', C_k, t_2) = 0 \tag{4.3}$$

4.2 Representation Scheme and Feature Extraction

In this section, we discuss the representation scheme used in this study for linear and planar features in LiDAR data. Furthermore, we describe the semi-automatic feature extraction procedure used to derive various features from LiDAR data.

4.2.1 Linear Features

A linear feature appearing in an image or a LiDAR scan is represented by a sequence of pseudo-conjugate points lying along the feature. Here, the term "pseudo-conjugate points" refers to points that are not distinctly identifiable in different LiDAR scans/images but are known to belong to the same feature. The representation of linear features in images and LiDAR data is schematically illustrated in Figure 4.2(a) and depicted for a light pole in Figures 4.2(b) and 4.2(c). Note that points along a linear feature are labeled the same, thus denoting that the points are indistinct in nature, i.e., the only identification of a point is by the feature that it belongs

to and there is no assumption about having conjugate points among different images and LiDAR scans.

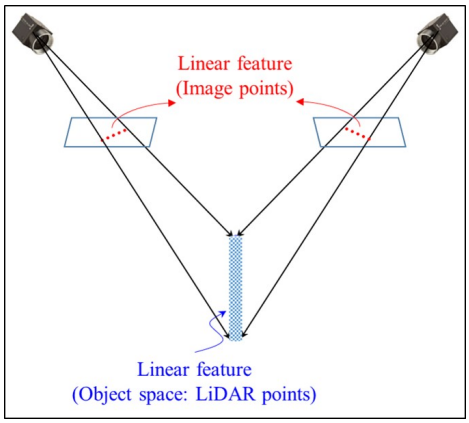

(a) Schematic illustration

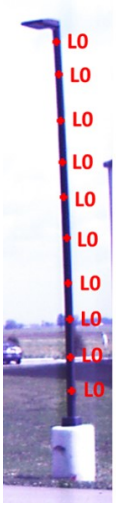

(b) Image points along a light pole

(c) LiDAR points along a light pole

Fig. 4.2.: Representation of linear features in imagery and LiDAR data

In outdoor calibration, various linear features can be extracted and used, such as flag poles, light poles, physical intersections of neighboring planar features, and so on. Features like flag poles or light poles are extracted from LiDAR data by specifying the two end points for each feature. A buffer radius (bf) is set to define a

cylinder around the linear feature of interest. Then, a line-fitting is done for the points lying within this cylindrical buffer, and finally, the points that lie within a normal distance threshold (nd_{th}) from the best-fitting line are extracted. On the contrary, points belonging to intersections of neighboring planar features are extracted by first, determining the best-fitting planes for each of the two planar surfaces. Then, their intersection line is determined and all the points lying withing a normal distance threshold (nd_{th}) from this line are extracted. In the case of imagery data, linear features are extracted by manually measuring image coordinates for pseudo-conjugate points along corresponding features.

4.2.2 Planar Features

A planar feature appearing in a LiDAR scan is represented by a sequence of pseudo-conjugate points lying along the feature. However, in the case of an image, a planar feature is represented by distinct points, such as the corners, along the feature, as shown schematically in Figure 4.3(a). For instance, the representation for a checkerboard target in imagery and LiDAR data (used in this study) is depicted in Figures 4.3(b) and 4.3(c), respectively. Note that LiDAR points belonging to each planar feature will have the same labels (which are specific to the feature) but the corresponding image points (here, corners of a board) will have distinct labels (specific to the corresponding object point). The justification for this deviation in the representation scheme followed for planar features from the one established for linear features is discussed in detail in Section 4.3.

In outdoor environment, several planar features available in the surroundings can be extracted and used for calibration. In this study, we use highly reflective boards, ground patches, wall patches, and other surfaces as planar features for calibration. The highly reflective sign boards can be easily identified from intensity data, as circled in Figure 4.4, where the points belonging to these boards exhibit higher intensity values than other LiDAR points. First, a predefined threshold (I_{th}) is set to extract

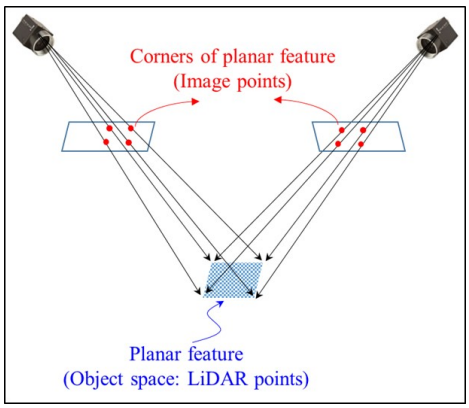

(a) Schematic illustration

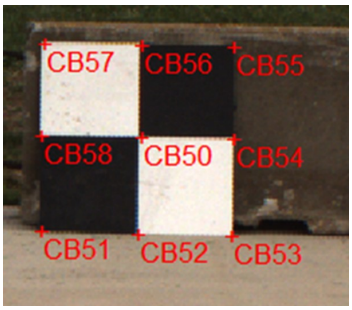

(b) Image points along a checkerboard target

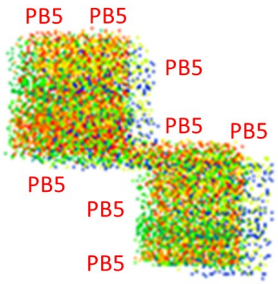

(c) LiDAR points along a checkerboard target

Fig. 4.3.: Representation of planar features in imagery and LiDAR data

high-intensity points. To avoid the extraction of high-intensity points belonging to objects other than these boards, an approximate preset region is set as seed points for each board. Then, for each of the tracks, a distance-based region growing technique is adopted to group the high-intensity points belonging to these boards starting from the preset seed point. The distance threshold (d_{th}) used for region growing is determined based on the accuracy of initial estimates of the mounting parameters. Finally, a plane-fitting is done for these points from each track, and the points lying within a normal distance threshold (nd_{th}) from the best-fitting plane are extracted. Other planar features, such as ground patches, wall patches, and other planar surfaces, are

extracted by defining two diagonally opposite corners. A bounding box is constructed around the planar feature of interest by adding a buffer value (bf) in X-, Y-, and Z-directions to the coordinates of diagonally opposite corners. Again, a plane-fitting is done for the points contained inside the box, and the ones lying within a normal distance threshold (nd_{th}) from the best-fitting plane are extracted. In the case of imagery data, the image coordinates of distinctly identifiable points along a planar feature (corners or center) are manually measured.

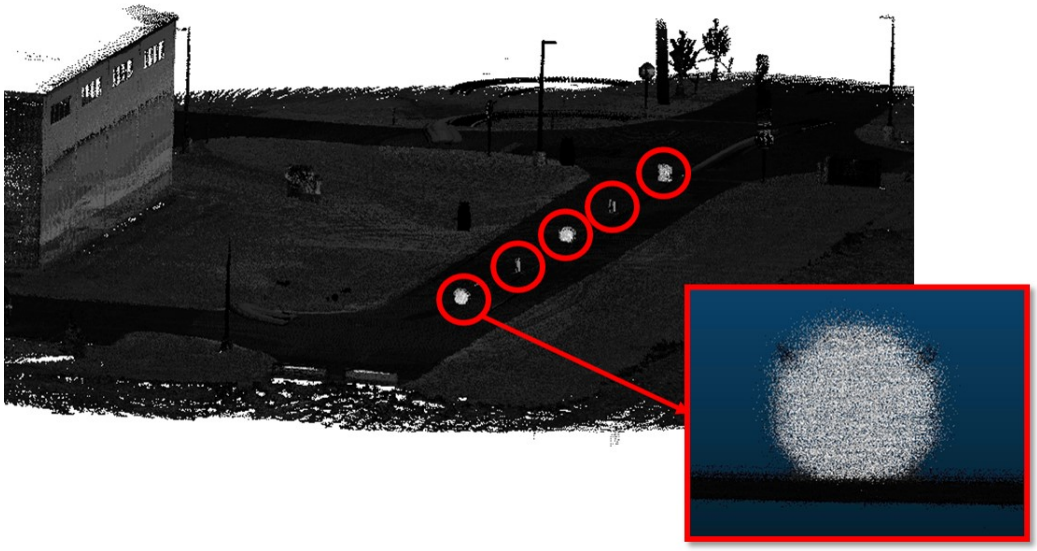

Fig. 4.4.: Intensity data of a point cloud obtained from a single drive-run

4.3 Development of an Optimal Pairing Scheme for Multi-sensor System Calibration

Now that the representation scheme has been established for the different types of features used for calibration, we proceed to analyze their contributions toward calibration. The mapping frame coordinates of a point I captured in a LiDAR scan and an image can be derived using (2.3) and (2.4), respectively. Consequently, the calibration objective function is to find the system parameters that minimize the

discrepancies between the 3D coordinates of a point derived from different drive-runs. In case of a multi-LiDAR multi-camera system, these discrepancies can arise from three types of pairings - LiDAR-to-LiDAR pairing (4.4), image-to-image pairing (4.5), and LiDAR-to-image pairing (4.6), where the term pairing refers to a point (say, I) observed in two LiDAR scans, two images, or one LiDAR scan and one image.

$$\text{LiDAR-to-LiDAR Pairing: } r_I^m(\text{Lu}_j, t_1) - r_I^m(\text{Lu}_k, t_2) = 0 \tag{4.4}$$

$$\text{Image-to-Image Pairing: } r_I^m(C_j, t_1) - r_I^m(C_k, t_2) = 0 \tag{4.5}$$

$$\text{LiDAR-to-Image Pairing: } r_I^m(\text{Lu}_j, t_1) - r_I^m(C_k, t_2) = 0 \tag{4.6}$$

Now, the contribution of each of the above-mentioned pairings toward calibration is analyzed for points, linear features, and planar features. One should note that each point pair serves two purposes – the first is the derivation of 3D mapping frame coordinates of the involved point and second is the estimation of system calibration parameters. So, in order to determine the contribution from a pairing toward system calibration, we compute the point definition redundancy, i.e., the redundancy for the derivation of the 3D mapping frame coordinates of LiDAR/image points, as a result of LiDAR-to-LiDAR, image-to-image, and LiDAR-to-image pairings. The point definition redundancy is chosen as a metric to deduce whether any type of pairing will have a contribution towards the estimation of system mounting parameters. If a pairing has a point definition redundancy greater than zero, then it indicates that apart from the contribution of the pairing towards the derivation of the involved 3D point coordinates, the same pairing will also be able to contribute towards the estimation of the system mounting parameters. One should note that in case of a LiDAR point, there are no additional unknowns involved in computing its 3D mapping frame coordinates apart from the system parameters. However, in case of an image point, there is a unique scaling factor associated with it, which is an additional unknown for computing its 3D mapping frame coordinates.

4.3.1 Point-based pairings

Let us consider a point I captured in n different LiDAR scans and m different images. Then, there can be a total of $(n-1)$ independent LiDAR-to-LiDAR pairings, $(m-1)$ independent image-to-image pairings, and one additional pairing between a LiDAR scan and an image for this point. Each point pairing will result in a random misclosure vector ($\vec{e}$), as given in (4.7).

$$r_I^m(\text{LiDAR scan/image 1}) - r_I^m(\text{LiDAR scan/image 2}) = \vec{e} \tag{4.7}$$

For a conjugate point pairing, the discrepancy ($\vec{e}$) is minimized along the X-, Y-, and Z-directions of the mapping frame, thus resulting in three equations for each point pair. So, a LiDAR-to-LiDAR point pairing will result in three equations with no additional unknowns, and hence, the point definition redundancy is 3, as shown in Figure 4.5(a). Now, an image-to-image point pairing would introduce a scaling factor corresponding to each image, as shown in Figure 4.5(c). As a result, there will be three equations and two unknowns, i.e., the point definition redundancy is 1. Similarly, a LiDAR-to-image point pairing, as shown in Figure 4.5(b), will give rise to three equations and one unknown (scaling factor corresponding to the image point), and thus, the point definition redundancy is 2. However, owing to the irregular distribution of LiDAR points, there is no accurate point-to-point correspondence between the LiDAR point clouds and images obtained from different drive-runs, thus ruling out the possibility of LiDAR-to-LiDAR and LiDAR-to-image conjugate point pairing.

4.3.2 Linear-feature-based pairings

As discussed before, a linear feature is represented by a sequence of pseudo-conjugate points along the feature. Each pseudo-conjugate point pairing will result in a random misclosure vector ($\vec{e}$) along with a non-random misclosure vector ($\vec{D}$), as shown in Figure 4.6(a) and expressed mathematically in (4.8).

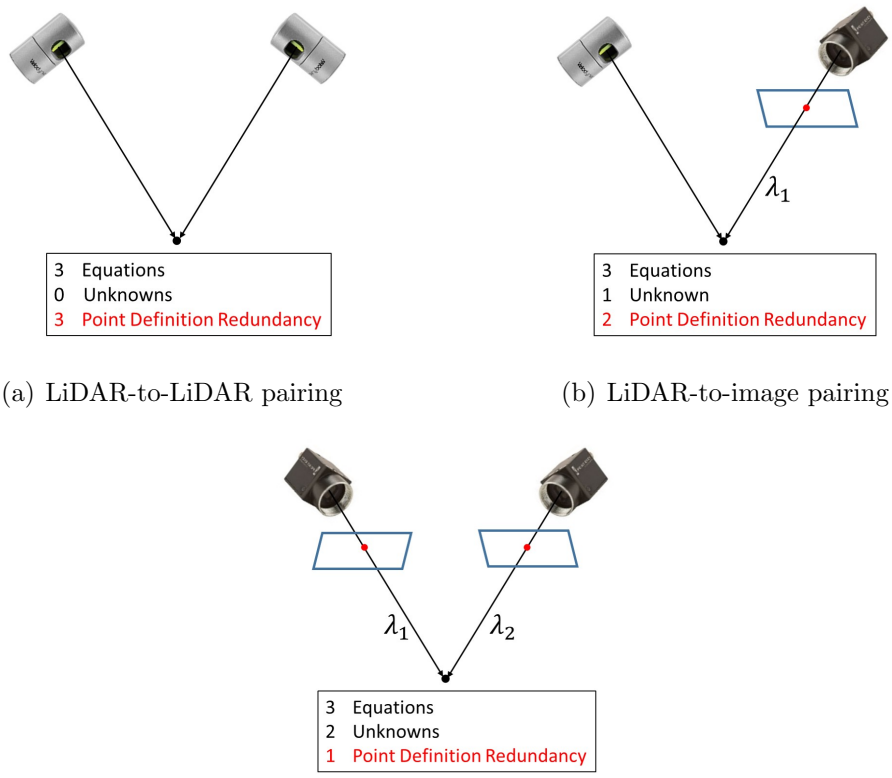

(a) LiDAR-to-LiDAR pairing

(b) LiDAR-to-image pairing

(c) Image-to-image pairing

Fig. 4.5.: Point definition redundancy for point-based pairings

$$r_I^m(\text{LiDAR scan/image 1}) - r_I^m(\text{LiDAR scan/image 2}) = \vec{D} + \vec{e} \tag{4.8}$$

In this case, the discrepancy of the resultant point pair should be minimized only along the two directions that are normal to the axial direction of the linear feature, thus resulting in two equations from each pseudo-conjugate point pair. This is achieved by applying a modified weight matrix to the point pair, which nullifies the component of their discrepancy along the axial direction of the linear feature. This modified weight matrix is derived according to the estimated direction of the linear feature using the points from a reference LiDAR scan encompassing this feature. The scan with the largest number of points belonging to a feature is set as the reference scan as it would result in the most reliable estimate of the feature direction. Note

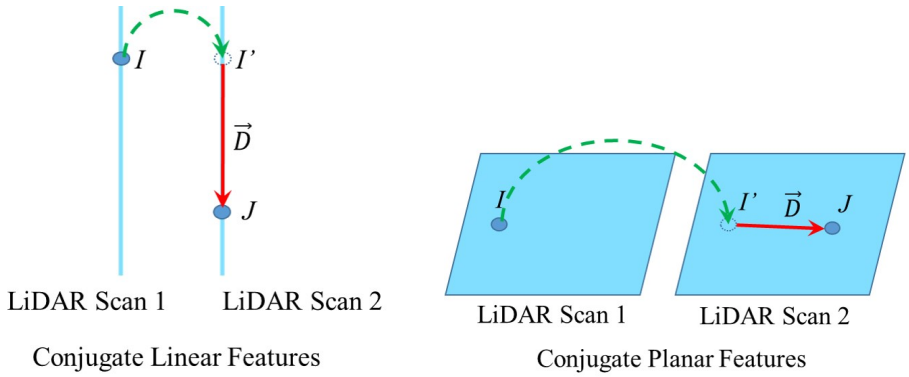

(a) Linear features (b) Planar features

Fig. 4.6.: Discrepancy vector between pseudo-conjugate points along corresponding features

that an image can never be used as a reference since each feature point in an image has a different unknown scaling factor and so, they cannot be used to derive a reliable feature direction in object space. Hence, all the images and LiDAR scans are paired to a reference LiDAR scan, i.e., there would be no image-to-image pairings in the case of linear features. The computation of the above-mentioned modified weight matrix will be discussed in more detail in Section 4.4.

In summary, if a linear feature is captured in n different LiDAR scans and m different images, then there will be a total of $(n-1)$ independent LiDAR-to-LiDAR pairings and m independent LiDAR-to-image pairings for each pseudo-conjugate point along the feature. A pseudo-conjugate LiDAR-to-LiDAR point pairing will give two equations and no unknowns, thus leading to a point definition redundancy of 2, as shown in Figure 4.7(a). Each pseudo-conjugate LiDAR-to-image point pairing will result in two equations and one unknown (scaling factor corresponding to the image point), i.e., the point definition redundancy is 1, as shown in Figure 4.7(b).

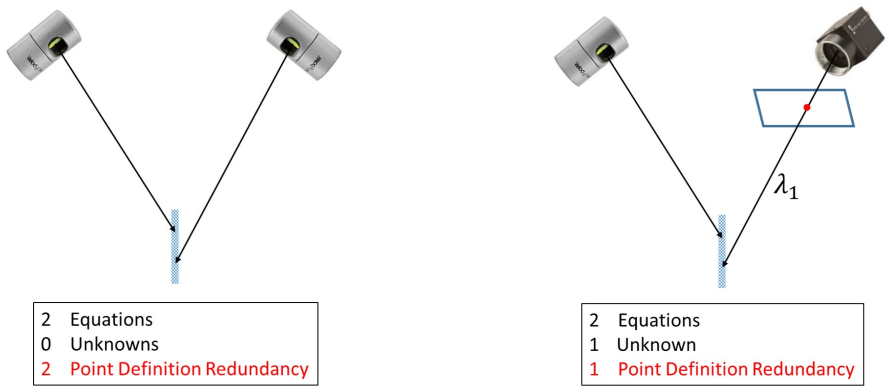

(a) LiDAR-to-LiDAR pairing (b) LiDAR-to-image pairing

Fig. 4.7.: Point definition redundancy for line-based pairings

4.3.3 Planar-feature-based pairings

A planar feature is represented by a sequence of pseudo-conjugate points along the feature. Again, each pseudo-conjugate point pairing will result in a random misclosure vector ($\vec{e}$) along with a non-random misclosure vector ($\vec{D}$), as shown in Figure 4.6(b) and stated before in (4.8). So, the discrepancy of the resultant point pair is minimized only along the direction normal to the planar surface, thus resulting in only one equation from each pseudo-conjugate point pair. Again, this is achieved by deriving a modified weight matrix using the normal direction of the planar surface based on the points from the corresponding reference LiDAR scan that encompass this feature (Section 4.4). This matrix would retain only the component of the discrepancy along the normal direction of the planar feature and nullify the other two. Similar to the discussion for linear features, an image cannot be used as reference for planar features as well. So, all the images and LiDAR scans will be paired to a reference LiDAR scan.

Let us consider a planar feature captured in n different LiDAR scans and m different images. Again, there will be a total of $(n-1)$ independent LiDAR-to-LiDAR pairings and m independent LiDAR-to-image pairings for each pseudo-conjugate point

along the feature. A pseudo-conjugate LiDAR-to-LiDAR point pairing will lead to one equation and no unknowns, which implies a point definition redundancy of 1, as shown in Figure 4.8(a). Each pseudo-conjugate LiDAR-to-image point pairing will result in one equation and one unknown (scaling factor corresponding to the image point), i.e., the point definition redundancy is 0, as shown in Figure 4.8(b). This implies that such pairings will not make a contribution toward the estimation of the system calibration parameters. This leads to the conclusion that pseudo-conjugate image points from a planar feature should not be used for calibration (as mentioned in Section 4.2). However, this model can be modified slightly by incorporating unique points belonging to a planar feature (such as the corners or center of a board) in different images. This would enable conjugate point pairings between different images for a planar feature. So, an image-to-image pairing for a point I belonging to a planar feature would result in three equations (and two unknowns) and a LiDAR-to-image pairing between one of the image points and a pseudo-conjugate LiDAR point will give an additional equation involving a scaling factor that has been already incorporated in the image-to-image point pairing. Hence, the point definition redundancy is increased to 2, as shown in Figure 4.8(c).

Based on this discussion, we can conclude that the following pairing scheme is optimal in order to conduct multi-LiDAR multi-camera system calibration:

1. Image-to-image conjugate point pairing,
2. LiDAR-to-LiDAR and LiDAR-to-image pairings of pseudo-conjugate points belonging to corresponding linear features,
3. LiDAR-to-LiDAR pairings of pseudo-conjugate points along corresponding planar features, and
4. LiDAR-to-image pairings of pseudo-conjugate points belonging to corresponding planar features (which have distinct points that can be identified in images) along with image-to-image conjugate point pairs for the same feature.

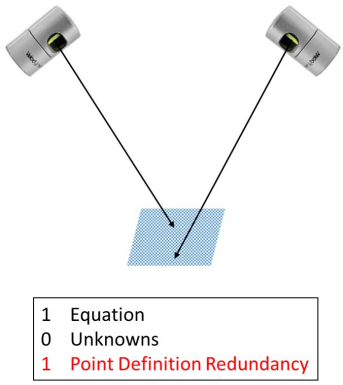

(a) LiDAR-to-LiDAR pairing

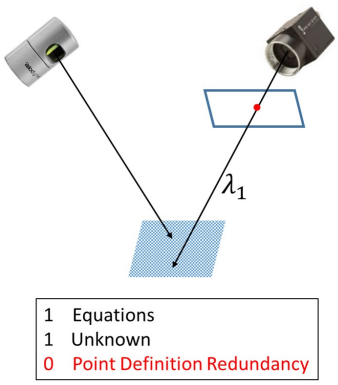

(b) LiDAR-to-image pairing

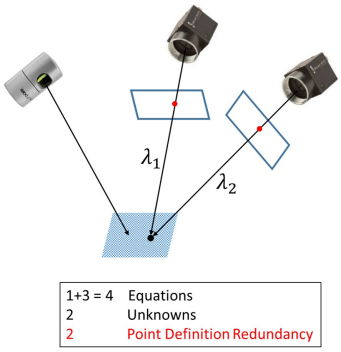

(c) LiDAR-to-image and image-to-image pairing

Fig. 4.8.: Point definition redundancy for plane-based pairings

4.4 Weight Modification for Pseudo-conjugate Point Pairings along Corresponding Features

In the proposed calibration method, conjugate features are extracted from the point clouds of different sensors and several drive-runs. The mounting parameters of each sensor are derived by minimizing the discrepancies among conjugate features (points/lines/planes) in overlapping drive-runs. Each pairing between conjugate features will result in a misclosure vector, which would be random ($\vec{e}$) in case of a conjugate point pair, as given before by (4.7). However, a pairing between pseudo-

conjugate points along corresponding planar or linear/cylindrical features would additionally introduce a non-random component ($\vec{D}$) in the misclosure vector, as given by (4.8). This component ($\vec{D}$) would lie along the planar surface or along the linear feature, respectively, as illustrated in Figure 4.6. Therefore, a modified weight matrix, P', is introduced to eliminate the non-random component of the misclosure vector, $\vec{D}$, from the LSA cost function, as given by (4.9) [32]. To derive this matrix, a local coordinate system (UVW) is established first. For linear features, the U-axis is aligned along the line and V- and W-axes are arbitrarily chosen to satisfy the orthogonality of the UVW triad. For the planar features, W-axis is aligned along the normal vector of the plane in question, and U- and V-axes are arbitrarily chosen along the planar feature. An illustration of the local coordinate systems for the two types of features is shown in Figure 4.9. Then, a rotation matrix, R_{XYZ}^{UVW}, relating the local and mapping coordinate systems is derived according to the components of the vectors, U, V, and W relative to the mapping frame. The weight matrix, P_{XYZ}, in the mapping coordinate system is transformed to a weight matrix, P_{UVW}, in the local coordinate system according to the law of error propagation ((4.10)). One should note that P_{XYZ} can be derived by applying the law of error propagation to the LSA model using the variance-covariance matrix derived for the point-pairings used for calibration. In this study, each point-pairing is weighed equally, i.e., P_{XYZ} is assumed to be identity matrix. The weight matrix, P_{UVW}, is modified by assigning a zero weight to the elements corresponding to the direction of $\vec{D}$. More specifically, the non-random component of the misclosure vector ($\vec{D}$) can be eliminated from the LSA minimization target function by setting a zero weight in the corresponding direction. The direction of ($\vec{D}$) for a linear feature is along the U-axis. Therefore, the modified weight matrix, P'_{UVW}, has zero weight in all the elements pertaining to the U-axis ((4.11)). Similarly, the direction of ($\vec{D}$) for a planar feature is along the U- and V-axes. So, all the elements pertaining to the U- and V-axes are assigned a zero weight ((4.12)). The modified weight matrix, P'_{XYZ}, in the mapping coordinate system is derived using (4.13). Finally, the obtained modified weight matrix, P'_{XYZ},

is applied to the condition in (4.8) to account for pseudo-conjugate points along the corresponding features within overlapping drive-runs. The resultant target function of LSA for calibration is to minimize the sum, S, which is given by (4.14).

$$P'\vec{D} = P' \begin{bmatrix} d_x \\ d_y \\ d_z \end{bmatrix} = 0 \tag{4.9}$$

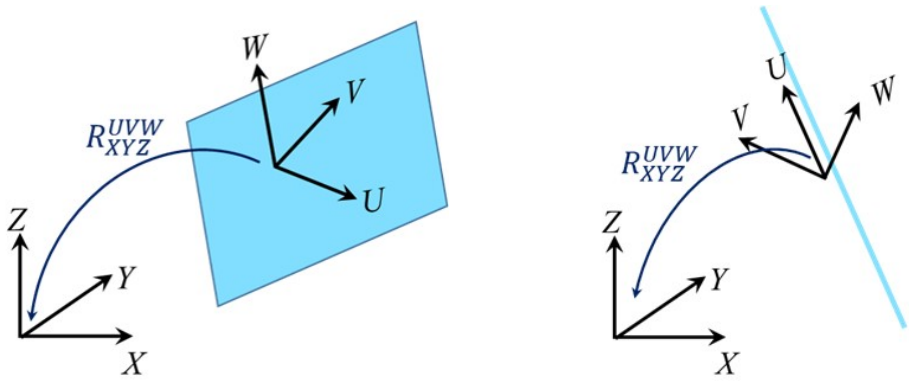

(a) Planar features (b) Linear features

Fig. 4.9.: Discrepancy vector between pseudo-conjugate points along corresponding features

$$P_{UVW} = R^{UVW}_{XYZ}\ P_{XYZ}\ R^{UVW^T}_{XYZ} = \begin{bmatrix} P_{UU} & P_{UV} & P_{UW} \\ P_{VU} & P_{VV} & P_{VW} \\ P_{WU} & P_{WV} & P_{WW} \end{bmatrix} \tag{4.10}$$

$$\text{Linear/Cylindrical Features: } P'_{UVW} = \begin{bmatrix} 0 & 0 & 0 \\ 0 & P_{VV} & P_{VW} \\ 0 & P_{WV} & P_{WW} \end{bmatrix} \tag{4.11}$$

$$\text{Planar Features: } P'_{UVW} = \begin{bmatrix} 0 & 0 & 0 \\ 0 & 0 & 0 \\ 0 & 0 & P_{WW} \end{bmatrix} \tag{4.12}$$

$$P'_{XYZ} = R_{XYZ}^{UVW^T}\ P'_{UVW}\ R_{XYZ}^{UVW} \tag{4.13}$$

$$S = \sum \left(\left(P' \left(\vec{D} + \vec{e} \right) \right)^T \left(P' \left(\vec{D} + \vec{e} \right) \right) \right) = \sum \left(\left(P' \vec{e} \right)^T \left(P' \vec{e} \right) \right) \tag{4.14}$$

4.4.1 Iterative Calibration Strategy

In this section, we summarize the proposed strategy to simultaneously estimate the mounting parameters of several spinning multi-beam laser scanners and cameras onboard a mobile platform using tie points and tie features (e.g., planar and linear features). After collecting data from several drive-runs, a LiDAR-based 3D point cloud relative to a global reference frame will be derived using the GNSS/INS-based position/orientation and initial estimates for the mounting parameters. Then, conjugate features are identified and extracted from the reconstructed point cloud. Similarly, images captured from different cameras and drive-runs are used to measure the image coordinates of the points belonging to these conjugate features. The 3D coordinates for the image points are computed using initial estimates of their scaling factors and camera mounting parameters along with the GNSS/INS position and orientation information.

The multi-LiDAR multi-camera system calibration is based on minimizing the discrepancies among conjugate points, linear features, and/or planar features obtained from different laser scanners, cameras, and/or drive-runs. An optimal configuration should aim to maximize the impact of biases in calibration parameters so as to ensure an accurate estimation of the bias. So, the configuration used in a calibration mission is one where there are sufficient target primitives to establish a control in all three directions (along drive-run, across drive-run, and vertical directions). Moreover, the drive-run configuration should include tracks in the same as well as opposite directions with different lateral separations between them. The target primitives and drive-runs

should be configured such that they adhere to the optimal configuration suggested according to the bias impact analysis conducted in Chapter 3.

When the initial estimate of the mounting parameters is inaccurate, the estimated modified weight matrix used for minimizing the discrepancies between pseudo-conjugate point pairings along corresponding features would be imprecise which would affect the accuracy of the derived mounting parameters. Hence, this research proposes an iterative calibration procedure. First, the discrepancy among extracted features is minimized to derive mounting parameters through the weight modification process. Then, the points along the extracted features are regenerated using the newly estimated mounting parameters and the discrepancy among conjugate features is minimized again using a newly defined modified weight matrix. The above steps are repeated until the change in the estimates of the mounting parameters is below a predefined threshold.

The parameters that need to be estimated using multi-sensor calibration are the scaling factors for all the points measured in different images ($\lambda(i, C_j, t)$), the lever-arm ($\Delta X,\ \Delta Y,\ \Delta Z$), and boresight angles ($\Delta\omega,\ \Delta\phi,\ \Delta\kappa$) for all the laser scanners and cameras. However, the vertical lever arm component ΔZ of the reference laser scanner is fixed during the calibration procedure as it cannot be estimated in the calibration procedure since any change in ΔZ will not introduce discrepancies among the different versions of the same feature captured from different laser scanners, cameras, and/or drive-runs. It would only result in a shift of the point cloud in the vertical direction as a whole. So, it is either manually measured or determined using vertical control (such as horizontal planar patches with known elevation). The proposed methodology can incorporate ground control points, which can be paired to the corresponding image points or pseudo-conjugate LiDAR points along the corresponding feature. Moreover, ground control features can also be paired with LiDAR or image points belonging to the corresponding feature. One should note that due to the generic nature of the proposed calibration model, it is also capable of simultaneously estimating the intrinsic parameters of all the cameras as well as the laser

scanners by using a sufficiently large number of conjugate point/feature pairs between different images/LiDAR scans captured from different drive-runs. Now, we proceed to the evaluation of the proposed calibration technique using experimental results for different mobile mapping systems.

4.5 Experimental Results for Calibration of Multi-sensor Mobile Mapping Systems

In this research, two different mobile mapping platforms - a car-mount system and a high clearance tractor (denoted henceforth as a PhenoRover-based system) - are used to collect LiDAR and photogrammetric data for 3D point cloud reconstruction, each of which is shown in Figures 4.10 and 4.11, respectively. The system specifications, dataset descriptions, and the calibration results for each of these systems are discussed in more detail in the forthcoming sections.

4.5.1 Car-mount Mobile Mapping System

The first dataset used to experimentally evaluate the proposed multi-sensor system calibration strategy is captured by a car-mount platform (as shown in Figure 4.10), which carries four LiDAR units (two Velodyne HDL32E sensors in the rear and one each of Velodyne HDL32E and Velodyne VLP16-Puck-Hi-Res in the front) and three cameras (two FLIR Grasshopper in the front and a FLIR Flea3 camera in the rear). The FLIR Grasshopper camera captures images at a resolution of 9.1 MP and the FLIR Flea3 camera has a resolution of 5 MP. These sensors are integrated with an Applanix POSLV 220 as the GNSS/INS unit used for direct georeferencing. The Velodyne HDL32E and VLP16-Puck-Hi-Res have typical range accuracies of 2 cm and 3 cm, respectively. For the Applanix POSLV 220, the post-processing accuracy in position can be less than 2 cm for X, Y and 5 cm for Z. The estimated accuracy for the roll/pitch and heading are 0.020° and 0.025°, respectively. These values were used to compute the expected achievable accuracy for the computed mapping

Fig. 4.10.: Car-mount MMS

frame coordinates using the LiDAR error propagation calculator developed by Habib et al. [18]. The calculator suggests that we should expect an accuracy of around 5 cm for the derived point cloud coordinates at a range of 30 m. The block diagram for this system, illustrating triggering signals, feedback signals, and communication wires/ports between sensors and power connections are shown in Figure 4.12. The setup for the car-mount system and the coordinate systems for the laser units, cameras, and the IMU body frame are shown in Figure 4.13. Here, it should be noted that the rotations between each front camera and the IMU body frame coordinate systems ($R^b_{C_L}$ and $R^b_{C_R}$) involve a secondary rotation of 90°, which would cause a gimbal lock problem. In order to avoid this gimbal lock problem, a virtual camera frame is introduced corresponding to each camera (C'_L and C'_R) that is approximately parallel to the IMU body frame. The introduction of virtual camera frame implies that the true rotational parameters are determined indirectly by estimating the cor-

Fig. 4.11.: PhenoRover-based Mobile Mapping System

rections to fixed approximate rotations. So, the mounting parameters relating the virtual reference camera frame (here, C'_L) to the IMU body frame ($r^b_{C'_L}$ and $R^b_{C'_L}$) and those relating the two virtual camera frames ($r^{C'_R}_{C'_L}$ and $R^{C'_R}_{C'_L}$) are estimated during calibration. On the other hand, the virtual camera frame is related to the actual one through fixed rotations ($R^{C_L}_{C'_L}$ and $R^{C_R}_{C'_R}$).

The target primitives and drive-runs for this experiment are configured in accordance with the optimal configuration derived based on the bias impact analysis conducted in Chapter 3. Five specially designed highly reflective boards are installed, perpendicular to each other, in a sufficiently spacious area to drive around them. The distance between adjacent sign boards was approximately 10 m along the driving direction. We ensure that the separation between target primitives during calibration is such that none of the target primitives are highly occluded by the others with respect to the laser scanner. Six highly reflective checkerboards are placed on the ground to

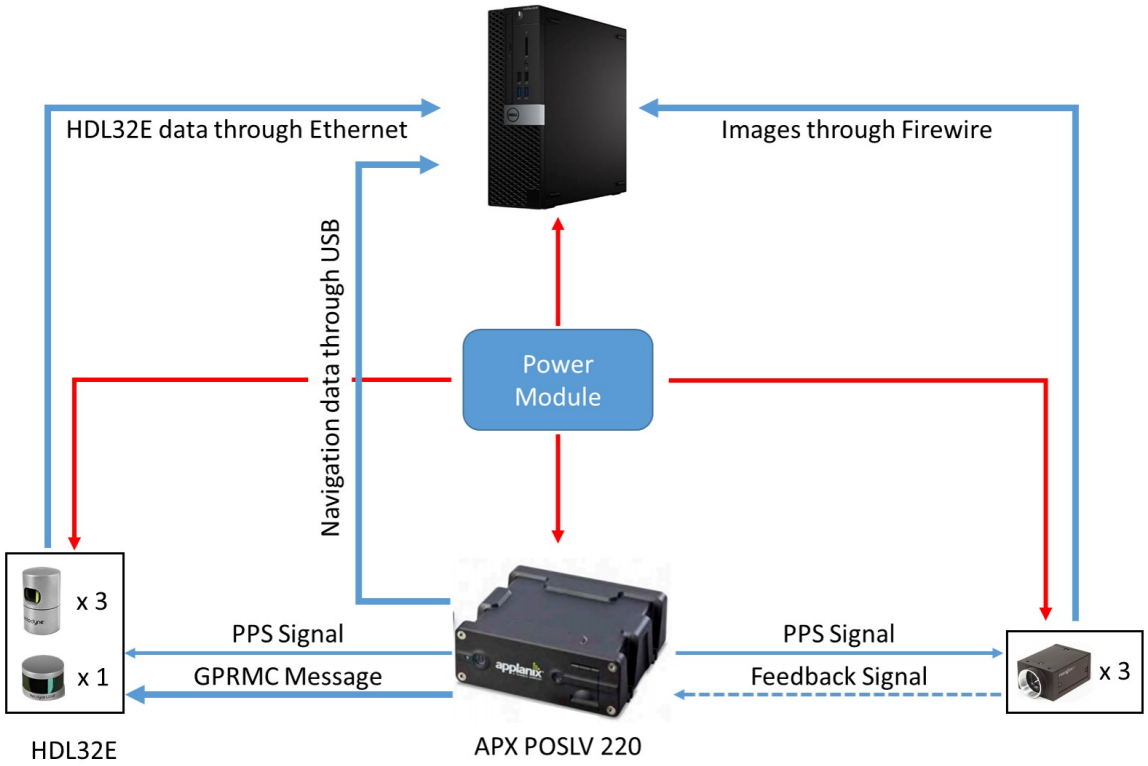

Fig. 4.12.: Integration scheme for the car-mount MMS

be used as horizontal planar features along with four ground patches. Four light poles and eight lane markers are used as linear features for calibration. Five hut-shaped targets are also deployed, with their ridges oriented perpendicular to each other. The two surfaces corresponding to each of these huts are used as planar features for calibration, and their ridges are used as conjugate linear features. One should note that the two planar features of hut-shaped targets are indeed not independent of their derived linear feature. However, since the aim of this research is to demonstrate the accuracy of the proposed calibration strategy, the correlation between these features is ignored and the planar as well as linear features of the hut-shaped targets can be used for calibration with their RMSEs indicating the quality of calibration. In this experiment, eight drive-runs having a length of approximately 60 m each, with different directions and lateral distance between them, were made around the calibration

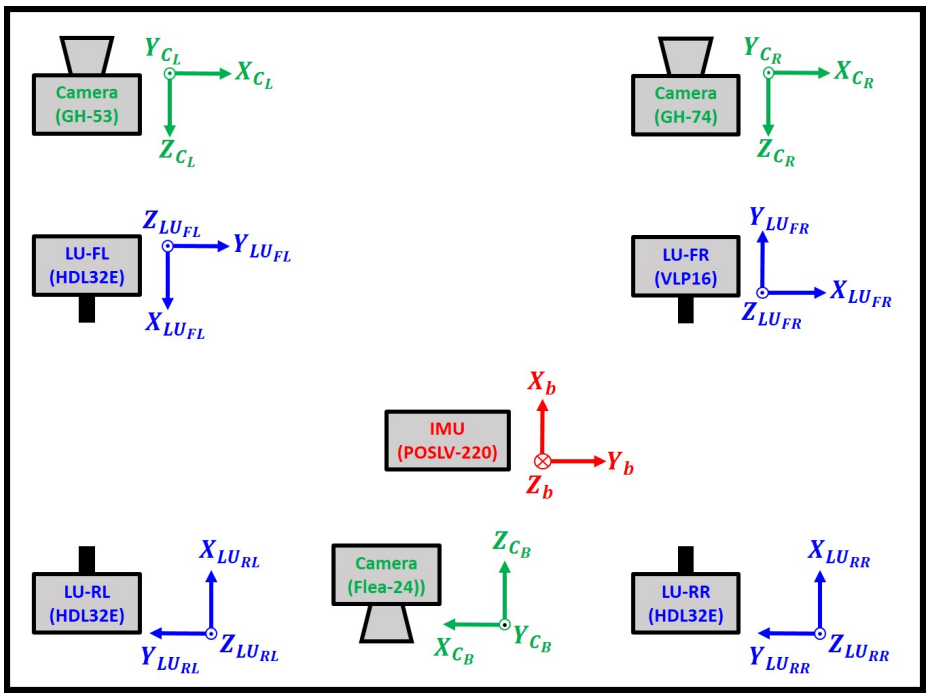

Fig. 4.13.: Coordinate systems for the car-mount MMS

primitives at an approximate speed of 4 miles/h. The cameras were set to capture images at an interval of 1 s. With eight drive-runs and four laser units, there will be a total of 32 versions for each of the features used for the calibration procedure. A total of 110 images from the three cameras were used to measure the image coordinates for the different calibration primitives. The coordinate measurements from each image are paired to a reference image in case of conjugate points or the reference version from LiDAR (i.e., the one consisting of most points along that feature) in the case of pseudo-conjugate points along a feature. Figure 4.14 shows the calibration test field and Figure 4.15 shows the configuration of drive-runs and target primitives, where PB denotes highly reflective planar boards, PV denotes the planar hut surfaces, PG denotes ground patches, L denotes light poles, LM denotes lane markers, and LH denotes linear hut ridges. For the car-mount, one of the laser scanners (here, rear-right HDL32E sensor) is taken as reference and the others are considered slave units. Similarly, one of the cameras (here, front-left Grasshopper camera) is set as reference

and the other two cameras are treated as slaves. The proposed calibration procedure is applied to obtain the mounting parameters for the four laser scanners and the three cameras simultaneously, using the features extracted from LiDAR point clouds and the distortion-free image coordinates.

Fig. 4.14.: Calibration test field for the car-mount MMS

A qualitative evaluation of the calibration results is done in two different ways:

1. checking the alignment in object space by computing the 3D mapping frame coordinates for all the LiDAR and image points using the GNSS/INS position and orientation information, estimated mounting parameters for the sensors, and estimated scaling factors for the image points; and

2. checking the alignment in image space by evaluating the pixel coordinates for all the LiDAR and image points based on their 3D mapping frame coordinates after calibration.

The initial approximations (derived from manual measurements) and the final results (along with their standard deviations) of all the mounting parameters are listed in Table 4.1, where the parameters fixed during calibration are highlighted in red. As

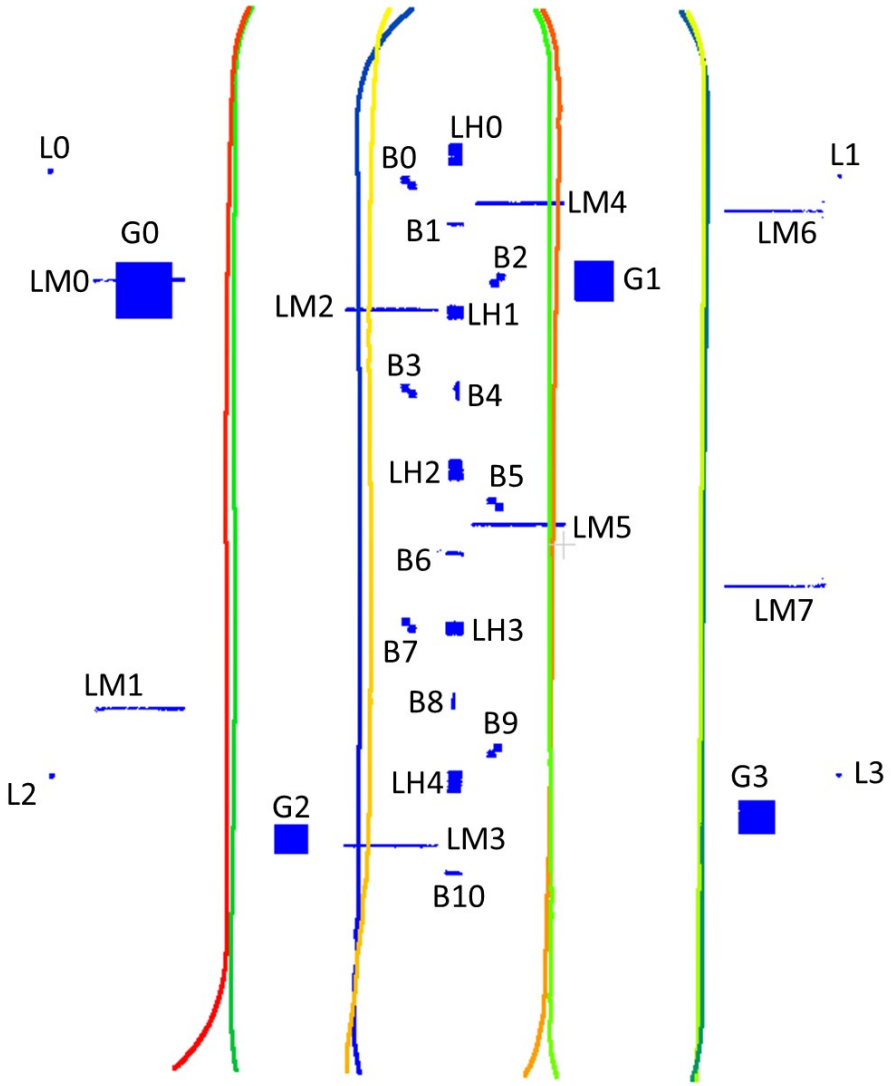

Fig. 4.15.: Configuration of drive-runs and calibration primitives for the car-mount MMS

a result of calibration, one should expect the estimated true sensor mounting parameters to be close to the initial approximations derived from manual measurements. We also report the square root of the *a posteriori* variance factor, denoted by $\hat{\sigma_0}$, which represents the average compatibility between all the conjugate and pseudo-conjugate point pairings. For the car-mount MMS, we obtained $\hat{\sigma_0} = 1.79$ cm after calibration. One should note that according to the accuracies of the hardware involved, the

expected accuracy of 3D point positioning is 3 cm. Using this information, we simulated a set of points belonging to a planar surface and introduced a random normal noise of 3 cm. On conducting a LSA-based planar fitting for the simulated dataset, it indicates the accuracy of feature-fitting to be about 3 cm. The value of $\hat{\sigma_0} = 1.79$ cm obtained from the experimental results indicates that the calibration achieves a better accuracy than the expected accuracy of around 3 cm according to the accuracies of the hardware involved. Figure 4.16 shows the LiDAR and image points (in blue and red, respectively) for the targets in the object space after calibration. From that figure, one can see that the corners of the highly reflective boards measured in different images align well with the high intensity LiDAR points. Similarly, the image points along the hut ridge are aligned in 3D with the corresponding LiDAR points. Figure 4.17 shows the alignment of LiDAR and image-based object points in image space by assigning blue color to the pixels corresponding to the object points derived from image measurements and the estimated calibration parameters. For quantitative evaluation, first, the object points derived from LiDAR unit and camera are considered together for computing the RMSE of normal distance for all the features. The RMSE of normal distance of LiDAR and image-based object points from best-fitting plane/line for extracted features before and after calibration for combined sensors are listed in Table 4.2. Here, the RMSE of features before calibration is computed using the 3D points reconstructed using the initial estimates of sensor mounting parameters listed in Table 4.1. Similarly, the RMSE after calibration is computed using the 3D points reconstructed using the final mounting parameters estimated from the proposed system calibration strategy, as listed in Table 4.1. The points used to evaluate the RMSE are actually the ones that were used to determine the mounting parameters. So, these RMSE values computed for the fitting residuals for all the features indicate the internal accuracy of calibration. Note that the proposed calibration approach is dependent on the extracted features, so it is imperative to evaluate the effect of feature extraction accuracy on the calibration results. The final RMSE of a feature obtained after calibration would reflect the feature extraction accuracy along

with the calibration accuracy. If the accuracy of feature extraction is low (i.e., the final RMSE is high), then the reliability of calibration results would decrease and it would be recommended to conduct a more accurate extraction of the feature and recalibrate the system. Also, the buffer used for extraction of various features is set according to the accuracy of initial estimates of calibration parameters.

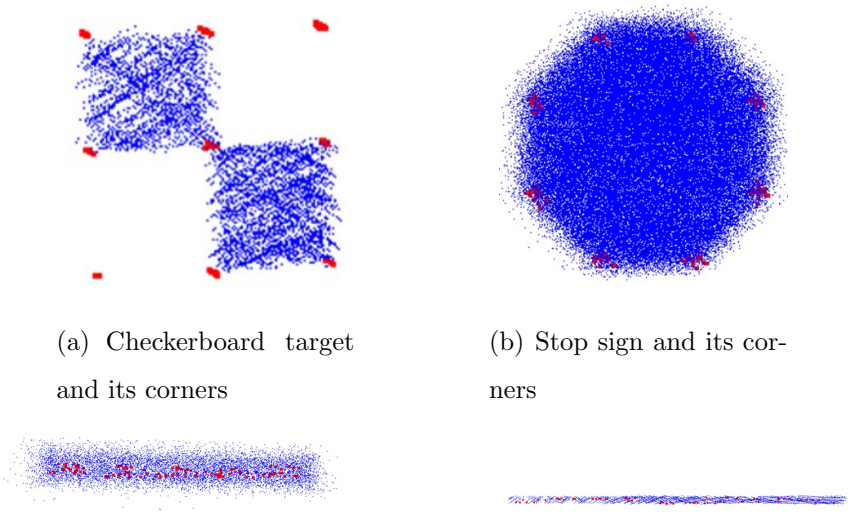

(a) Checkerboard target and its corners

(b) Stop sign and its corners

(c) Ridge of hut-shaped target

(d) Lane marker

Fig. 4.16.: Qualitative evaluation of 3D alignment between LiDAR (blue) and image-based object points (red) after calibration of car-mount MMS

4.5.2 PhenoRover-based Mobile Mapping System

The mobile mapping system onboard the PhenoRover consists of two Velodyne HDL32E laser scanners and two FLIR Grasshopper cameras, which are directly geo-referenced by an Applanix POSLV 125 unit. Both cameras capture images at a rate of 1 frame per second, thus leading to a stereo pair of images every second. For the POSLV 125, the postprocessing accuracy in position can be 2-5 cm and the estimated accuracy for the roll/pitch and heading can be 0.025° and 0.060°, respectively. These values were used to evaluate the expected accuracy of the derived mapping frame

Table 4.1.: Mounting parameters before and after calibration of the car-mount MMS

Reference Unit: HDL32E (Rear-Right) LiDAR Unit Mounting Parameters $\left(r^{b}_{\mathbf{Lu_{RR}}},\ R^{b}_{\mathbf{Lu_{RR}}}\right)$						
	ΔX (m)	ΔY (m)	ΔZ (m)	$\Delta\omega$ (°)	$\Delta\phi$ (°)	$\Delta\kappa$ (°)
Initial	-1.10	0.65	-0.44	180	-15	0
Final	-1.0998	0.6551	-0.44	180.2602	-16.7813	-0.2114
Standard Deviation	0.0044	0.0047	Fixed	0.0136	0.0122	0.0116
HDL32E (Rear-Left) LiDAR Unit Mounting Parameters $\left(r^{\mathbf{Lu_{RR}}}_{\mathbf{Lu_{RL}}},\ R^{\mathbf{Lu_{RR}}}_{\mathbf{Lu_{RL}}}\right)$						
	ΔX (m)	ΔY (m)	ΔZ (m)	$\Delta\omega$ (°)	$\Delta\phi$ (°)	$\Delta\kappa$ (°)
Initial	0	1.10	0	0	0	0
Final	-0.0011	1.1012	0.0070	-0.1890	-1.9851	-0.1349
Standard Deviation	0.0055	0.0057	0.0047	0.0132	0.0116	0.0124
HDL32E (Front-Left) LiDAR Unit Mounting Parameters $\left(r^{\mathbf{Lu_{RR}}}_{\mathbf{Lu_{FL}}},\ R^{\mathbf{Lu_{RR}}}_{\mathbf{Lu_{FL}}}\right)$						
	ΔX (m)	ΔY (m)	ΔZ (m)	$\Delta\omega$ (°)	$\Delta\phi$ (°)	$\Delta\kappa$ (°)
Initial	2.30	0.95	-0.65	0	20	180
Final	2.2929	0.9336	-0.6825	-0.4408	23.8006	-178.7085
Standard Deviation	0.0056	0.0057	0.0054	0.0139	0.0141	0.0123
VLP16 (Front-Right) LiDAR Unit Mounting Parameters $\left(r^{\mathbf{Lu_{RR}}}_{\mathbf{Lu_{FR}}},\ R^{\mathbf{Lu_{RR}}}_{\mathbf{Lu_{FR}}}\right)$						
	ΔX (m)	ΔY (m)	ΔZ (m)	$\Delta\omega$ (°)	$\Delta\phi$ (°)	$\Delta\kappa$ (°)
Initial	2.30	0.20	-0.75	0	25	-90
Final	2.2610	0.2236	-0.7680	-0.3834	27.6216	-89.9047
Standard Deviation	0.0072	0.0075	0.0090	0.0168	0.0218	0.0151
Reference Camera: Grasshopper (Front-Left) Camera Mounting Parameters $\left(r^{b}_{C'_L},\ R^{b}_{C'_L}\right)$						
	ΔX (m)	ΔY (m)	ΔZ (m)	$\Delta\omega$ (°)	$\Delta\phi$ (°)	$\Delta\kappa$ (°)
Initial	1.16	-0.46	-0.29	0	0	0
Final	1.1205	-0.4561	-0.3886	0.5398	-0.9069	1.9003
Standard Deviation	0.0425	0.0402	0.0452	0.0939	0.0988	0.0697
Grasshopper (Front-Right) Camera Mounting Parameters $\left(r^{C_L}_{C_R},\ R^{C_L}_{C_R}\right)$						
	ΔX (m)	ΔY (m)	ΔZ (m)	$\Delta\omega$ (°)	$\Delta\phi$ (°)	$\Delta\kappa$ (°)
Initial	1.1009	0.0144	-0.0380	-0.5332	3.7838	0.6363
Final	1.1099	0.0198	-0.0292	-0.5465	3.7782	0.5777
Standard Deviation	0.0450	0.0445	0.0486	0.1012	0.1047	0.0733
Flea3 (Back) Camera Mounting Parameters $\left(r^{C_L}_{C_B},\ R^{C_L}_{C_B}\right)$						
	ΔX (m)	ΔY (m)	ΔZ (m)	$\Delta\omega$ (°)	$\Delta\phi$ (°)	$\Delta\kappa$ (°)
Initial	0.95	0	2.00	90	0	90
Final	0.9582	-0.0262	2.0328	98.2048	2.5724	98.5418
Standard Deviation	0.0479	0.0416	0.0469	0.0972	0.0911	0.0646

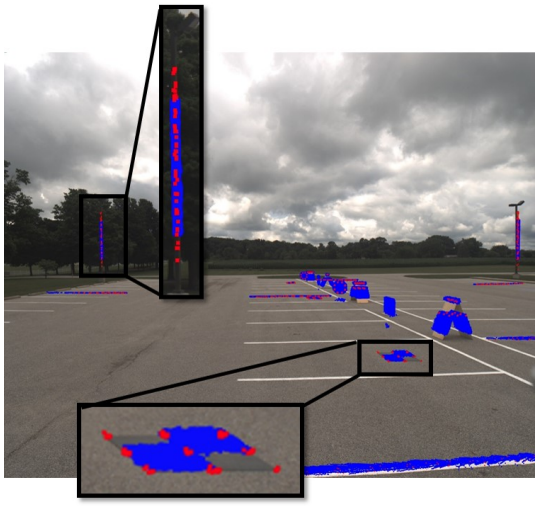

(a) Left camera image

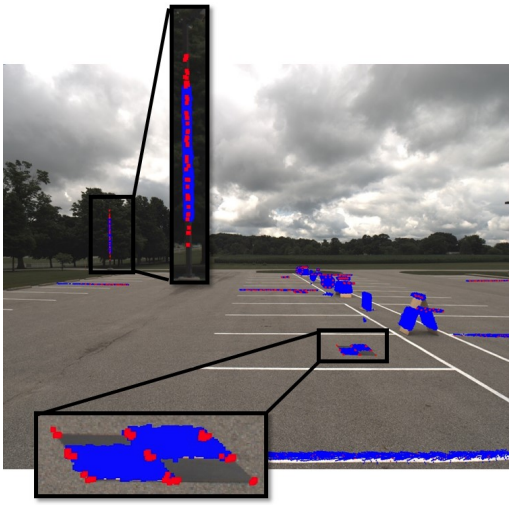

(b) Right camera image

Fig. 4.17.: Car-mount MMS: Backprojection of LiDAR (blue) and image-based object points (red) onto stereo-pair images

coordinates using the LiDAR error propagation calculator developed by Habib et al. [18]. The results from the error propagation calculator indicates that we should expect an accuracy of around 5 cm at a range of 30 m. The setup for the PhenoRover-based MMS and the coordinate systems for the laser units, cameras, and the IMU body frame are shown in Figures 4.11 and 4.18, respectively. Here, it should be noted that

Table 4.2.: RMSE of plane/line-fitting before and after calibration of the car-mount MMS

Feature ID	No. of LiDAR Points	No. of Image Points	RMSE (m)	
			Before Calibration	After Calibration
Reflective Boards				
PB0	6,816	56	0.018	0.021
PB1	117,351	60	0.021	0.021
PB2	5,507	93	0.010	0.014
PB3	5,258	83	0.015	0.018
PB4	156,237	-	0.022	0.022
PB5	4,822	72	0.008	0.008
PB6	123,261	156	0.023	0.022
PB7	5,338	74	0.020	0.023
PB8	135,046	-	0.020	0.020
PB9	4,150	65	0.013	0.009
PB10	103,737	81	0.020	0.019
Ground Patches				
PG0	597,927	-	0.020	0.015
PG1	547,993	-	0.022	0.022
PG2	238,791	-	0.020	0.019
PG3	336,907	-	0.025	0.021
Hut Surfaces (PV)				
PV0	94,263	-	0.018	0.019
PV1	96,511	-	0.018	0.020
PV2	92,944	-	0.017	0.017
PV3	93,362	-	0.020	0.021
PV4	93,095	-	0.020	0.021
PV5	87,464	-	0.019	0.019
PV6	95,575	-	0.019	0.019
PV7	102,781	-	0.019	0.019
PV8	83,271	-	0.020	0.020
PV9	85,401	-	0.019	0.020

Feature ID	No. of LiDAR Points	No. of Image Points	RMSE (m)	
			Before Calibration	After Calibration
Light Poles (L) and Hut Ridges (LH)				
L0	64,836	138	0.354	0.022
L1	39,463	144	0.167	0.019
L2	62,511	118	0.207	0.023
L3	42,435	56	0.423	0.021
LH0	6,969	50	0.044	0.014
LH1	7,410	18	0.047	0.015
LH2	9,869	105	0.122	0.033
LH3	8,033	10	0.022	0.014
LH4	9,825	74	0.376	0.014
Lane Markers				
LM0	1,131	48	0.164	0.016
LM1	1,562	57	0.310	0.016
LM2	7,618	93	0.132	0.014
LM3	5,960	67	0.106	0.012
LM4	8,082	56	0.113	0.015
LM5	5,674	76	0.095	0.015
LM6	3,128	66	0.165	0.020
LM7	3,177	50	0.184	0.018

the rotations between each laser unit and the IMU body frame coordinate systems ($R^b_{\mathrm{Lu}_L}$ and $R^b_{\mathrm{Lu}_R}$) involve a secondary rotation of 90°, which would cause a gimbal lock problem. In order to avoid this gimbal lock problem, a virtual LiDAR unit frame is introduced corresponding to each laser unit (Lu'_L and Lu'_R) that is approximately parallel to the IMU body frame. The introduction of virtual frame implies that the true rotational parameters are determined indirectly by estimating the corrections to fixed approximate rotations. So, the mounting parameters relating the virtual reference LiDAR unit frame (here, Lu'_L) to the IMU body frame ($r^b_{\mathrm{Lu}'_L}$ and $R^b_{\mathrm{Lu}'_L}$) and those relating the two virtual LiDAR unit frames ($r^{\mathrm{Lu}'_R}_{\mathrm{Lu}'_L}$ and $R^{\mathrm{Lu}'_R}_{\mathrm{Lu}'_L}$) are estimated

during calibration. On the other hand, the virtual LiDAR unit frame is related to the actual one through fixed rotations ($R^{\mathrm{Lu}_L}_{\mathrm{Lu}'_L}$ and $R^{\mathrm{Lu}_R}_{\mathrm{Lu}'_R}$).

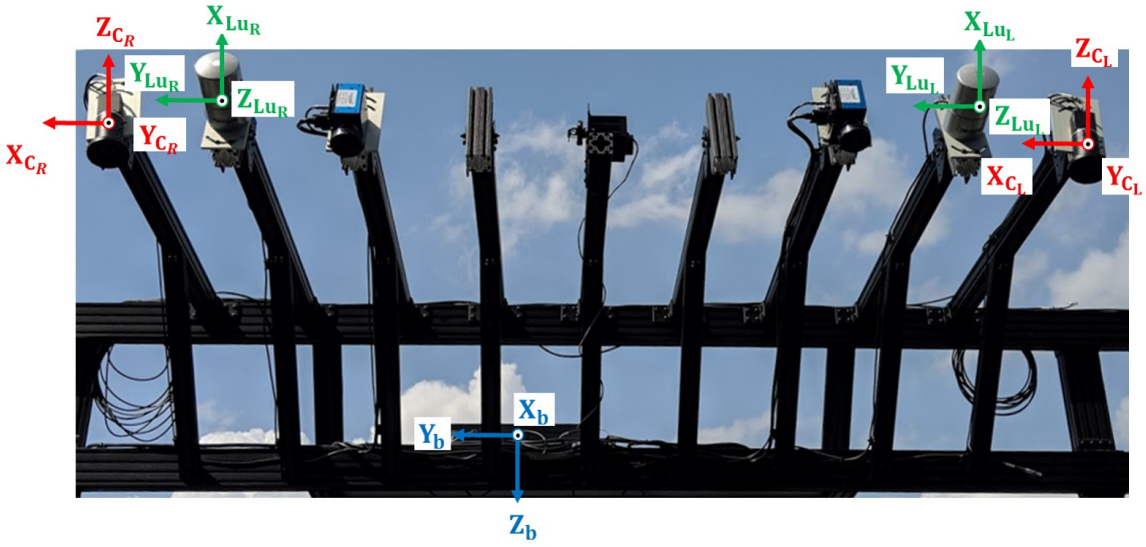

Fig. 4.18.: Coordinate Systems for PhenoRover-based MMS

The setup of calibration primitives is similar to the one used for the car-mount system. In this experiment, ten drive-runs, with different directions and lateral distances between them, were made around the calibration primitives at an approximate speed of 1.5 miles/h. A total of 126 images from both cameras were used to measure the image coordinates for the different calibration targets. Figure 4.19 shows the calibration test field, and Figure 4.20 shows the configuration of drive-runs and boards, where PB denotes highly reflective planar boards, PG denotes ground patches, L denotes light poles, and LH denotes linear hut ridges. The proposed multi-sensor calibration procedure is applied to obtain the mounting parameters for the laser units and cameras simultaneously.

The initial approximations and the final results (along with their standard deviations) of all the mounting parameters are listed in Table 4.3, where the parameters fixed during calibration are highlighted in red. The initial estimates of the mounting parameters relating the reference and slave cameras are set to the values from indoor

Fig. 4.19.: Calibration test field for the PhenoRover-based MMS

stereo-camera calibration and it should be noted that the parameters obtained from the proposed calibration strategy closely match the results from indoor calibration. The square root of the *a posteriori* variance factor ($\hat{\sigma_0}$) after calibration is 1.75 cm in this case. This is better than the expected accuracy (indicated by conducting a feature-fitting on simulated points with the same noise level) of around 5 cm according to the accuracies of the hardware involved. Figures 4.21 and 4.22 depict the qualitative evaluation of the calibration by showing the alignment of LiDAR and image-based object points belonging to different features in the mapping space (3D) and image space (2D), respectively. The RMSE of normal distance of LiDAR and image-based object points from best-fitting plane/line for extracted features before and after calibration for combined sensors are listed in Table 4.4, which indicate a significant improvement in the alignment of the features. Here, the RMSE of features before calibration is computed using the 3D points reconstructed using the initial estimates of sensor mounting parameters listed in Table 4.3. Similarly, the RMSE after calibration is computed using the 3D points reconstructed using the final mounting parameters estimated from the proposed system calibration strategy, as listed in Table 4.3. One should note that there are no image points for some linear features (such as light poles) since the cameras are both looking downward, and hence, these features are not captured in any of the images.

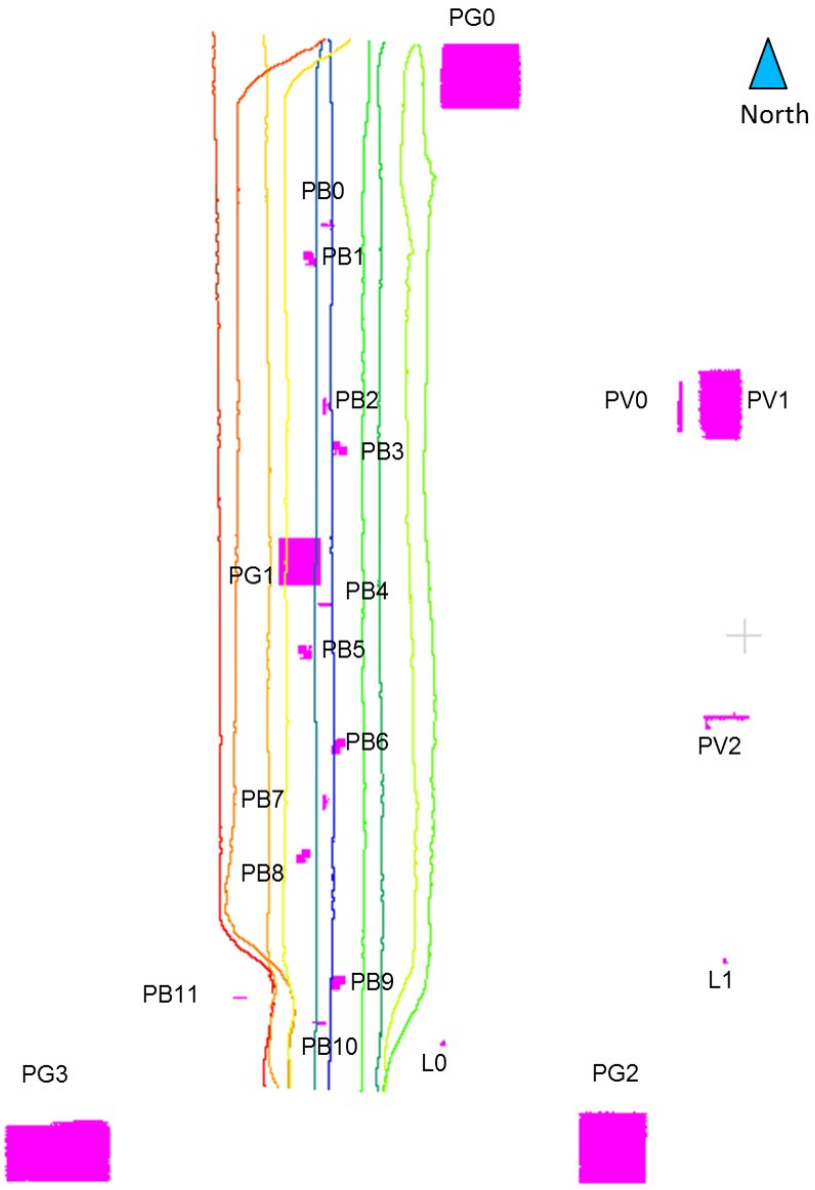

Fig. 4.20.: Configuration of drive-runs and calibration primitives for the PhenoRover-based MMS

4.6 Summary

This chapter mainly focused on developing a point-pairing-based calibration strategy for multi-LiDAR multi-camera mobile mapping systems, which can derive the

Table 4.3.: Mounting parameters before and after calibration of the PhenoRover-based MMS

Reference Unit: HDL32E (Left) LiDAR Unit Mounting Parameters $\left(r^{b}_{\mathbf{Lu}'_L},\ R^{b}_{\mathbf{Lu}'_L}\right)$						
	ΔX (m)	ΔY (m)	ΔZ (m)	$\Delta\omega$ (°)	$\Delta\phi$ (°)	$\Delta\kappa$ (°)
Initial	1.35	-1.30	-0.39	0	15	0
Final	1.3575	-1.3026	-0.39	1.9506	16.6891	-0.1754
Standard Deviation	0.0057	0.0039	Fixed	0.0098	0.0179	0.0155
HDL32E (Right) LiDAR Unit Mounting Parameters $\left(r^{\mathbf{Lu}'_L}_{\mathbf{Lu}'_R},\ R^{\mathbf{Lu}'_L}_{\mathbf{Lu}'_R}\right)$						
	ΔX (m)	ΔY (m)	ΔZ (m)	$\Delta\omega$ (°)	$\Delta\phi$ (°)	$\Delta\kappa$ (°)
Initial	0	1.50	0	0	0	0
Final	-0.0014	1.5293	-0.0273	-0.0180	-1.2501	-0.1841
Standard Deviation	0.0067	0.0049	0.0037	0.0118	0.0193	0.0159
Reference Camera: Grasshopper (Left) Camera Mounting Parameters $\left(r^{b}_{C_L},\ R^{b}_{C_L}\right)$						
	ΔX (m)	ΔY (m)	ΔZ (m)	$\Delta\omega$ (°)	$\Delta\phi$ (°)	$\Delta\kappa$ (°)
Initial	1.36	-1.55	-0.39	180	0	-90
Final	1.3182	-1.5251	-0.2443	169.7510	-15.6958	-93.0163
Standard Deviation	0.0643	0.0633	0.0564	0.1945	0.2125	0.1371
Grasshopper (Right) Camera Mounting Parameters $\left(r^{C_L}_{C_R},\ R^{C_L}_{C_R}\right)$						
	ΔX (m)	ΔY (m)	ΔZ (m)	$\Delta\omega$ (°)	$\Delta\phi$ (°)	$\Delta\kappa$ (°)
Initial	1.9353	-0.0002	-0.3331	-0.3101	20.2899	0.0668
Final	1.9517	0.0116	-0.3212	-0.4731	20.3930	0.1289
Standard Deviation	0.0677	0.0710	0.0512	0.2319	0.2086	0.1444

mounting parameters of multiple laser units and cameras simultaneously for terrestrial mobile mapping systems. This avoids the need to perform a separate calibration for each laser unit and each camera. The point-pairing-based bundle adjustment was theoretically compared with the conventional bundle adjustment, which revealed the equivalency of the two models in terms of their parameter estimation ability. The proposed calibration procedure can utilize different types of conjugate features

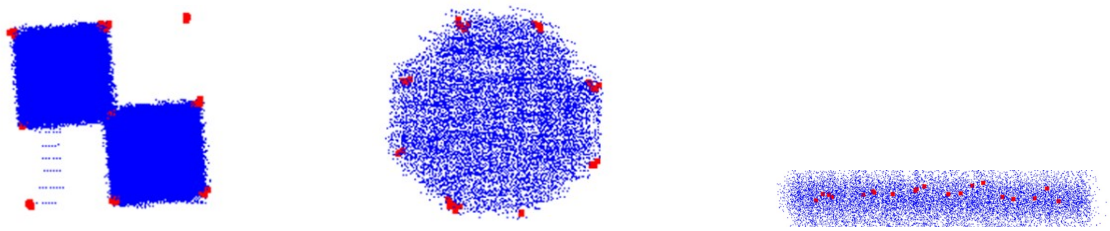

(a) Checkerboard target and its corners

(b) Stop sign and its corners

(c) Ridge of hut-shaped target

Fig. 4.21.: Qualitative evaluation of 3D alignment between LiDAR (blue) and image-based object points (red) after calibration of PhenoRover-based MMS

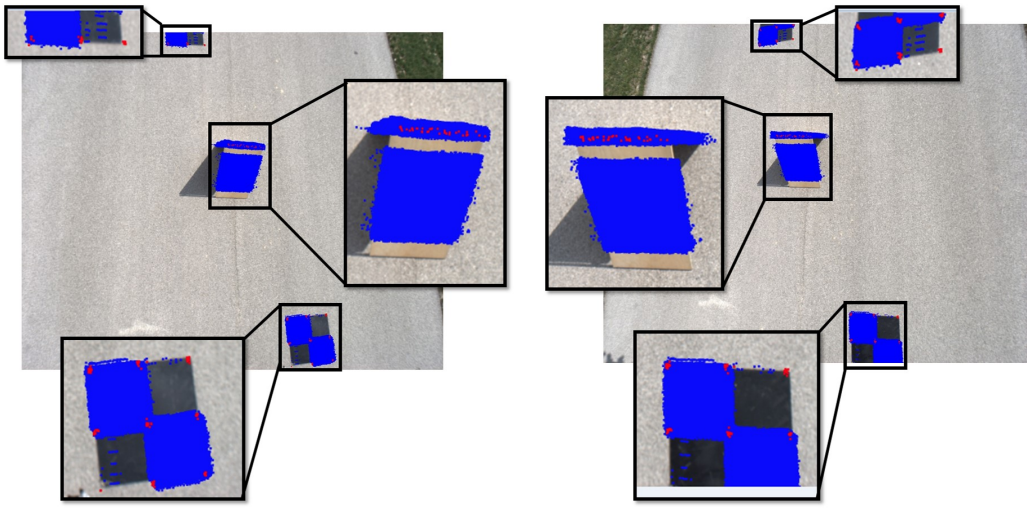

(a) Left camera image

(b) Right camera image

Fig. 4.22.: PhenoRover-based MMS: Backprojection of LiDAR (blue) and image-based object points (red) onto stereo-pair images

(i.e., planar, linear) from the LiDAR data, along with conjugate or pseudo-conjugate points in images belonging to different calibration primitives. An optimal representation and pairing scheme between imagery and LiDAR data was developed for point, linear features, and planar features by estimating the point definition redundancy that quantifies the contribution of a point pair towards system calibration. The proposed

Table 4.4.: RMSE of plane/line-fitting before and after calibration of PhenoRover-based MMS

Feature ID	No. of LiDAR Points	No. of Image Points	RMSE (m)	
			Before Calibration	After Calibration
Reflective Boards				
PB0	11,703	14	0.146	0.024
PB1	100,730	102	0.296	0.018
PB2	115,452	-	0.270	0.024
PB3	103,211	64	0.280	0.021
PB4	11,866	42	0.141	0.012
PB5	98,680	89	0.284	0.022
PB6	105,462	69	0.234	0.029
PB7	123,526	-	0.262	0.021
PB8	97,314	85	0.240	0.023
PB9	115,910	220	0.266	0.022
PB10	7,920	75	0.159	0.016
PB11	8,227	17	0.120	0.010
Ground Patches				
PG0	1,396,577	-	0.724	0.022
PG1	2,795,671	-	0.738	0.024
PG2	137,547	-	0.985	0.026
PG3	43,530	-	0.736	0.020
PG4	1,391,031	-	0.542	0.021

Feature ID	No. of LiDAR Points	No. of Image Points	RMSE (m)	
			Before Calibration	After Calibration
Hut Surfaces and Wall Patches				
PV0	459,993	-	0.731	0.027
PV1	25,820	-	1.019	0.058
PV2	41,477	-	0.151	0.030
PV4	134,877	-	0.229	0.016
PV5	134,554	-	0.246	0.030
PV6	93,092	-	0.160	0.016
PV7	93,523	-	0.158	0.014
PV8	152,161	-	0.216	0.018
PV9	149,134	-	0.216	0.032
PV10	90,380	-	0.157	0.019
PV11	92,589	-	0.160	0.014
PV12	163,378	-	0.236	0.019
PV13	165,611	-	0.310	0.017
Light Poles (L) and Hut Ridges (LH)				
L0	39,417	14	0.047	0.013
L1	14,513	-	0.100	0.019
LH0	12,292	18	0.125	0.014
LH1	14,105	35	0.114	0.013
LH2	15,501	20	0.118	0.017
LH3	11,367	38	0.128	0.016
LH4	17,797	51	0.136	0.017

iterative calibration method is capable of deriving accurate estimates for the mounting parameters, even if the initial estimates for the scaling factors of image points or mounting parameters are considerably inaccurate. The proposed calibration strategy is observed to reach an accuracy which is better than the expected accuracy based on the accuracies of the hardware involved for each of the mobile mapping platforms.

5. IMAGE-LIDAR INTERACTIVE VISUALIZATION ENVIRONMENT (I-LIVE)

5.1 Introduction

This chapter presents the interface known as Image-LiDAR Interactive Visualization Environment (I-LIVE) developed as a part of this research in order to allow end-users to conduct a qualitative evaluation of data acquired from any mobile mapping system consisting of a variable number of LiDAR units and cameras. I-LIVE enables the visualization of point clouds and imagery data, and evaluate their registration quality. The primary purpose of the interface is to serve as a tool for the quality control of GNSS/INS-derived trajectory and LiDAR-camera system calibration. I-LIVE is based on the open-source software - CloudCompare v2.9 - that allows the visualization of 3D point clouds. It is further extended to include functionalities that integrate the 3D (point clouds) and 2D (imagery) modalities to facilitate information extraction. An overview of the two windows (Point Cloud Viewer and Image Viewer) is shown in Figure 5.1. The Point Cloud Viewer deals with the display and manipulation of 3D point cloud data whereas the Image Viewer is used for displaying the corresponding 2D imagery data.

5.2 I-LIVE Input Information

The following information is required in order to enable the integration of 2D and 3D information within I-LIVE:

1. *3D Point Cloud(s):* The 3D point clouds are reconstructed from the raw LiDAR data along with the estimated LiDAR mounting parameters and the GNSS/INS-

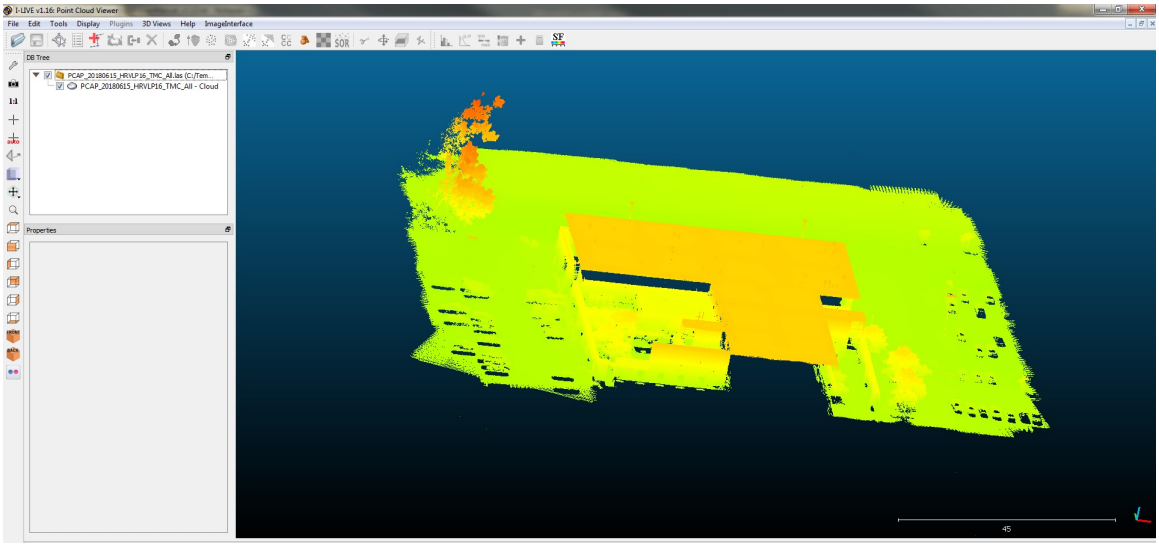

(a) Point Cloud Viewer

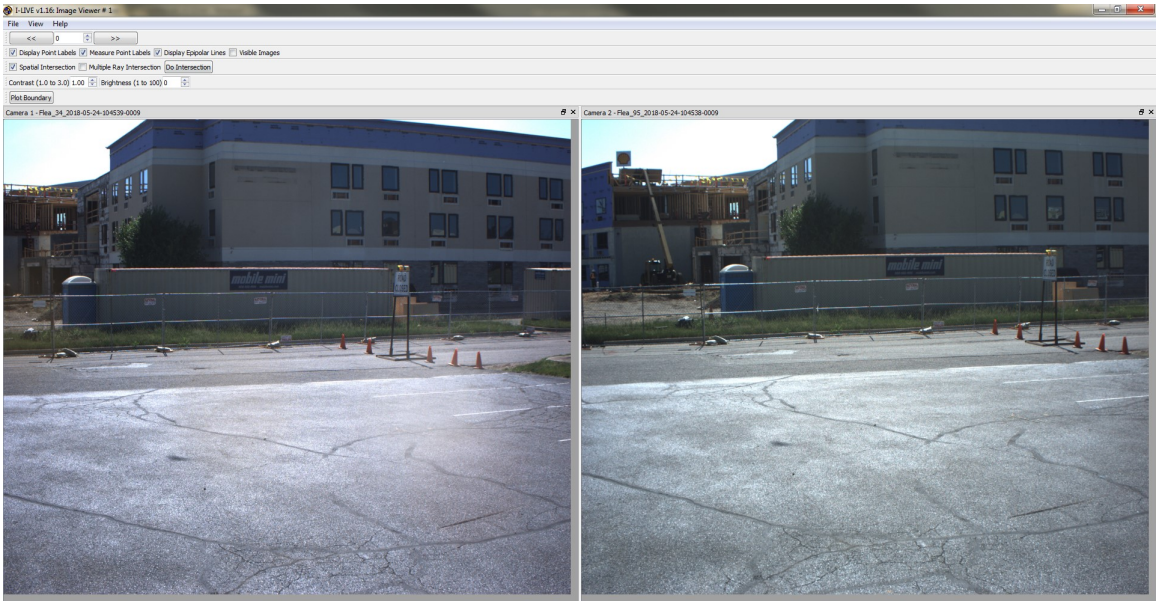

(b) Image Viewer

Fig. 5.1.: Visualization of 3D and 2D data in I-LIVE

derived trajectory information. These 3D point clouds can be loaded onto the Point Cloud Viewer within I-LIVE.

2. *2D RGB Imagery:* The sequence of 2D RGB images captured during data collection are loaded into the Image Viewer along with the corresponding GNSS/INS-derived trajectory information indicating the vehicle position and orientation corresponding to the epoch of each image in the sequence.

3. *Camera Parameters:* In addition to the 2D and 3D data input to I-LIVE, the integration of these different modalities requires information regarding the IOPs and mounting parameters of the cameras used to capture the input sequence of 2D images.

5.3 I-LIVE Functionalities

1. *Image Navigation:* I-LIVE can be used to navigate/stream through stereo-images captured during a data collection from multiple cameras. It can either be done manually to jump to the images of interest or it can conduct an automatic streaming of stereo-images at a user-defined time interval between consecutive images.

2. *Point Measurement:*

   (a) Measure Image Points: I-LIVE allows users to measure points of interest in various images and store their raw image coordinates. This is particularly helpful for conducting a multi-sensor system calibration, where the image points belonging to various features need to be measured in several images. One should note that I-LIVE facilitates image coordinate measurement upto a sub-pixel accuracy by zooming into the images and displaying them in super-resolution.

   (b) Display Point Labels: The Image Viewer in I-LIVE can be used to display the image points that were previously measured and recorded by overlaying them onto the corresponding image along with the corresponding point labels. This can be used to verify/correct prior measurements.

(c) Display Epipolar Lines: The point measurement for a stereo-pair of images is made easier by having an option to display the epipolar line when a point in either the left or right camera is clicked. However, this function is dependent on the availability of accurate interior orientation parameters of the two cameras as well as the relative orientation parameters between the two cameras.

3. *Intersection:* I-LIVE allows to derive object space (3D) coordinates of any point observed in two or more images from the same/different cameras at same/different epochs. The derived 3D object point is then displayed onto the Point Cloud Viewer while placing it at the appropriate location with respect to any already loaded and displayed point cloud in the window, as shown in Figure 5.2. This feature is one of the tools that facilitates the qualitative and quantitative evaluation of the registration accuracy between LiDAR and imagery data. However, this functionality is contingent upon the availability of accurate GNSS/INS-derived trajectory, i.e., the position and orientation of the vehicle at the moment of image capture; accurate mounting parameters relating the cameras to the onboard GNSS/INS unit; and the IOPs of the cameras.

4. *Backprojection:* While intersection allows the computation of 3D coordinates from a set of observed 2D points, backprojection is a strategy that computed the 2D projection of a 3D point onto an image. The base software of I-LIVE - CloudCompare - has a "Point Picking Tool" that displays all information related to a 3D point clicked by the user. This is further enhanced in I-LIVE by adding a feature to automatically backproject the clicked 3D point onto the stereo-pair which was captured closest to the clicked point, as shown in Figure 5.3. Moreover, the user is also provided with a list of all images where the clicked point is visible in the images loaded onto Image Viewer. A 3D point is considered to be visible in an image if its backprojected image coordinates lie within the image bounds and if the distance of the 3D point from the camera

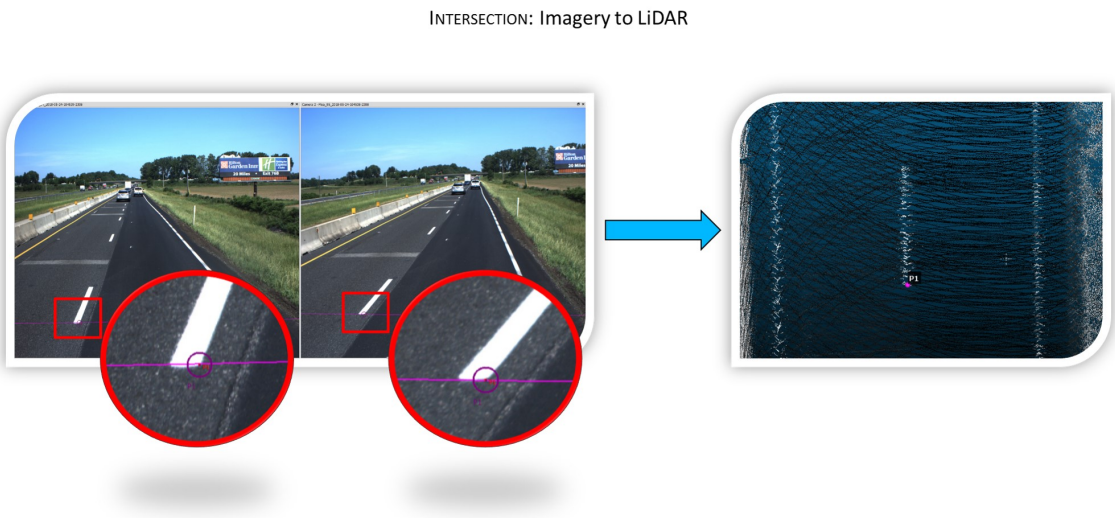

Fig. 5.2.: I-LIVE: Intersection of a point visible in a stereo-pair to compute its 3D mapping frame coordinates, as shown on the right

location at the instant of image capture is less than a user-defined threshold. This distance threshold ensures the reduction in the cluttering of backprojected image points that may arise as a result of 3D points that are far away from the camera.

5.4 Summary

Equipped with the functionalities listed above, I-LIVE serves as a tool aimed for end-users to conduct a qualitative and quantitative evaluation of data acquired from an MMS developed over any platform consisting of sensors capturing 2D and/or 3D data. The major contribution of I-LIVE is the integration of data acquired in the form of point clouds (3D) and images (2D), in order to analyze the quality of GNSS/INS-derived trajectory and LiDAR-camera system calibration. The Point Cloud Viewer within I-LIVE can be used to display the 3D point cloud that is reconstructed from the raw data acquired by the LiDAR units onboard an MMS. The 3D point cloud visualization can be used to evaluate the LiDAR system calibration parameters. For

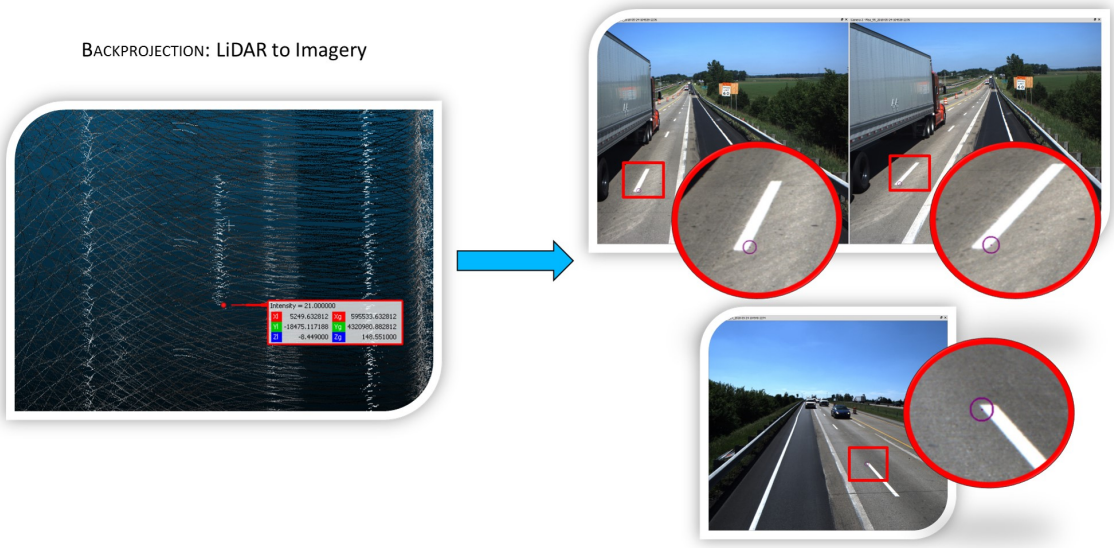

Fig. 5.3.: I-LIVE: Backprojection of a 3D point from a point cloud onto the three cameras onboard the car-mount system shown in Figure 4.10

instance, a misalignment in 3D point cloud acquired for the same area from different drive-runs and/or different sensors would indicate an inaccuracy in the LiDAR mounting parameters or the GNSS/INS-derived trajectory information that have been used to reconstruct the point cloud. The integration of the 3D data along with 2D imagery displayed in the Image Viewer can be used to detect any miscalibration of the camera mounting parameters. Apart from the basic tools to integrate the 2D and 3D modalities for qualitative and quantitative quality control of the acquired data, I-LIVE also consists of tools to facilitate accurate image point measurement for system calibration.

6. CONCLUSIONS AND RECOMMENDATIONS FOR FUTURE WORK

6.1 Overview

The goal of the research proposed in this thesis is to devise an accurate calibration strategy for terrestrial mobile mapping systems and further, allow a qualitative and quantitative evaluation of the calibration results for generic mobile mapping systems. This research started off with a thorough bias impact analysis for terrestrial mobile mapping systems consisting of a spinning multi-beam laser scanner, and validated the analytically driven conclusions by evaluating the results from an experimental setup. Based on this analysis, an optimal target primitive setup and drive-run configuration was devised for calibrating a multi-LiDAR mobile mapping system. Finally, a point-pairing-based iterative calibration strategy for multi-LiDAR multi-camera systems is proposed, realized, and experimentally validated. The ability of the proposed approach to simultaneously estimate the mounting parameters for multiple LiDAR units and cameras avoids the need to perform a separate calibration for each laser unit and each camera. The proposed calibration strategy is observed to reach an accuracy that is better than the expected accuracy based on the accuracies of the hardware involved for each of the mobile mapping platforms. This research concluded by developing an Image-LiDAR Interactive Visualization Environment (or, I-LIVE) that can integrate LiDAR and image data acquired by different platforms in order to facilitate a quality check of the acquired data.

6.2 Major Contributions

The major contributions of this thesis that significantly overcome the limitations of the state-of-the-art techniques are as follows:

1. In the proposed approach, there is no requirement of any specially-designed calibration targets with known properties (such as, known shapes, patterns, or dimensions) in order to conduct an accurate calibration. Instead, the calibration can be done using any planar/linear features and distinctly identifiable points available in the surrounding environment, such as building facades, rooftops, traffic sign boards, and light poles.

2. Since this thesis proposes a feature-based calibration technique, the approach does not necessarily require exact point-to- point correspondences of any type (2D-2D, 2D-3D, or 3D-3D). Instead, it uses pseudo-conjugate points belonging to conjugate features that can be easily extracted from LiDAR and camera data.

3. The proposed calibration approach is capable of simultaneously estimating the extrinsic parameters relating an arbitrary number of sensors (LiDAR units and cameras), i.e., it has no such restriction that it would work only for single LiDAR-single camera systems. Moreover, this approach is generic to be applied to terrestrial and airborne mapping systems alike - an aspect that, to the best of our knowledge, has not been addressed in any of the previous literature.

4. We propose a sensor-independent calibration model, i.e., it is independent of whether the mapping system consists of a single-beam or a multi-beam LiDAR, 2D or 3D laser scanner, and whether a camera is a frame or a line camera. The calibration for any combination of any type of these sensors can be achieved using the proposed calibration technique without making any modification to the model. While this thesis only presents results for multi-beam LiDAR units and frame cameras, the applicability of the proposed calibration model to other sensor types will be the focus of future work.

5. The approach is flexible to the type of the mapping system being used, i.e., the calibration approach can be applied to stationary as well as mobile mapping systems alike. In case of mobile mapping systems, the proposed approach relies on the availability of a GNSS/INS unit and we propose a single-step calibration technique that can estimate the extrinsic calibration relating any combination of the mentioned sensors, i.e., LiDAR-LiDAR, LiDAR-camera, camera-camera, LiDAR-GNSS/INS, and/or camera-GNSS/INS, simultaneously.

6. Although this thesis only addresses the estimation of extrinsic parameters relating the various onboard sensors, it is worth mentioning that our model is realized with the ability to simultaneously estimate the intrinsic parameters of the different sensors since the model deals directly with raw data obtained from different sensor modalities for attaining an accurate calibration.

7. This thesis also validates the accuracy of the proposed strategy by conducting an extensive qualitative evaluation by studying the registration of the data obtained from different modalities in the 3D object space as well as 2D image space. Moreover, a thorough quantitative evaluation is also reported by listing the standard deviations of the estimated parameters, the quality of fit for different calibration features, and the comparison of results to the expected error derived using error propagation calculation.

8. This research concluded by developing an Image-LiDAR Interactive Visualization Environment (or, I-LIVE) that can integrate LiDAR and image data acquired by different mobile mapping platforms. With in-built functions for image streaming, image measurement, backprojection, and light ray intersection, I-LIVE is one of the first tools aimed at providing the end-users with the ability to perform a quality check of the acquired data and to evaluate the quality of registration of data from different sensor modalities.

6.3 Limitations and Future Work

Apart from the above-mentioned characteristics, the assumptions and limitations of our proposed calibration approach, which serve as the basis for future work, are summarized as follows:

1. Although the calibration approach is capable of dealing with stationary as well as mobile systems, in case of mobile mapping systems, the proposed approach relies on the availability of sufficiently accurate GNSS/INS position and orientation information. However, if the GNSS/INS-derived trajectory information is not accurate, the proposed approach has the ability to detect this issue by analyzing the fitting residuals for different features.

2. Since the previously developed calibration techniques mostly rely on specifically designed calibration targets, these approaches facilitate the automatic extraction of such features. However, the limitation of this thesis is the manual effort involved in certain steps, such as selection of seed points and bounding points for various features during feature extraction from LiDAR data and the manual image coordinate measurement for the various calibration features captured by the cameras. This can be attributed to the flexibility provided in the choice of features being used for calibration. Therefore, a method to identify such LiDAR and camera-based features that are useful for calibration is necessary.

3. Although the proposed calibration model can be used to simultaneously estimate the intrinsic parameters of the different sensors (LiDAR and camera) along with the extrinsic parameters, this work still does not address the development of an optimal/minimal track and target configuration in order to derive accurate estimates of all these parameters. Hence, the experimental results included in this paper only focus on the estimation of extrinsic parameters.

4. The final goal of this research would be the development of an automatic calibration module that can be used within a method for multi-modal simultaneous localization and mapping.

5. Furthermore, the interface I-LIVE developed in this research will be further enhanced to incorporate application-specific functionalities pertaining to information extraction and visualization for agricultural applications, transportation engineering, infrastructure monitoring, and shoreline monitoring in order to serve a larger group of end-users. In the future, we also hope to add support for other sensor types, such as hyperspectral push-broom scanners, and introduce a new component for orthophoto visualization and manipulation integrated with the point cloud and image viewers.

REFERENCES

REFERENCES

[1] Atanacio-Jiménez, G., González-Barbosa, J.-J., Hurtado-Ramos, J. B., Ornelas-Rodríguez, F. J., Jiménez-Hernández, H., García-Ramirez, T., and González-Barbosa, R. (2011). LiDAR Velodyne HDL-64E calibration using pattern planes. *International Journal of Advanced Robotic Systems*, 8(5):59. 4

[2] Bileschi, S. (2009). Fully automatic calibration of LiDAR and video streams from a vehicle. In *2009 IEEE 12th International Conference on Computer Vision Workshops, ICCV Workshops*, pages 1457–1464. IEEE. 9, 11, 12

[3] Castorena, J., Kamilov, U. S., and Boufounos, P. T. (2016). Autocalibration of LiDAR and optical cameras via edge alignment. In *ICASSP*, pages 2862–2866. 6

[4] Chan, T., Lichti, D. D., and Belton, D. (2013). Temporal analysis and automatic calibration of the Velodyne HDL-32E LiDAR system. *ISPRS Ann. Photogramm. Remote Sens. Spat. Inf. Sci*, 2:61–66. 4, 13

[5] Choi, J. (2014). Hybrid map-based SLAM using a Velodyne laser scanner. In *2014 IEEE 17th International Conference on Intelligent Transportation Systems (ITSC)*, pages 3082–3087. IEEE. 4

[6] Conrady, A. E. (1919). Decentered lens-systems. *Monthly notices of the royal astronomical society*, 79(5):384–390. 5, 6

[7] Delara, R., Mitishita, E., and Habib, A. (2004). Bundle adjustment of images from non-metric CCD camera using LiDAR data as control points. In *International Archives of XXth ISPRS Congress*, pages 13–19. 6

[8] Duane, C. B. (1971). Close-range camera calibration. *Photogramm. Eng*, 37(8):855–866. 5, 6

[9] Fremont, V., Bonnifait, P., et al. (2008). Extrinsic calibration between a multi-layer LiDAR and a camera. In *2008 IEEE International Conference on Multisensor Fusion and Integration for Intelligent Systems*, pages 214–219. IEEE. 6, 11, 12

[10] Furukawa, Y. and Ponce, J. (2009). Accurate camera calibration from multi-view stereo and bundle adjustment. *International Journal of Computer Vision*, 84(3):257–268. 6

[11] García-Moreno, A.-I., Gonzalez-Barbosa, J.-J., Ornelas-Rodriguez, F.-J., Hurtado-Ramos, J. B., and Primo-Fuentes, M.-N. (2013). LiDAR and panoramic camera extrinsic calibration approach using a pattern plane. In *Mexican Conference on Pattern Recognition*, pages 104–113. Springer. 8, 11, 12, 13

[12] Glennie, C., Brooks, B., Ericksen, T., Hauser, D., Hudnut, K., Foster, J., and Avery, J. (2013). Compact multipurpose mobile laser scanning system – Initial tests and results. *Remote Sensing*, 5(2):521–538. 4

[13] Glennie, C., Kusari, A., and Facchin, A. (2016). Calibration and stability analysis of the VLP-16 laser scanner. *ISPRS Annals of Photogrammetry, Remote Sensing & Spatial Information Sciences*. 5, 13

[14] Gong, X., Lin, Y., and Liu, J. (2013). 3D LiDAR-camera extrinsic calibration using an arbitrary trihedron. *Sensors*, 13(2):1902–1918. 10, 11, 12

[15] Guo, C. X. and Roumeliotis, S. I. (2013). An analytical least-squares solution to the line scan LiDAR-camera extrinsic calibration problem. In *2013 IEEE International Conference on Robotics and Automation (ICRA)*, pages 2943–2948. IEEE. 9, 11, 12

[16] Habib, A., Ghanma, M., Morgan, M., and Al-Ruzouq, R. (2005). Photogrammetric and LiDAR data registration using linear features. *Photogrammetric Engineering & Remote Sensing*, 71(6):699–707. 6

[17] Habib, A., Kersting, A. P., Bang, K. I., and Lee, D.-C. (2010). Alternative methodologies for the internal quality control of parallel LiDAR strips. *IEEE Transactions on Geoscience and Remote Sensing*, 48(1):221–236. 14

[18] Habib, A., Lay, J., and Wong, C. (2006). Specifications for the quality assurance and quality control of LiDAR systems. *Base Mapping and Geomatic Services of British Columbia*. Available online: https://engineering.purdue.edu/CE/Academics/Groups/Geomatics/DPRG/files/LIDARErrorPropagation.zip. 72, 81

[19] Habib, A. F., Kersting, A. P., Shaker, A., and Yan, W.-Y. (2011). Geometric calibration and radiometric correction of LiDAR data and their impact on the quality of derived products. *Sensors*, 11(9):9069–9097. 5

[20] He, M., Zhao, H., Davoine, F., Cui, J., and Zha, H. (2013). Pairwise LiDAR calibration using multi-type 3D geometric features in natural scene. In *2013 IEEE/RSJ International Conference on Intelligent Robots and Systems*, pages 1828–1835. IEEE. 4

[21] Le, Q. V. and Ng, A. Y. (2009). Joint calibration of multiple sensors. In *2009 IEEE/RSJ International Conference on Intelligent Robots and Systems*, pages 3651–3658. IEEE. 7

[22] Levinson, J. and Thrun, S. (2013). Automatic online calibration of cameras and lasers. In *Robotics: Science and Systems*, volume 2. 7

[23] Lin, H., Gao, J., Zhou, Y., Lu, G., Ye, M., Zhang, C., Liu, L., and Yang, R. (2013). Semantic decomposition and reconstruction of residential scenes from LiDAR data. *ACM Transactions on Graphics (TOG)*, 32(4):66. 1

[24] Mirzaei, F. M., Kottas, D. G., and Roumeliotis, S. I. (2012). 3D LiDAR-camera intrinsic and extrinsic calibration: Identifiability and analytical least-squares-based initialization. *The International Journal of Robotics Research*, 31(4):452–467. 7, 11, 12

[25] Muhammad, N. and Lacroix, S. (2010). Calibration of a rotating multi-beam LiDAR. In *2010 IEEE/RSJ International Conference on Intelligent Robots and Systems*, pages 5648–5653. IEEE. 4, 14

[26] Pandey, G., McBride, J. R., Savarese, S., and Eustice, R. M. (2012). Automatic targetless extrinsic calibration of a 3D LiDAR and camera by maximizing mutual information. In *2012 Twenty-Sixth AAAI Conference on Artificial Intelligence*. 8, 11, 12

[27] Park, Y., Yun, S., Won, C. S., Cho, K., Um, K., and Sim, S. (2014). Calibration between color camera and 3D LiDAR instruments with a polygonal planar board. *Sensors*, 14(3):5333–5353. 10, 11, 12

[28] Puente, I., González-Jorge, H., Martínez-Sánchez, J., and Arias, P. (2013). Review of mobile mapping and surveying technologies. *Measurement*, 46(7):2127–2145. 1, 12

[29] Pusztai, Z. and Hajder, L. (2017). Accurate calibration of LiDAR-camera systems using ordinary boxes. pages 394–402. 9, 11, 12

[30] Ravi, R., Lin, Y. J., Elbahnasawy, M., Shamseldin, T., and Habib, A. (2018a). Bias impact analysis and calibration of terrestrial mobile LiDAR system with several spinning multibeam laser scanners. *IEEE Transactions on Geoscience and Remote Sensing*, pages 1–15. 3

[31] Ravi, R., Lin, Y. J., Elbahnasawy, M., Shamseldin, T., and Habib, A. (2018b). Simultaneous system calibration of a multi-LiDAR multicamera mobile mapping platform. *IEEE Journal of Selected Topics in Applied Earth Observations and Remote Sensing*, 11(5):1694–1714. 3

[32] Renaudin, E., Habib, A., and Kersting, A. P. (2011). Featured-based registration of terrestrial laser scans with minimum overlap using photogrammetric data. *Etri Journal*, 33(4):517–527. 67

[33] Schwarz, B. (2010). LiDAR: Mapping the world in 3D. *Nature Photonics*, 4(7):429. 4

[34] Vallet, B., Xiao, W., and Brédif, M. (2015). Extracting mobile objects in images using a Velodyne LiDAR point cloud. *ISPRS Annals of the Photogrammetry, Remote Sensing and Spatial Information Sciences*, 2(3):247. 4

[35] Vel'as, M., Španěl, M., Materna, Z., and Herout, A. (2014). Calibration of RGB camera with Velodyne LiDAR. 9, 11, 12

[36] Weiss, U. and Biber, P. (2011). Plant detection and mapping for agricultural robots using a 3d LiDAR sensor. *Robotics and autonomous systems*, 59(5):265–273. 1

[37] Weng, J., Cohen, P., and Herniou, M. (1992). Camera calibration with distortion models and accuracy evaluation. *IEEE Transactions on Pattern Analysis & Machine Intelligence*, (10):965–980. 5

[38] Williams, K., Olsen, M. J., Roe, G. V., and Glennie, C. (2013). Synthesis of transportation applications of mobile LiDAR. *Remote Sensing*, 5(9):4652–4692. 1

[39] Willis, A. R., Zapata, M. J., and Conrad, J. M. (2009). A linear method for calibrating LiDAR-and-camera systems. In *MASCOTS*, pages 1–3. 11, 12

[40] Zhang, Q. and Pless, R. (2004). Extrinsic calibration of a camera and laser range finder (improves camera calibration). In *IROS*, volume 3, pages 2301–2306. 6, 11, 12

[41] Zhang, Z. (2000). A flexible new technique for camera calibration. *IEEE Transactions on pattern analysis and machine intelligence*, 22:1330–1334. 5

[42] Zhou, L. and Deng, Z. (2012). Extrinsic calibration of a camera and a LiDAR based on decoupling the rotation from the translation. In *Intelligent Vehicles Symposium (IV), 2012 IEEE*, pages 642–648. IEEE. 11, 12

VITA

VITA

Radhika Ravi received her B.Tech. in Civil Engineering with second major in Electrical Engineering from Indian Institute of Technology Kanpur, India, in 2016. She is currently pursuing her M.S. degree in Civil Engineering (Geomatics) at the Lyles school of Civil Engineering at Purdue University, West Lafayette, IN, USA.

Her research interests include 3D point cloud reconstruction from LiDAR and photogrammetric data, intrinsic and extrinsic calibration of mobile LiDAR systems, and calibration of LiDAR systems integrated with several cameras.